IPP-Report

Max-Planck-Institut
für Plasmaphysik

Carl Friedrich Benedikt Zimmermann

Feasibility of Extracting Momentum Transport Coefficients from NBI Modulation Experiments in ASDEX Upgrade

Machbarkeitsstudie zur Extrahierung von Impuls-Transport-Koeffizienten aus modulierten NBI-Experimenten in ASDEX Upgrade

IPP 2020-13
November 2020

FEASIBILITY OF EXTRACTING MOMENTUM TRANSPORT COEFFICIENTS FROM NBI MODULATION EXPERIMENTS IN ASDEX UPGRADE

MACHBARKEITSSTUDIE ZUR EXTRAHIERUNG VON IMPULS-TRANSPORT-KOEFFIZIENTEN AUS MODULIERTEN NBI-EXPERIMENTEN IN ASDEX UPGRADE

MASTER THESIS

WRITTEN AT THE
MAX PLANCK INSTITUTE FOR PLASMA PHYSICS
IN GARCHING

SUBMITTED TO THE
LUDWIG MAXIMILIAN UNIVERSITY OF MUNICH,
DEPARTMENT OF PHYSICS

submitted by:	Carl Friedrich Benedikt Zimmermann
supervisor:	Dr. Rachael M. McDermott and Dr. Emiliano Fable
academic supervisor:	PD Dr. Thomas Pütterich

Abstract

In this thesis, an analysis method was studied and validated to extract momentum transport coefficients from NBI modulation experiments at the ASDEX Upgrade fusion device at the Max Planck Institute for Plasma Physics in Garching, Germany. The aim was to find a model for the momentum transport of the plasma particles that accurately predicts the dynamics of the plasma rotation experimentally measured.

To do so, a set of discharges was studied, revealing similar time-averaged background profiles for the ion and electron temperature, the electron density and the plasma rotation. In these discharges, different temporal perturbations were imposed by modulating the power of the NBI, ECRH, and ICRH. All considered discharges should exhibit similar transport parameters within error bars.

Examining the model showed that a linearly, radially increasing Prandtl number $Pr = \chi_i/\chi_\varphi$ is needed for the diffusive transport. Furthermore, optimization exhibited a degeneracy of the possible solutions, such that the GKW code was used to impose further assumptions on the Prandtl number. Afterwards, the convective transport contribution was studied, where it was possible to reproduce similar transport parameters for all studied discharges.

This model was implemented in the ASTRA code and the corresponding transport coefficients reproduced the experimentally measured phase and amplitude profiles of the rotation very well. Deviations in the rotation profiles were found, which were explained with an intrinsic rotation caused by residual stress. For all discharges with similar background profiles, the same intrinsic rotation was calculated.

The successful verification of this methodology opens the door to study the parametric dependence of the diffusive and convective momentum transport as well as the turbulent intrinsic rotation.

Zusammenfassung

In dieser Arbeit wurde eine Analyse-Methode untersucht und validiert, um Impuls-Transport-Koeffizienten aus modulierten NBI-Experimenten am ASDEX Upgrade Fusionsreaktor am Max-Planck-Institut für Plasmaphysik in Garchingen zu extrahieren. Das Ziel war, ein Impuls-Transport-Modell zu entwickeln, um die Dynamik der Plasma-Rotation im Reaktor vorherzusagen und diese mit experimentellen Daten zu vergleichen.

Dafür wurden Plasmaentladungen untersucht, die alle ähnliche Hintergrundprofile für die relevanten Größen von Elektronen- und Ionentemperatur, Elektronendichte und Plasmarotation zeigten. Bei diesen Entladungen wurde die Leistung der NBI, ECRH und ICRH moduliert und dadurch eine zeitabhängige Störung ins Plasma eingebracht. Trotz der Störung müssen sich für alle Entladungen mit selben Hintergrundprofilen selbe Transportparameter finden lassen.

Eine genaue Untersuchung des Modells zeigte die Notwendigkeit einer linearen, radial steigenden Prandtl-Zahl, um den diffusiven Teil des Transports zu erklären. Bei den Untersuchungen zeigte sich, dass der Raum möglicher Lösungen unterbestimmt war, sodass der GKW-Code verwendet wurde, um weitere Annahmen über die Prandtl-Zahl treffen zu können. Anschließend wurde näher auf den konvektiven Anteil des Impulstransports eingegangen, wobei es möglich war, ähnliche Transportparameter für alle untersuchten Entladungen zu finden.

Das Modell wurde im Rahmen des ASTRA-Codes implementiert und die berechneten Transportparameter waren in der Lage, die experimentell gemessenen Fourier-Profile erfolgreich zu reproduzieren. Abweichungen zeigten sich bei den Profilen zur Rotation, wobei die Differenz mit einer intrinsischen Rotation durch den Residual Stress erklärt werden konnte. Dabei war die intrinsische Rotation für alle untersuchten Entladungen in Übereinstimmung.

Die erfolgreiche Validierung dieser Methodik ermöglicht nun, die parametrischen Abhängigkeiten des diffusiven und konvektiven Impuls-Transports und der intrinsischen Rotation zu studieren.

Acknowledgements

First of all, the author would like to thank Dr. Thomas Pütterich who gave the author the possibility to come into contact with possible supervisors for the thesis. His door was always open not only for organisational work, but also for scientific discussion.

Various colleagues contributed to this thesis. In general, the author wants to thank the whole ASDEX Upgrade experimental staff, leading the experiments and working on the diagnostics to provide the experimental data on which this thesis is based on, also the experts from the MST1 team, namely Dr. Tomas Tala, Dr. Antti Salmi and Dr. Basil Duval.

The author would like to name Dr. Alexander Bock who provided the author with code snippets to use Python to extract shotdata as well as all the experts who contributed with their data like Dr. Matthias Benert, Dr. Christoph Fuchs and Dr. Padraig Mac Carthaigh. The CXRS team around Dr. Ralph Dux deserves special mention providing the author with the invaluable experimental data of their diagnostics.

For the helpful discussions after various test talks, the author would like to thank Dr. Marco Cavedon, Dr. Athina Kappatou, Dr. Elisabeth Wolfrum, Dr. Hendrik Meyer and Peter Miersch.

Dr. Rainer Fischer was a big help, recalculating the IDA and IDE data for the considered discharges and Dr. Giovanni Tardini, who introduced the author to the use of TRANSP and discussing results. Dr. Clemente Angioni contributed significantly by performing the GKW calculations and helping the author to understand and evaluate the results.

This thesis would not have been possible without the help of Dr. Emiliano Fable who gave the author the possibility to use ASTRA, introduced him to different models and took care of the theoretical validity of this work.

Most of all, the author is indebted to Dr. Rachael McDermott, who was motivated from the first contact in summer 2019 until the stressful time in late August to help the author with all his questions, to point him to the right directions, to never hesitate to call a spade a spade and by doing so gave the author the opportunity to get into this field of physics.

Her, Florian Jung, and Charlotte Dietrich the author would like to thank for proof reading and Dr. Tautvydas Maceina for the nice office neighborhood.

Finally, the author is grateful to the German Academic Scholarship Foundation which has supported the author during his university time and gave him the possibility to make the most of this period of life. The author hopes to have met the expectations and the trust placed in him during this six years.

Contents

Chapter 1

Introduction

In the second half of the last century, the decision-makers of the industrialized countries became aware of the need to look beyond the fossil age. By doing so, the research for alternative, non-fossil based sources of energy has been intensified. A method of energy generation, discovered in the 1940s, could significantly contribute meeting the growing demand for energy: nuclear fusion.

After declassification of fusion research in 1958, scientists all over the world have participated to set up experimental devices to study the possibility of building fusion energy reactors. The aim is to gain more energy than needed to ignite and sustain the fusion process.

Nuclear fusion

A basic requirement for a fusion reactor is to heat up the fuel to millions of degrees Kelvin. At such high temperatures, the electrons in atoms separate from their protons so that the fuel becomes a plasma. Via quantum tunneling, the ions overcome the Coulomb barrier and fuse. The energy gained by the fusion process due to the mass difference is released as kinetic energy, leading to further heating of the plasma or to losses to the plasma-facing reactor components.

The most common fusion reaction in stars is the proton-proton fusion, which has a very low cross section and is, therefore, not utilizable for an industrial energy production. The tritium-deuterium fusion reaction is best suited for a fusion reactor on earth due to a high reaction rate at achievable temperatures. Beside that, the fusion products are easy to confine and to handle from a safety-points perspective [1, p. 20]. The reaction equation reads as given below.

$$^{2}\mathrm{D} + {}^{3}\mathrm{T} \rightarrow {}^{4}\mathrm{He}(3.5\,\mathrm{MeV}) + \mathrm{n}(14.1\,\mathrm{MeV})$$

Confinement

To ignite a fusion reaction, the Lawson criterion has to be fulfilled [2]. A more general form of this law states that the product of the plasma density n, the temperature T and the energy confinement time τ_E has to be larger than a given value such that the energy losses are smaller than the energy gained in the reaction [1, p. 19]. For a 50/50 tritium-deuterium plasma at a temperature of $T_e = 30$ keV and a density of $n_e = 10^{20}$ m^{-3} this so-called triple product reads as

$$n\,T\,\tau_E > 8.1 * 10^{21}\,\mathrm{keV\,s\,m^{-3}}, \tag{1.1}$$

where the left hand side has to be maximized within the experimental setup. The primary concept of confinement is rather complex: magnetic fields can be used to confine the moving, charged particles of a plasma.

The ASDEX Upgrade tokamak

One approach to confine a plasma within a magnetic field was proposed and experimentally introduced by the Soviet physicists Tamm and Sakharov in 1952 and was called tokamak after the acronym for "toroidal chamber with magnetic coils" (*ТОроидальная КАмера с МАгнитными*

Катушками, *TOroidalnaja KAmera s MAgnitnymi Katushkami*) [3, p. 450]. This concept basically consists of a toroidal plasma chamber with a field produced by simple magnets and a current in the plasma itself, which gives a poloidal component to the field. The current is driven by induction with a solenoid coil in the center where the plasma acts as the secondary winding of a transformer [4, p. 44].

The basic geometry is depicted below:

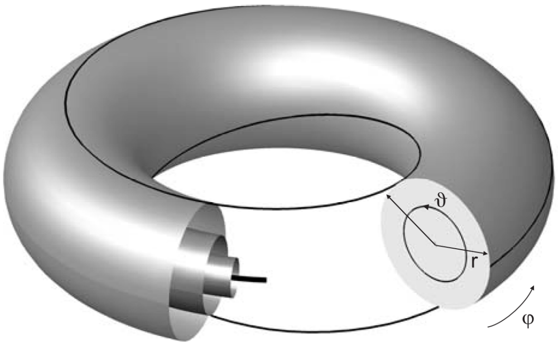

Figure 1.1: Sketch of a torus (figure taken from [4, p. 198])

The preferred coordinate system for tori uses three coordinates: φ for the toroidal angle, ϑ for the poloidal angle, and r for the minor radius. As an alternative, one can also use a standard cylindrical coordinate system with ϑ, z and minor radius r. The closed line at $r = 0$ in Figure 1.1 is called the magnetic axis.

The conditions for a plasma confining field are multiple. To minimize losses and balance drift effects, it has to be closed toroidally and also needs a poloidal component.

The *Axial Symmetric Divertor EXperiment* (ASDEX Upgrade) is a tokamak operated at the Max Planck Institute for Plasma Physics in Garching, Germany, and the largest tokamak in Germany at the moment. It is a research-oriented machine, such that the standard plasma consists of deuterium. Basic machine parameters are given in Table 1.1 [5]. It allows for a plasma heating up to roughly 30 MW with 1 MW Ohmic heating, 20 MW of *Neutral Beam Injection* (NBI), 8 MW of *Ion Cyclotron Resonance Heating* (ICRH) and 5 MW *Electron Cyclotron Resonance Heating* (ECRH). [5]

major radius of the magnetic axis	$R = 1.65$ m
maximum minor radius of the vessel	$a = 0.5$ m
maximum plasma current within the plasma	$I_p = 1.6$ MA
maximum toroidal field	$B_\varphi = 3.9$ T
discharge duration	$t_{FT} < 10$ s

Table 1.1: Main machine parameters of ASDEX Upgrade

Neutral Beam Injection

The NBI is the most powerful heating in ASDEX Upgrade and the most crucial heating system for this work. The basic idea is to inject high velocity neutral particles into the plasma which, in contrast to charged particles, are able to cross the strong magnetic fields. These particles transfer their energy to the plasma by simple collision processes and get ionized. To heat the plasma, the injected particles temperature has to be higher than that of the plasma particles. Usual beam energies vary between 40 keV and 100 keV.

To speed up the particles, positive or negative ions are accelerated by electric fields and then neutralized. At ASDEX Upgrade, positive ion sources are used. Depending on the geometry of the injection it is possible to transfer significant toroidal angular momentum with the injected particles. The injected angular momentum can be modulated with a given frequency by turning on and off the beams with frequencies of a few Hertz [1, p. 538].

ASDEX Upgrade has two neutral injectors, separated toroidally by 180° with four sources each. The two injectors provide deuterium particles with main energies of 60 keV (box 1, sources 1-4) and 93 keV (box 2, sources 5-8) with 20 MW power in total [5, p. 84].

The goal of momentum transport research

In 2017, a series of discharges was performed in ASDEX upgrade to test methods to extract momentum transport coefficients from NBI modulation experiments. The aim is to find a model for the momentum transport of the plasma particles that accurately predicts the dynamics of the plasma rotation in the reactor, i.e. reproduces the experimentally measured data. In addition, the model solution must be unique within the experimental uncertainties.

Generally, knowledge about transport is needed to understand the behavior in present day devices and to predict operation conditions of future devices that will be capable of producing net fusion power [6, p. 1].

There is still a lack of understanding of momentum transport [7, 8, 9], compared to heat [10, 11] and particle transport [12, 12], which are comparatively well understood. This difference in understanding is connected with the off-diagonal transport, which plays a bigger role in momentum transport [7]. Deep knowledge about momentum transport, as well as quantitative comparisons of theory with numerical simulations, are still missing [8, p. 12]. There is no fully validated predictive capability for the rotation of the plasma: the plasma rotation is always an input for simulations in fusion research.

The rotation itself is of high importance because it has a strong impact on other processes, especially on neoclassical [13] and turbulent impurity transport [14, 15]. Also, it provides stability against locked modes and resistive wall modes. It stabilizes turbulences and thus influences the confinement [16].

Thesis goals and structure

This thesis aims to verify the methods to analyse NBI modulation experiments and to make use of this type of experiment on the path towards an independent model explaining the plasma rotation.

In Chapter 2 the basic theory of momentum transport and the used models are introduced. The used methods and numerics are documented in Chapter 3. In Chapter 4, the concept of the performed experiments is explained and an overview of the considered discharges is given. A detailed verification of the used codes is performed in Chapter 5 and these are then used to optimize the transport model in Chapter 6. A summary, a discussion, and an outlook are given in Chapter 7.

Chapter 2

Momentum Transport

In this chapter the basic equations modeling the momentum transport are introduced and an overview of the most relevant concepts is given.

Plasma flow in a tokamak

The study of momentum transport is concerned with the question of how the plasma momentum moves radially. In a tokamak, the plasma flow is along flux surfaces. The velocity vector of the particles can be split up in a parallel and a perpendicular component with respect to the field lines. Alternatively, one can consider a toroidal and a poloidal vector component.

The velocity determining the momentum is mostly parallel or toroidal, as the poloidal or perpendicular velocity is strongly damped [17, 18]. In this work one assumes that the poloidal velocity is small compared to the error on the rotation data such that it is justified to approximate the parallel rotation velocity with the toroidal velocity and vice versa.

Overall, the radial transport of (mainly toroidal) momentum strongly influences the radial profile of the rotation.

Toroidal momentum

Due to the toroidal symmetry of a tokamak, the total toroidal angular momentum is a conserved quantity within the reactor. For the effects considered in this thesis, this conservation reads as

$$n\, R^2 \, \frac{\partial \Omega}{\partial t} = -\nabla \cdot (n\, \Gamma_\varphi + \Pi_{RS}) + \frac{S_{NBI}}{m_{ion}} \tag{2.1}$$

with the plasma rotation $\Omega = v_{\mathrm{rot}}/R \approx v_{\|}/R$, the toroidal velocity v_{rot}, the parallel velocity $v_{\|}$, the major radius R, the density n, the momentum source of the NBI S_{NBI} and the residual stress Π_{RS} [19, eq. 1].

To predict the momentum transport, one needs to solve for the torque of the NBI S_{NBI}, as well as for the parameters Γ_φ and Π_{RS}.

Momentum flux

The momentum flux Γ_φ splits into a diffusive and a convective part, where the first scales with the gradient of the parallel velocity and the second with the parallel velocity itself. This radial flux of parallel momentum can be expressed as

$$\Gamma_\varphi = -\chi_\varphi \, \frac{\partial v_{\|}}{\partial r} + v_{\mathrm{Pinch}} \, v_{\|}, \tag{2.2}$$

where χ_φ is the parallel momentum diffusion coefficient and v_{Pinch} the pinch velocity [19, eq. 18].

Diffusion coefficient

The diffusion coefficient χ_φ and the ion heat conduction coefficient

$$\chi_i = -\frac{Q_i}{n_i \nabla T_i} \tag{2.3}$$

define the Prandtl number [20]

$$Pr = \frac{\chi_\varphi}{\chi_i}, \tag{2.4}$$

which is predicted to be of order of unity [9, p. 2], showing little variation with plasma parameters [20, 21]. The strong coupling of χ_φ and χ_i arises from the fact that both quantities are proportional to different moments of the same velocity distribution.

Numerical calculations predict a dependence of the Prandtl number on the shear $s = \frac{r}{q}\frac{dq}{dr}$ such that one expects $Pr = Pr(r)$ [19] to have a radial dependence. A linear approach leads to the expression

$$Pr = (b + \texttt{CHE3} \cdot m \cdot \rho_\varphi), \tag{2.5}$$

where the scalars b and m reflect the linear ansatz and `CHE3` will be used later in this thesis for optimization of the model. The independent variable ρ_φ (speaking “rho toroidal”) is the radial flux coordinate and is defined as $\rho_\varphi = \sqrt{(\Psi_0 - \Psi)(\Psi_0 - \Psi_{sep})}$ with Ψ_0, the toroidal flux along the magnetic axis ($r = 0$), and Ψ_{sep} at the separatrix.

Coriolis drift and pinch

The Coriolis drift is produced by the Coriolis force in the rotating plasma frame [22]. It gives rise to a symmetry breaking of the transformation $v_\parallel \to -v_\parallel$ along the field lines [8], such that there is a preferential direction of rotation [7].

The so called pinch velocity results from the Coriolis drift, which couples density, temperature perturbations, and parallel velocity moment within the *Ion Temperature Gradient* (ITG) mode and leads to a radial gradient of the toroidal velocity profile even in absence of a torque [22].

Theoreticians predicted the various dependencies of the pinch, mainly scaling with the logarithmic density gradient $\frac{R}{L_{n_e}} = -\frac{R}{n}\frac{\partial n}{\partial R}$, the shear s, and the safety factor q [22]. For a linear ansatz, the pinch can be written as

$$v_{\text{Pinch}} \sim -\frac{\chi_\varphi}{R}(\texttt{CHE1} \cdot \frac{R}{L_{n_e}} + \texttt{CHE2} \cdot s). \tag{2.6}$$

As q and s are strongly coupled, only one of the two is included. However, other parameters are neglected in this model.

Coming from theory, the parameters `CHE1` and `CHE2` are positive scalars in order to have a negative pinch velocity and thus an inward convection reinforcing the present rotation [9, 22]. To constrain them to be positive is the starting point in this thesis and will be discussed again in Chapter 7.2.

Residual stress

The *Residual Stress* (RS) Π_{RS} causes an intrinsic rotation. In contrast to the pinch it can spin-up the plasma from rest [9, p. 4]. The effect involves all sources of momentum flux that result from non-linear symmetry breakings which are not proportional to the rotation or its gradient [23] [6, p. 2]. Also, the wave-particle momentum exchange [9, p. 3] contributes to this effect. It has no analog in the theory of particle or heat flux [9, p. 2] and is much less understood than the diffusive and convective effects [8, 6, 7].

For the ITG mode it is expected to be co-current ($\Pi_{RS} < 0$ [9, eq. 14], in the direction of I_p). Detailed studies with the help of gyrokinetic simulations (cf. Chapter 3.2) predict a strong correlation of the residual stress with the logarithmic density gradient $\frac{R}{L_{ne}}$ [23, 8, 6].

It is found in this work that experimental rotation data, e.g. at ASDEX Upgrade, can not be explained without the presence of a residual stress (cf. Chapter 6.5). A first approach for modeling the residual stress is made with the approximation [23, eq. 28]

$$\Pi_{RS} \sim \texttt{CV8} \cdot R \cdot \chi_\varphi \cdot \frac{R}{L_{n_e}}, \tag{2.7}$$

where multiple scaling constants have to be included. The parameter `CV8` can be used to scale the direction and size of the residual stress.

Summary

Having explained these effects, solving Equation 2.1 reduces to the calculation of the profiles χ_i (cf. Chapter 3.2) and S_{NBI} (cf. Chapter 3.2), the parameter for the linear dependency of Pr (cf. Chapter 3.2), and the fitting of the scalars `CHE1`, `CHE2`, and `CHE3` to the experimental data. To find a good solution, the simulation has to match the measured rotation profile $\Omega(r)$. Hereby, the room of possible solutions is underconstrained. To approach this problem, one considers the equations with temporal dependence and a perturbation to gain more information from the data to constrain the solutions.

Chapter 3

Methods

In this chapter the diagnostics and numerical codes used for this thesis are introduced.

3.1 Experimental data

The diagnostics at ASDEX Upgrade provide various methods to measure relevant quantities from performed plasma discharges. The ones used in this thesis are introduced in the section below.

IDA: electron density n_e and temperature T_e

The data for the electron density and temperature were obtained via the *Integrated Data Analysis* (IDA) [24]. This system brings together different diagnostic data like the *Lithium Beam emission spectroscopy* (LIB), the *Deuterium CyaNide laser interferometry* (DCN), the measurement of the *Electron Cyclotron Emission* (ECE), and the *Thomson Scattering spectroscopy* (TS). In order to do so, Bayesian probability theory is applied. This allows the profiles to be calculated with high temporal and spatial resolution and minimizes the systematic and statistical errors.

The used diagnostics are based on different physical principles.

- The **LIB** is a diagnostic to measure the electron density in the edge of the plasma [25]. An injector produces a neutral lithium beam. The lithium atoms are excited via collisions and light is emitted. Spectroscopy measurements of the emission profiles enable the electron density profiles to be inferred [26].

- The **DCN** is also used to measure the electron density, but in the core of the plasma. It is based on interferometry. A laser is fired into the plasma and the phase shift of the wave is compared to a wave travelling through vacuum. The observed shift is proportional to the density integrated along the path of the laser [27].

- The **ECE** is an established method to calculate the electron density. Charged particles, like electrons, gyrate around magnetic field lines. This acceleration leads to electromagnetic radiation with the cyclotron frequency. The resonance of this frequency and its harmonics is very high such that the plasma is optically thick. The intensity of the black body radiation which can be measured at this frequency is connected to the electron temperature. It can be measured by interferometers [1, p. 386].

- The **TS** is widely used to measure the electron temperature and density. The scattered light of a laser is Doppler shifted due to the thermal movement of the electrons. Powerful laser and array-detectors are needed to exploit this technique [1, p. 426].

IDA uses the radial flux coordinate ρ_ϑ as a common coordinate system. The underlying magnetic equilibrium is calculated with the *Integrated Data analysis Equilibrium* (IDE) code used at ASDEX Upgrade [28, 29]. It should be noted that Dr. Rainer Fischer (IPP Garching), who prepared the IDA shotfiles for the analysis performed in this thesis, used the IDE equilibrium for the IDA evaluations.

CXRS: toroidal rotation velocity v_{rot}/Ω, ion temperature T_i and impurity density n_{imp}

Charge eXchange Recombination Spectroscopy (CXRS) provides temporal and spatial high-resolution measurements of impurity ion temperature, density, and rotation profiles.

The injected neutral ions of the NBI undergo charge-exchange reactions with the fully ionized impurity ions. In this reaction, electrons are transferred from the neutral particles to the impurity ions, which leads to a de-excitation and line radiation. Spectroscopy measurements of the emitted light provide information about the temperatures and velocities via the the analysis of Doppler widths and Doppler shifts of the spectra and lines. Analysis of the intensity yields the main impurity densities n_{imp} when the neutral particle population is known.

In ASDEX Upgrade, arrays of fiber optics provide various *Lines Of Sight* (LOS) through the plasma such that radial profiles can be resolved. The integration times for core CXRS are usually of the order of 10 ms. Typically, the charge exchange lines for B^{5+} $(n = 7 \to 6)$ at 497.467 nm or for N^{7+} $(n = 9 \to 8)$ at 566.937 nm are used. The main impurity boron is introduced into the machine by boronization, i.e. the deposition of a thin boron layer onto the inner wall [30]. Besides that, the system can be used to measure any emission line between 390 - 700 nm like those of He, Li, C, F, Ne, O, Ar, or D_α.

To extract data, calibrations are necessary. These include the instrument of the spectrometer, dispersion due to the optics, noise, gain and smear characterization as well as an absolute wavelength and intensity calibration [31, p. 5]. In addition, corrections for Zeeman and fine structure splitting are routinely included. When this is done, systematic deviations on the rotation can be reduced down to ±1 km/s [31, 32].

It should be noted that within this thesis the assumption is made that the main impurity species represents the plasma main ions in terms of temperature and rotation. For the analysis carried out in this thesis mainly the core CXRS diagnostics CEZ was used. It looks at NBI source #3 in sector 15 and has 24 LOS. For the plasma edge, the CMZ data were used. The CCZ was found to be too noisy due to too low concentration of carbon. The CEZ measurements were made on boron and had a signal to noise ratio twice higher than the carbon measurements.

Various

For the numerical calculations carried out in this thesis, information on many different quantities is needed. In the following, a short overview is provided on the ones that have been not mentioned so far.

- P_{NBI} is the power of the NBI sources, where the power from each source can be read out from the NIS shotfiles individually.
- The ECRH operates with gyrotrons which inject waves in the frequency range of the electron cyclotron resonance and can accelerate the electrons [4, p. 91]. The injected ECRH power is denoted by P_{ECRH}.
- The effective nuclear charge Z_{eff} is the positive charge experienced by an electron. In a multi-component plasma it denotes the average over the density-weighted nuclear charges of the ions. It can be derived from bremsstrahlung background measurements along LOS of the core CXRS diagnostics.

3.2 Numerics

Significant numerical calculations were performed in this thesis. Following the order of use within the workflow: first, the data fitting is explained, afterwards the transport codes TRANSP, GKW, and ASTRA are introduced. The optimization method for the model is explained at the end.

Data fitting

For this thesis, time was spent to optimize the different input profiles needed for the numerical calculations. In this section the methodology used is explained.

Electron density n_e and temperature T_e, ion temperature T_i and rotation velocity v_{rot}

These four quantities are time-dependent profiles and are often referred to as the kinetic profiles. They each have a large impact on the results, so it is necessary to keep as much information as possible while fitting. Fitting is necessary to reduce noise and filter out high-frequency effects like *Edge Localized Modes* (ELM) (cf. [1, p. 327]) and *Sawteeths* (cf. [1, p. 317]). At the same time, smooth radial profiles are required to avoid unphysical discontinuities in the heat and momentum diffusion coefficients. The NBI modulation clearly impacts the ion temperature and rotation, while for the electron temperature and density it is, if present, often lost in the noise. If these effects are present, one aims to preserve them while fitting and smoothing the data.

Therefore, a bivariate spline fit (Python library `scipy.interpolate.RectBivariateSpline` [33]) was used to fit the experimental data, giving a smoothness-factor. This smoothness-factor was iterated for every data set such that the experimental amplitude profile at the modulation frequency is accurately reproduced. To do so, for every tested smoothness-factor, the amplitude profile was calculated and it was checked whether it agreed with the experimentally obtained one within the error bars. The code starts with too much smoothing such that the result is the most smooth fitting that still preserves the amplitude profile at the modulation frequency.

The comparison of the smoothed amplitude profile and the experimental one was carried out for $0.2 < \rho_\varphi < 0.8$ to neglect effects in the core (e.g. sawteeths) and at the edge. For the density n_e and all temperatures an agreement of 90% was demanded, while for the rotation data 80 % agreement was used since its amplitude profile is usually quite noisy. A vanishing gradient was imposed as a boundary condition for $\rho_\varphi = 0$ to demand continuous radial symmetry for all profiles.

The errors on the amplitude and phase profiles were calculated by creating distributions starting from the experimental value, adding or subtracting Gaussian noise with a standard deviation of the error from the data. After that, the Fourier transformations were performed. Finally, for every radial point of all the different amplitude and phase profiles, the standard deviation was calculated. This standard deviation is considered as the error on this datapoint.

NBI power P_{NBI}

For the power of the NBI one gets eight time traces, one for every source. For the calculations in this thesis, the signal was flattened: either a zero signal or an average value over the time when the NBI was injecting. Trips were removed with an average.

ECRH power P_{ECRH}

Piggyback on the discharges considered in this thesis, ECRH tests of the gyrotron deposition were carried out with high-frequency, low-power modulation of one gyrotron. This modulation does not impact the experiments, but in order not to recover this modulation in the conductivities, the ECRH power was flattened. One has to take care that a possible ECRH modulation with lower frequency is not destroyed by this fitting approach.

Effective charge Z_{eff}

The Z_{eff} data from the CXRS diagnostics was also smoothed in time to minimize noise in the calculations using a 1D spline interpolation (Python library `scipy.interpolate.splrep` [33]).

TRANSP

The TRANSP code is developed at Princeton Plasma Physics Laboratory (PPPL) and was used in this thesis to calculate the heat fluxes and the torque from the NBI via the NUBEAM code [34].

TRANSP is basically used to calculate the particle and the energy transport in a tokamak by analyzing the current diffusion and particle and energy conservation equations. It makes it possible to access quantities which are not straightforward to measure in an experiment such as conductivities. Since the basic code framework works with an iterative approach, a high reliability on the input data is necessary.

NUBEAM is part of the TRANSP library, based on a Monte Carlo approach and is used to calculate the NBI power deposition, the driven current, the momentum transfer, and other quantities related to the NBI. It takes various physical effects into account such as the beam geometry and composition, the various particle interactions, the diffusion of fast ions, instabilities and Larmor radius effects [35].

Due to the statistical approach, one has to provide enormous parallel computing power to effectively run the code. In order to obtain smooth torque profiles, the Monte Carlo calculation is carried out with a high amount of test particles. While 20.000 are commonly used in this code, for the calculation in this thesis 200.000 were used, which directly increases the computation time, but decreases the error bars on the results.

The following quantities in Table 3.1 are required inputs to TRANSP. They were fit as described previously in Section 3.2.

Symbol	**Suffix**	**Description**	**Source**
n_e	`NE`	electron density	`NE` from `IDA`
T_e	`TE`	electron temperature	`TE` from `IDA`
T_i	`TI`	ion temperature	`TI_c` from `CMZ,CEZ`
v_{rot}	`VROT`	plasma rotation	`VROT` from `CMZ,CEZ`
Z_{eff}	`ZEF`	effective nuclear charge	`ZEFF` from `CER`
P_{ECRH}	`ECH`	ECRH power	`PECRH` from `ECS`
P_{NBI}	`NBI`	NBI power	`PNI` from `NIS`

Table 3.1: TRANSP input quantities fitted with own code

Besides these basic profiles and time traces, the `trview` code written by Dr. Giovanni Tardini, available on the TOK cluster at IPP Garching, prepares a set of other quantities, e.g. the loop voltage U_{loop}, the safety factor q, the toroidal magnetic field B_φ, and the plasma current I_p. Furthermore, the code adds geometry data about the heating devices, the vacuum vessel, and the plasma LCFS taken from the IDE diagnostic.

All TRANSP calculations carried out in this thesis used the same TRANSP input settings. These are given in Table A.5. The author would like to mention the inconsistency of setting the atomic weight of impurity to 12, considering carbon, whereas boron was used for all the other calculations. This does not have an effect on the calculations carried out in this thesis since neoclassical effects are not considered and Z_{eff} was provided as an input.

The TRANSP calculations were submitted via the `tr_gui` code, which was written by Dr. Giovanni Tardini and is available on the TOK cluster at IPP Garching, to the TRANSP-cluster running at Princeton Plasma Physics Laboratory (PPPL) [36].

GKW

The nonlinear *gyrokinetic flux tube code* (GKW) is used for the simulation of instabilities and turbulent transport and was used in this thesis to predict the Prandtl number and the pinch velocity. The code considers the effects of kinetic electrons, electromagnetic effects, collisions, MHD equilibria coupling of the geometry, and the $E \times B$-shearing. To solve the underlying gyrokinetic equations, a parallel approach is taken [37, 38, 39].

Depending on the type of results, the simulation can be carried out with a linear or a nonlinear system of equations in the local flux-tube geometry or in a finite radial domain, i.e. a global geometry. Calculations with a higher domain size as well as the nonlinear calculations require a significantly higher amount of computational power.

For simplification, the distribution function of the gyrokinetic theory is solved up to first order in the Larmor radius over the major radius. All quantities are normalised, e.g. velocities with respect to the thermal velocity. The calculations are performed in Hamada coordinates, where contravariant components of the poloidal and toroidal magnetic field are flux functions. Furthermore, pseudo-spectral methods are used such that all quantities are represented by Fourier modes.

In the calculations performed in this thesis, a linear set of equations was considered in a local form. The toroidal momentum flux was also calculated quasi-linearly. The following quantities in Table 3.2 were passed in an ASCII input file. All data were time-averaged and consistent with those given to TRANSP and later to ASTRA for the transport simulations.

Symbol	**Description**	**Type**	**Comment**
#	discharge number	scalar	
t_{Begin}	start time	scalar	
t_{End}	end time	scalar	
$\#(\rho_\varphi)$	number of toroidal points	scalar	
ρ_φ	rho toroidal	profile	radial linear grid
T_i	ion temperature	profile	`Ti_c` from `CMZ,CEZ`
T_e	electron temperature	profile	`TE` from `IDA`
Ω	Angular velocity of the plasma	profile	`VROT` from `CMZ,CEZ`
n_e	electron density	profile	`NE` from `IDA`
n_{imp}	impurity density (boron)	profile	`nimp` from `CES`
Z_{imp}	Z_{eff} of main impurity	scalar	$= 5$ for boron
f	impurity density scale factor	scalar	$\overline{Z_{\mathrm{eff,exp}}}/(Z_{\mathrm{imp}}^2 - Z_{\mathrm{imp}}) \cdot \overline{n_e}/\overline{n_{\mathrm{imp}}}$
Z_{eff}	effective nuclear charge of plasma	profile	$(Z_{\mathrm{imp}}^2\, f\, n_{\mathrm{imp}} + n_D)/n_e$
n_D	deuterium density	profile	$n_e - Z_{\mathrm{imp}} f n_{\mathrm{imp}}$
	fast ion density	profile	`BDENS` from TRANSP
	fast ion temperature	profile	`BDENS`$/e \cdot (2 *$ `UBPRP` $+$ `UBPAR`$)/3$ from TRANSP

Table 3.2: GKW input quantities

Based on this information, local normalized logarithmic temperature and density gradients are calculated. The electron and ion temperatures and densities are used to calculate the local collisionality and the normalized pressure. The safety factor, the magnetic shear and other geometric parameters define the local metric tensor. All of this information together is used to reconstruct a numerical magnetic equilibrium, which is computed with *CHEASE* from the *CLISTE* code [37].

To calculate quantities such as the Prandtl number Pr and the pinch, the difference is taken between runs in which the local plasma rotation and its gradient are included or set to zero, respectively. The quasi-linear fluxes are calculated over a spectrum of five binomial wave numbers, covering the range from $\rho_\varphi = 0.2 \ldots 0.8$. In the way the calculations were performed, only ratios between the transport coefficients can be considered, such as the Prandtl number or the pinch number $R\, v_{\mathrm{Pinch}}/\chi_\varphi$ [40].

The Prandtl number is one of the most robust predictions for momentum transport for gyrokinetic theory, since it does not depend on symmetry breaking mechanisms [40].

ASTRA

The *Automatic System for TRansport Analysis* code (ASTRA) is a well-established tokamak transport code to solve analytically the strongly coupled set of the various transport equations. It is an optimal tool in which to implement a transport model (cf. Chapter 2) to compare the experimental values of the plasma rotation with the simulated one.

Due to the coupling of the different quantities in transport studies, even small changes in the data can strongly impact the results. To face this problem and to supply transport modeling with a tool to test empiric models, the ASTRA code provides a flexible programming system for predictive and interpretative transport modeling and can be used for stability analysis or for processing experimental data [41, p. 7]. It is considered to be a 1.5D code, solving diffusion equations, e.g. those for the densities and temperatures, 1D over the radius and treating the equilibrium in 2D. For further insight into the large amount of implemented effects and equations, the reference paper is recommended [41, Chapter 3].

Dr. Emiliano Fable implemented the parallel momentum conservation equations in ASTRA [42]. This set of equations is used to solve for $v_{\|}$ and to compare it with the experimentally measured v_{rot}.

ASTRA not only provides an extensive library describing all relevant physical effects, but also a supervising shell to debug the model and a graphical user interface to provide direct insight into the simulations. Routines to save the time traces of the calculated scalars and profiles can be used.

The input consists of four parts. First, an `equ`-file which sets up the physical model. Second, an `exp`-file setting up basic parameters and linking to the experimental data used for the simulation. Third, a `udb`-database with all the experimental data itself. Last, a `log`-file which makes it possible to pass constants or variables.

In this work, the `log`-file is simply used to provide the transport coefficients of the model to the code, namely `CHE1`, `CHE2`, and `CHE3`. There are two further lines worth mentioning and shown in the Appendix in Table A.2. Python scripts were designed by the author to write the `udb`-database and the `exp`-file. For the database, the quantities shown in Table 3.3 of the output of a TRANSP run were written out to ASCII files. Not all of these quantities were finally used for calculations in this thesis, but are available in ASTRA.

Abbreviation	**Description**	**Source**
`MU`	safety factor	fitted experimental data
`NE`	electron density	fitted experimental data
`TE`	electron temperature	fitted experimental data
`TI`	ion temperature	fitted experimental data
`OMEGA`	toroidal rotation	fitted experimental data
`ZEF`	effective nuclear charge	fitted experimental data
`PRAD`	radiated Power	fitted experimental data
`CONDI`	ion heat diffusivity	TRANSP calculation
`CONDE`	electron heat diffusivity	TRANSP calculation
`CHPHI`	effective momentum diffusivity	TRANSP calculation
`ESRC`	electron source	sum of `SBE`+`SCEV` from TRANSP
`TQIN`	torque	TRANSP calculation
`UFASTPP`	perpendicular fast ion velocity	TRANSP calculation
`UFASTPA`	parallel fast ion velocity	TRANSP calculation
`BDENS`	fast ion density	TRANSP calculation
`EHEAT`	electron heating power density	TRANSP calculation
`IHEAT`	ion heating power density	TRANSP calculation

Table 3.3: ASTRA input profiles

Besides linking the ASCII files to the right ASTRA variable names, the `exp`-file provides the quantities given in Table A.3. Data imported following the `exp`-file can be accessed from the `equ`-file by appending an `X` (e.g. `CAR1X` for `CAR1`). The fourth part of the input requires to set up the actual physical model in the `equ`-file. The variable names given in Table A.1 are relevant for the understanding of the models and not intuitive by themselves. The model used for calculations in this thesis was implemented in the `equ`-file as shown in Table A.4.

Starting from these four different input types, ASTRA calculates the toroidal momentum transfer with the given transport parameters and gives the parallel velocity `UPAR` $= v_{\|}$ as a result. This allows for comparing the calculated parallel velocity to the experimentally measured toroidal rotation to evaluate the quality of the model.

As a caveat, the experimental rotation data is used to impose a boundary condition (cf. [6, p. 4] and [22]). Setting the boundary to `CBND4` $= 0.8$ in the calculations for this thesis, the range of interest for the evaluation of the data is $\rho_\varphi < 0.8$. By doing so, edge effects are not considered within the work of this thesis.

Calculation of transport parameters

After smoothing and fitting the data, calculating the torque of the NBI with TRANSP, and obtaining a prediction for the Prandtl number with GKW, one has to test different parameters for the transport model implemented in ASTRA.

These three parameter, `CHE1`, `CHE2`, and `CHE3`, span a too large parameter space to carry out this optimization manually. To automatize this and provide errors on the results, a parallel approach on the TOK cluster was implemented.

Testing of these parameters is conducted with a scan on a grid of different candidates. As an input, the upper and lower limit and the total number of values for each parameter are given. For every combination, an ASTRA runs is performed. Here it should be noted that all ASTRA calculations within this thesis were started 0.3 s prior to the time span of interest to exclude equilibration effects.

After ASTRA writes the results of each simulation, the `quality` value

$$\texttt{quality} = \log \sum_{t=t_{\mathrm{Begin}}}^{t_{\mathrm{End}}} \sum_{\rho_\varphi=0.2}^{0.8} \left(v_{\|,\ \mathrm{ASTRA}}(t,\rho_\varphi) - v_{rot,\mathrm{EXP}}(t,\rho_\varphi)\right)^2 \tag{3.1}$$

is calculated.

The set of transport parameter with the smallest `quality` value is chosen to be the one best representing the experimental values. This is basically a least-squares fit where the logarithm was used to avoid large numbers.

As an alternative, one can concentrate on the changes of the profile to fit the amplitude and phase profiles. To do so, one subtracts the time-averaged values

$$\texttt{quality} = \log \sum_{t=t_{\mathrm{Begin}}}^{t_{\mathrm{End}}} \sum_{\rho_\varphi=0.2}^{0.8} \left(\left(v_{\|,\ \mathrm{ASTRA}}(t,\rho_\varphi) - \overline{v_{\|}(\rho_\varphi)}\right) - \left(v_{rot,\mathrm{EXP}}(t,\rho_\varphi) - \overline{v_{\mathrm{rot}}(\rho_\varphi)}\right)\right)^2. \tag{3.2}$$

After such a minimization, one obtains a set of transport parameter. Using the obtained parameter, one can plot the corresponding simulated rotation data and the experimental data to compare by eye.

Error estimates on the transport coefficients and calculated profiles are obtained by testing different deviations from the optimized results. If the resulting rotation does not deviate by more than the experimental errors on the steady-state profile of the rotation data, the deviation is increased until leaving the error bars. The largest deviation from the optimized parameters still being within the error bars is considered as the uncertainty with which one can carry out the optimization.

3.3 Overview of the workflow

In the following sketch, the flow of data is depicted. One gets an impression of how many quantities and diagnostics contribute to the optimization process.

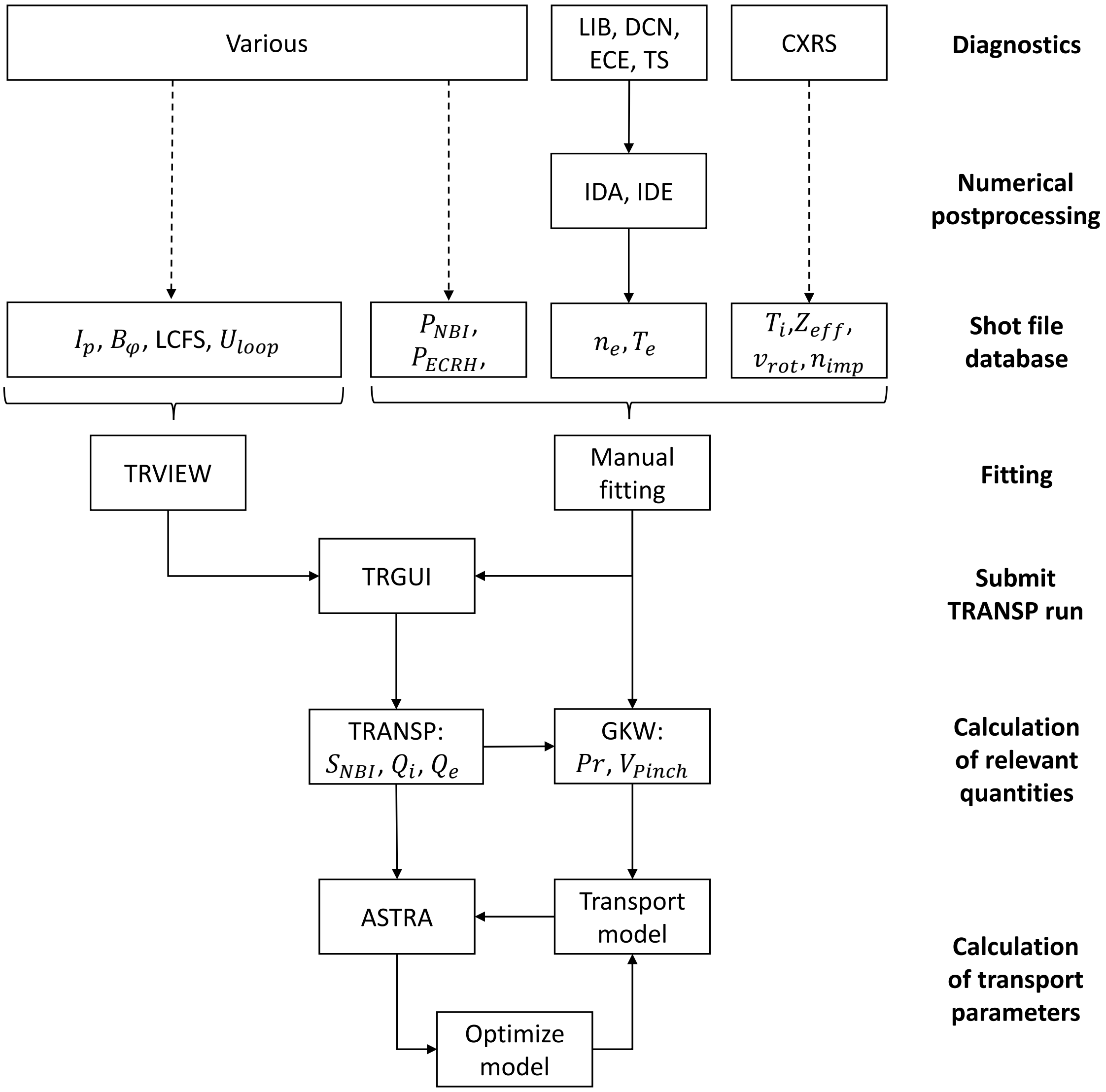

Figure 3.1: Flow of data within the used method to find transport coefficients

Chapter 4

Experimental Setup

The experimental data used in this thesis was obtained in NBI modulation experiments. In this chapter the basic idea of such experiments is introduced and the resulting profiles are discussed. Finally, the selection of the used data sets is justified.

4.1 NBI modulation experiments

To modulate the applied momentum of the plasma, the NBI power is modulated: the neutral particles are injected in periodical pulses of a given frequency f_{mod} as depicted in Figure 4.1. This modulates the heat and momentum from the NBI, causing a perturbation of the ion temperature and the plasma rotation as shown in Figure 4.2.

In order to keep the perturbation small, only one source is modulated with reduced voltage. Using the other NBI source with constant power and regular voltage is needed to use the CXRS. Having a smaller perturbation on top of a constant heating aims to keep the diffusivities as constant in time as possible.

The temporal perturbation allows one to consider the momentum conservation Equation 2.1 to be time-dependent and extract more information from the data by calculating amplitude and phase profiles of the rotation modulation. The phase is calculated with respect to the NBI modulation. These profiles are obtained by calculating the Fourier transformation for a given radial channel of a data set and by then picking the amplitude and phase of the modulation frequency and plotting these over the radius as shown in Figure 4.3.

Among the discharges performed for this thesis, different torque perturbations were imposed. The background profiles for n_e, T_e, T_i, and v_{rot} where kept identical within error bars. Therefore, the different discharge profiles coincide for the steady state (cf. Chapter 4.4), but differ in the amplitude and phase profiles as shown in Figure 4.4 for a subset of discharges. On hopes that the perturbation is small such that modeling is easier, e.g. the Prandtl number does not modulate. For identical steady-state background profiles, the transport coefficients must be the same, independent of the variation due to the perturbation. If this is the case, one should be able to find an unique set of transport parameter modeling all considered discharges.

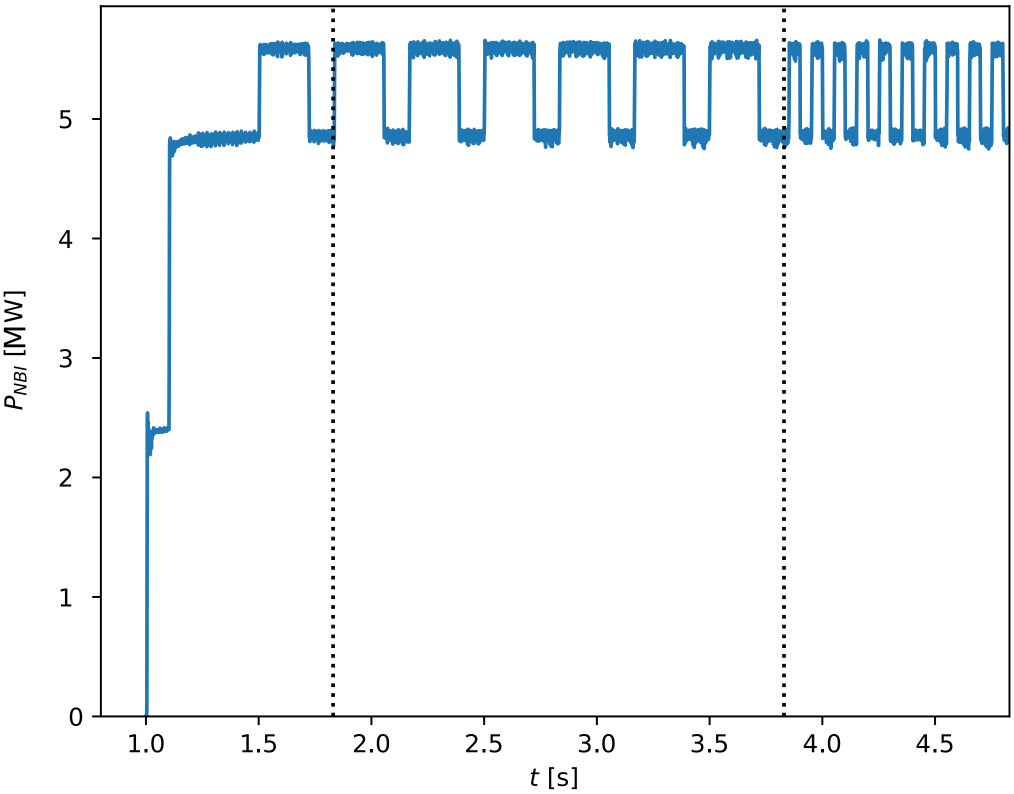

Figure 4.1: Modulated NBI power, #34027, used analysis window marked with dotted lines

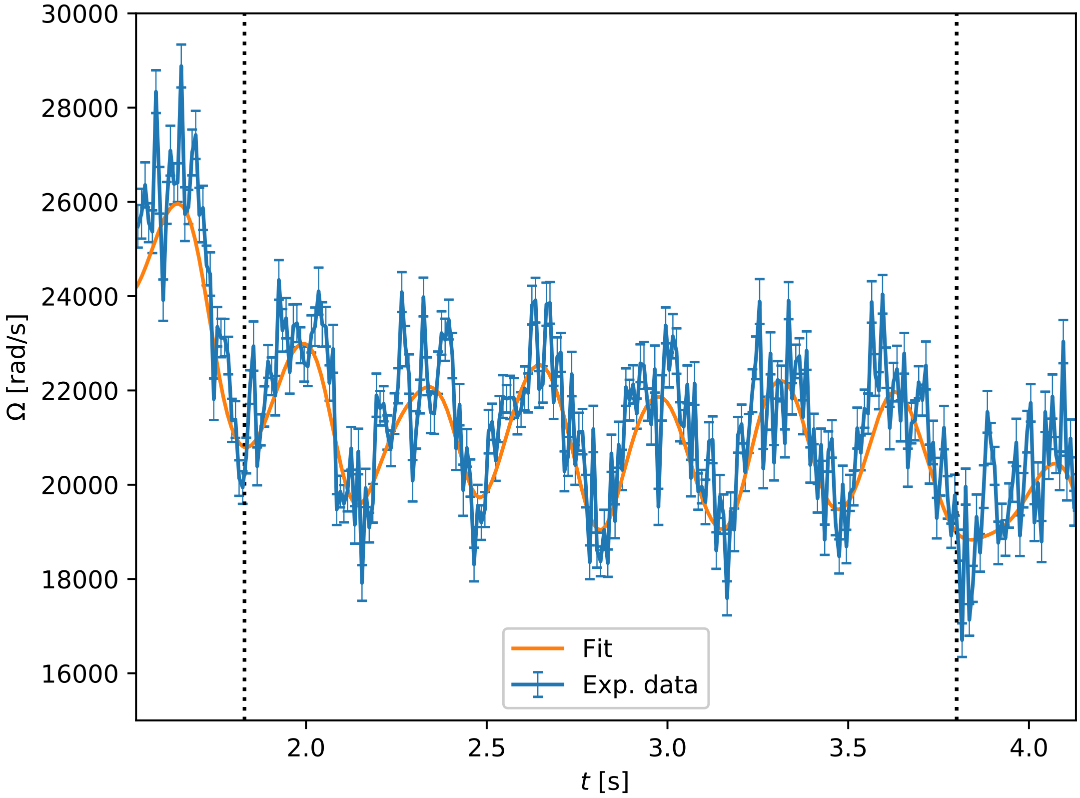

Figure 4.2: Modulated rotation, #34027, $\rho_\varphi = 0.5$, used analysis window marked with dotted lines

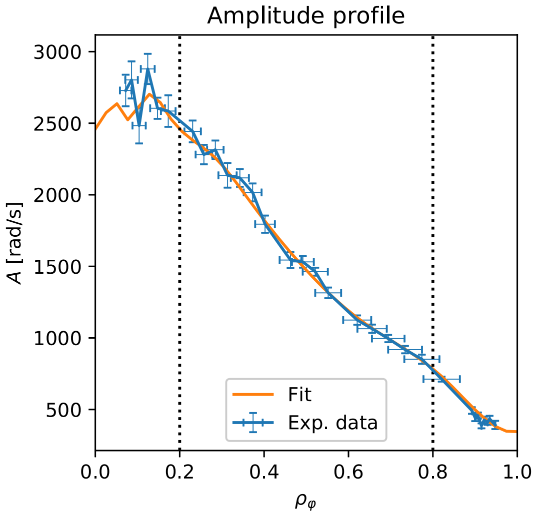

Figure 4.3: Amplitude and phase profile of the rotation, #34027, $f_{\mathrm{mod}} = 3$ Hz, range of interest for analysis marked with dotted lines, outside this range a smoothing-out and non-agreement is justified in order to avoid unphysical steep gradients and behavior

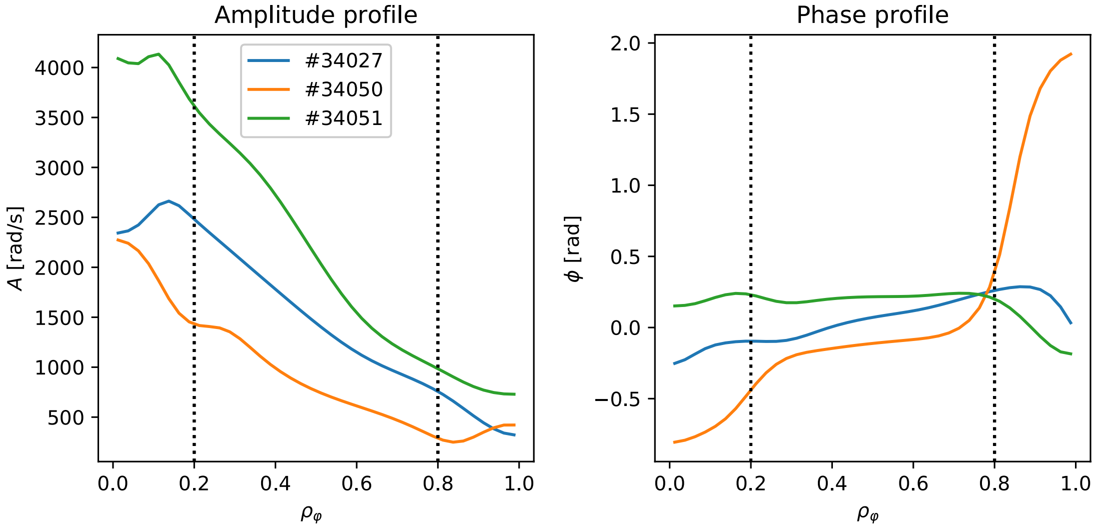

Figure 4.4: Amplitude and phase profiles of the fitted rotation, $f_{\mathrm{mod}} = 3$ Hz, range of interest for analysis marked with dotted lines

4.2 Performed discharges

In the following, the performed discharges with a $f_{\mathrm{mod}} = 3$ Hz are listed and basic plasma parameters are given.

#	**NBI mod. power [MW]**	**RF mod. power [MW]**	**Comment**
34027	0.744 on-axis	0	reference discharge
34042	0.716 off-axis	0	off-axis discharge
34047	0.751 on-axis	0	repeated reference discharge
34048	0.748 on-axis	1.15	ECRH modulated in phase
34049	0.752 on-axis	1.15	ECRH modulated out of phase
34050	0.753 on-axis	1	ICRH modulated in phase
34051	0.754 on-axis	1	ICRH modulated out of phase
34062	0.749 on-axis	0	no ECRH or ICRH
34063.1	0.749 on-axis	0.6	ICRH modulated out of phase
34063.2	0.749 on-axis	0.3	ICRH modulated out of phase

Table 4.1: Performed NBI modulation discharges

Main differences lie in the modulation of the ECRH and ICRH. Their power was modulated to either match the phase of the NBI modulation or to modulate counter-phase with the goal to either keep the T_i constant or to maximize the modulation in the ion temperature. A changing T_i leads to a modulating ion heat diffusivity and thus influences the Prandtl number and yields new insights to be analyzed. Beside #34062, where the ECRH tripped, $P_{ECRH} \approx 0.6$ MW was applied to avoid tungsten accumulation. The different NBI modulation modifies the rotation. All in all, this provides the possibility to study the effects of different modulated perturbations.

All discharges were performed under standard conditions: high confinement mode, a toroidal field of $B_\varphi \approx 2.5$ T, a plasma current of $I_p \approx 0.8$ MA, and a *lower single null* (LSN) configuration with an outer plasma position of $R_{\mathrm{aus}} = 2.15$ m to provide optimal conditions to the CXRS diagnostics and optimize the results of the DCN. All relevant quantities are shown in the overview plot in Figure 4.5. There one can clearly see how steady the pulses are in time.

It should be noted that NBI modulation experiments with $f_{\mathrm{mod}} = 7$ Hz and $f_{\mathrm{mod}} = 10$ Hz were also carried out in separate phases of these discharges, but are not part of this thesis. These cases include additional variations in applied NBI perturbations and thus analysis will be the subject of future work.

4.3 Data verification

The discharges listed in Table 4.1 were analyzed carefully in order to avoid systematic mistakes, like using wrong time windows or applying averages where these are not justified.

Selection of time windows

As a general rule, not all modulation cycles within the given data sets were used for analysis. The first modulation cycle was neglected to avoid ramp-up effects in the data. The time windows for analysis were manually set with the first rising flank of the NBI as t_{Begin} and ended at t_{End} with a multiple of the modulation period.

To support clean Fourier transformations, the overall time window has to be a multiple of the modulation period time. To prove this, the overall length of the time window T_{ges} was calculated and the numbers of NBI modulation cycles were counted. One calculates the resulting modulation frequency $f_{mod,eff}$ which can be compared with the used $f_{\mathrm{mod}} = 3$ Hz. This calculation is shown in Table 4.2.

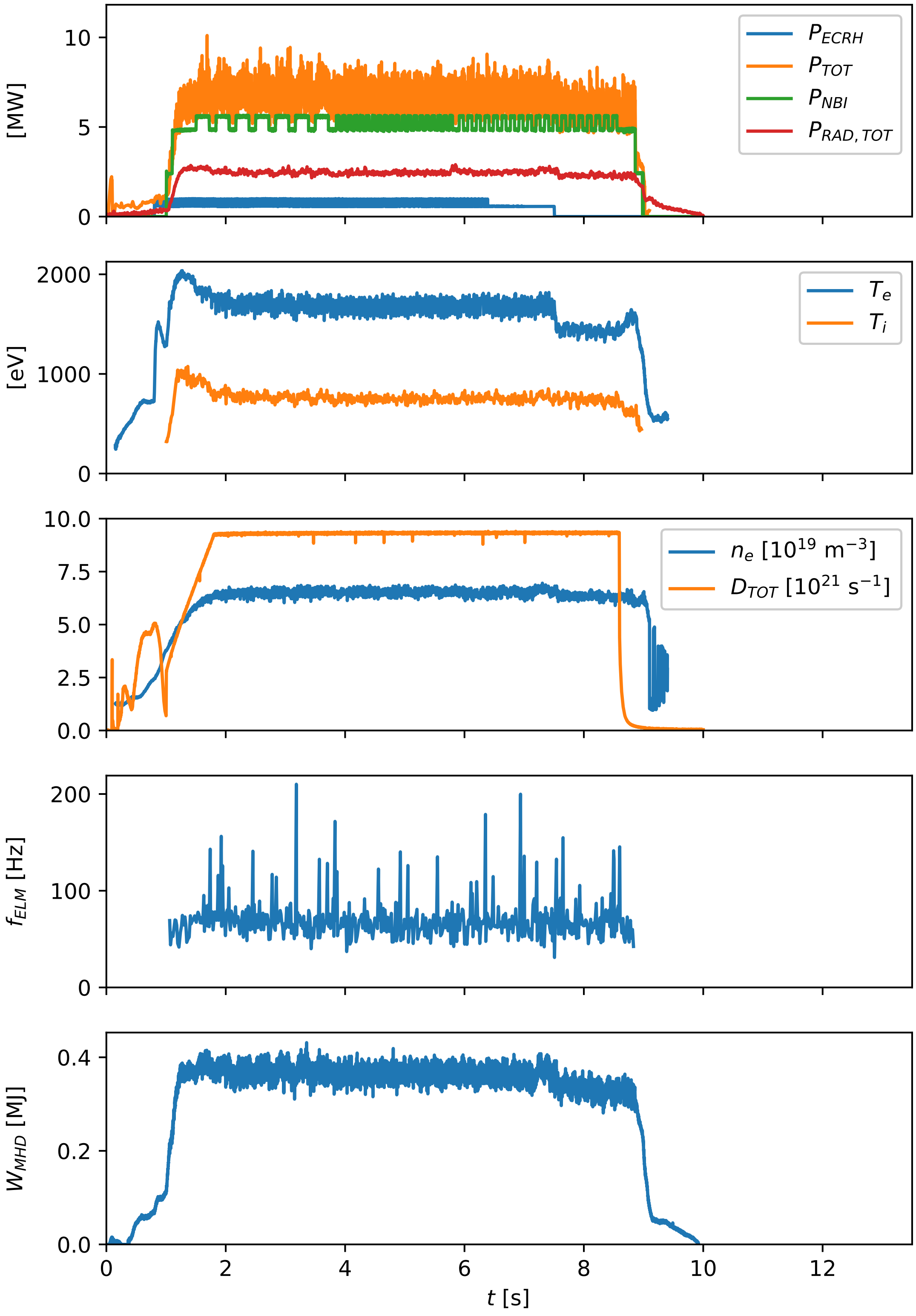

Figure 4.5: Basic time traces of the reference discharge #34027, profiles are radius averaged. First, a 3 Hz NBI modulation is imposed, then 10 Hz and 7 Hz.

#	t_{Begin} [s]	t_{End} [s]	T_{tot} [s]	**mod. cycles**	$f_{\text{mod,eff}}$ [Hz]
34027	1.832	3.847	2.015	6	2.978
34042	1.834	5.829	3.995	12	3.004
34047	1.829	3.83	2.001	6	2.999
34048	1.831	2.831	1	3	3
34049	1.834	2.831	0.997	3	3.009
34050	1.831	3.831	2	6	3
34051	1.829	3.831	2.002	6	2.997
34062	3.645	8.304	4.659	14	3.005
34063.1	3.645	5.976	2.331	7	3.003
34063.2	5.976	8.304	2.328	7	3.007

Table 4.2: Chosen time windows for the analysis

The last column shows that the chosen time points reflect the $f_{\text{mod}} = 3$ Hz well and one can be certain that no offsets in the Fourier transformation are introduced.

Applied heating power

The applied heating power has an enormous impact on the background profiles. Therefore, the total applied heating powers were compared. To do so, the sum of the time-averaged contributions of the NBI, the ECRH, and the ICRH (where applied) were calculated.

#	$\overline{P_{TOT}}$ [MW]	**Dev. from avg. in %**
34027	5.95	-3.4
34042	5.93	-3.8
34047	5.96	-3.3
34048	6.75	**9.6**
34049	6.27	1.8
34050	6.76	**9.7**
34051	6.36	3.3
34062	5.36	**-13**
34063.1	6.19	0.5
34063.2	6.07	-1.4

Table 4.3: Applied averaged power in the considered discharges

The discharges #34048, #34050, and #34062 are clear outliers that raise suspicion if these discharges have dissimilar background profiles compared to the others.

Stability of equilibrium

The equilibrium of the magnetic field is an important input to the simulations. A time-dependent equilibrium would drastically increase computational time especially for the ASTRA calculation. Therefore, the equilibrium was examined to see if it was strongly impacted by the power modulations, i.e. if the changes in power caused a non-negligible modulation in the Shafranov shift of the plasma.

To do so, a fixed set of z and R coordinates, corresponding to the nearest approach of the CEZ LOS to the primary beam, was chosen. With the help of the IDE equilibrium, the time-dependent ρ_φ for these spatial points were calculated and a Fourier transformation was performed.

Figure 4.6 shows that the modulation of the ρ_φ for a given spatial point at midradius is negligible. This is a demonstration that the plasma shape was stable and that the applied power modulations were small enough to not induce a significant Shafranov shift.

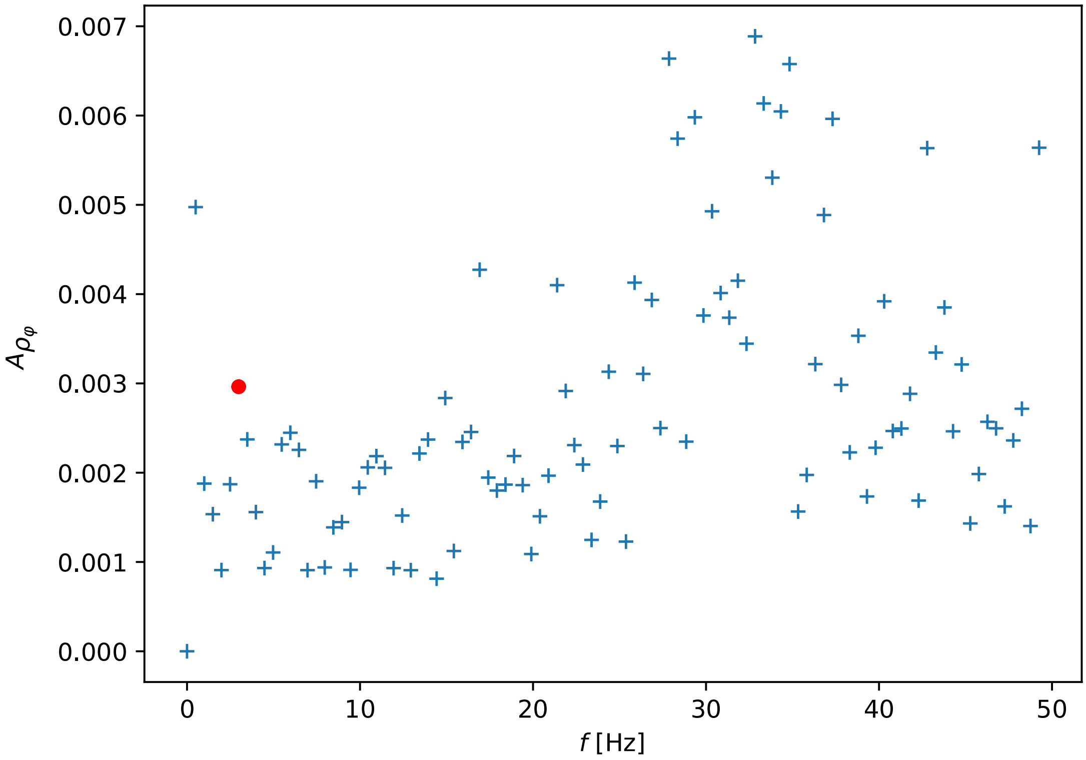

Figure 4.6: Fourier transformation of ρ_φ of a midradius channel, #34027, data from IDE, the NBI modulation frequency $f_{\mathrm{mod}} = 3$ Hz is marked with the red dot

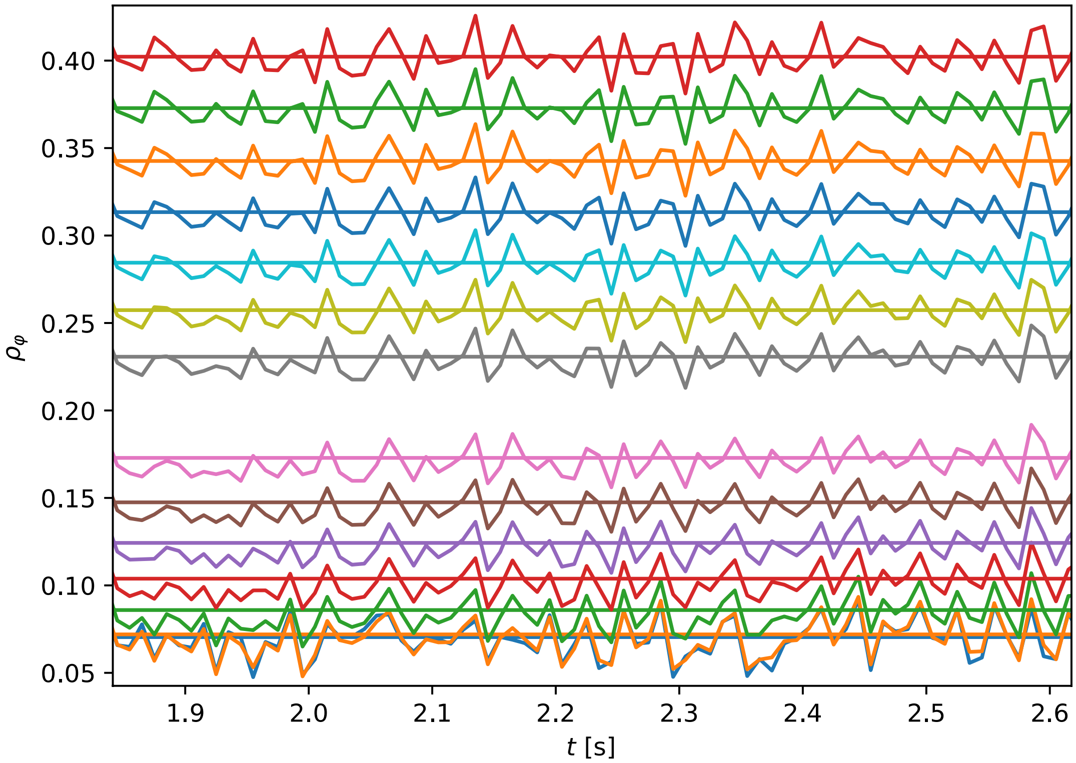

Figure 4.7: ρ_φ for the 14 innermost channels of the CEZ diagnostic, #34027

As a next step, it was proven that there is no general drift of the flux coordinate for a given radial position. To do so, linear and quadratic fits were performed, which all lead to negligible contributions of the linear and quadratic terms. This was done for all radial channels of the CEZ diagnostic and is shown in Figure 4.7. There is no overlap of the channels flux coordinates with the exception of the two innermost channels. To avoid problems in the fitting routines, the innermost radial channel was ignored. Besides that, the analysis yields the assumption of a stable magnetic equilibrium such that time averaging is justified. The LCFS was also observed to be similarily stable.

Averaging window for CXRS data

The numerical postprocessing of the CXRS data offers the possibility to vary the integration time of the diagnostic. Usually one uses 10 ms, but for data with low signal in particular it can be useful to extend this to 20 ms or 30 ms.

Dr. Rachael McDermott wrote shotfiles for the CEZ data with different integration times. This has little effect on the amplitude and phase profiles. Increasing integration time causes a slight decrease of error bars. The reduced noise in the data is balanced by having fewer time points for the Fourier transformation. Therefore, the error bars do not change significantly. Also, the difference in these integration times is still far below the f_{mod}, such that it has no impact on the amplitude and phase values. Concerning the rotation profile, one observes the error bars slightly decrease, but overall, there is no improvement of the signal as depicted in Figure 4.8.

To confirm this behavior, a numerical experiment with simulated data was carried out. In agreement with the experimental observation, it was found that increasing the integration time has no significant impact on the error bars of the amplitude and phase profiles.

In this simulation high time resolution rotation data sets were produced with different error bars on the rotation data itself. Then, different sampling times were applied to the data and the Fourier transformation was carried out. As a result, one obtains the errors of the phases and amplitudes. As one can see in Figure 4.9 and 4.10, the increase of integration time does not significantly decrease the error on the amplitude and phase profiles. An increase of the integration time from 10 ms to 20 ms or 30 ms does not significantly improve the error bars of the rotation, as was seen in the experimental data. It is not worth to recalculate the CXRS data with higher integration time. Furthermore, the right-hand sides of Figures 4.9 and 4.10 reveal the tendency that a smaller integration time decreases the error for the amplitude and phase profiles, because more time points are available for the Fourier transformation.

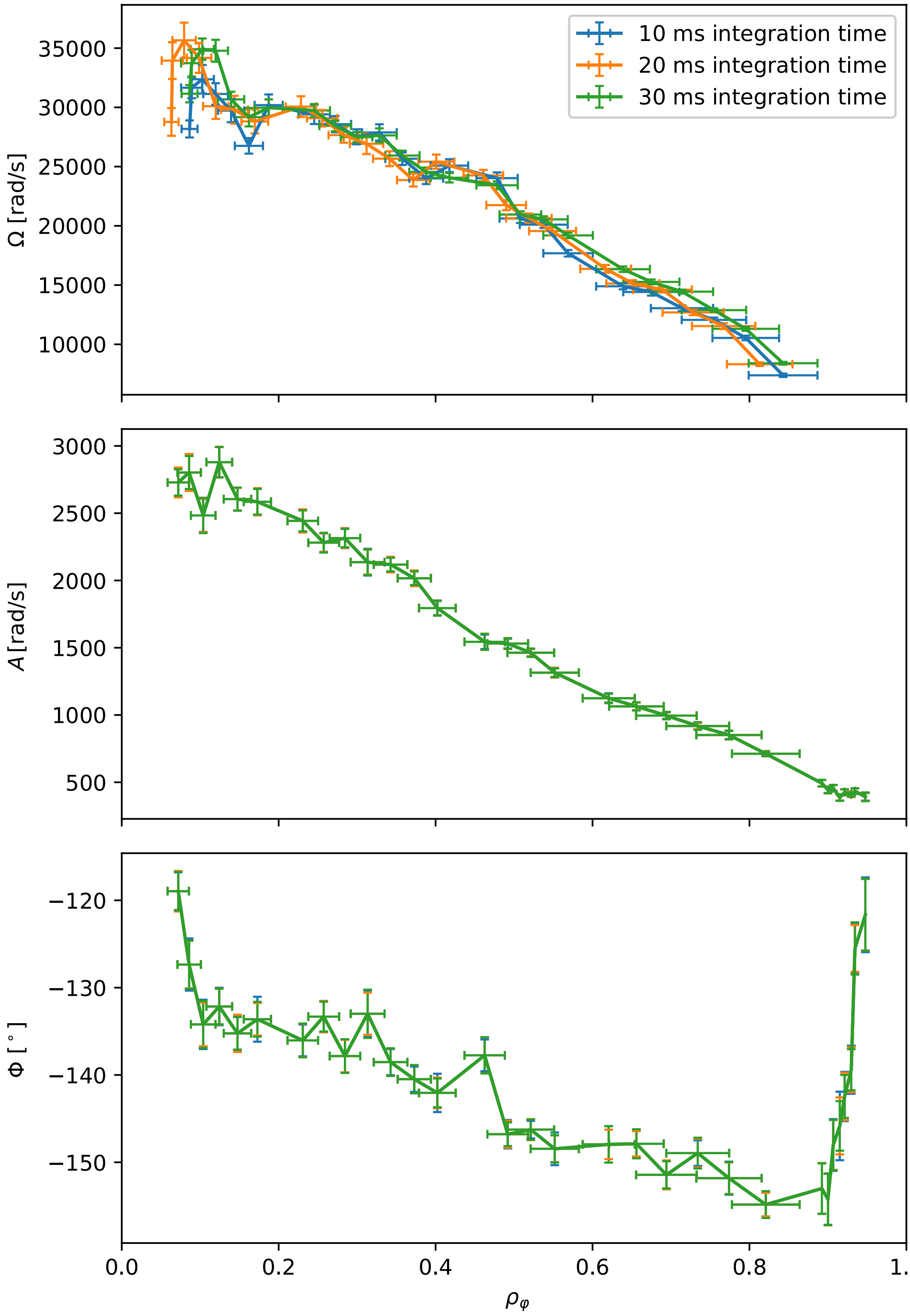

Figure 4.8: Effect of different CEZ integration times, #34027, experimental data. The amplitude and phase profiles are so similar that is it difficult to see the differences.

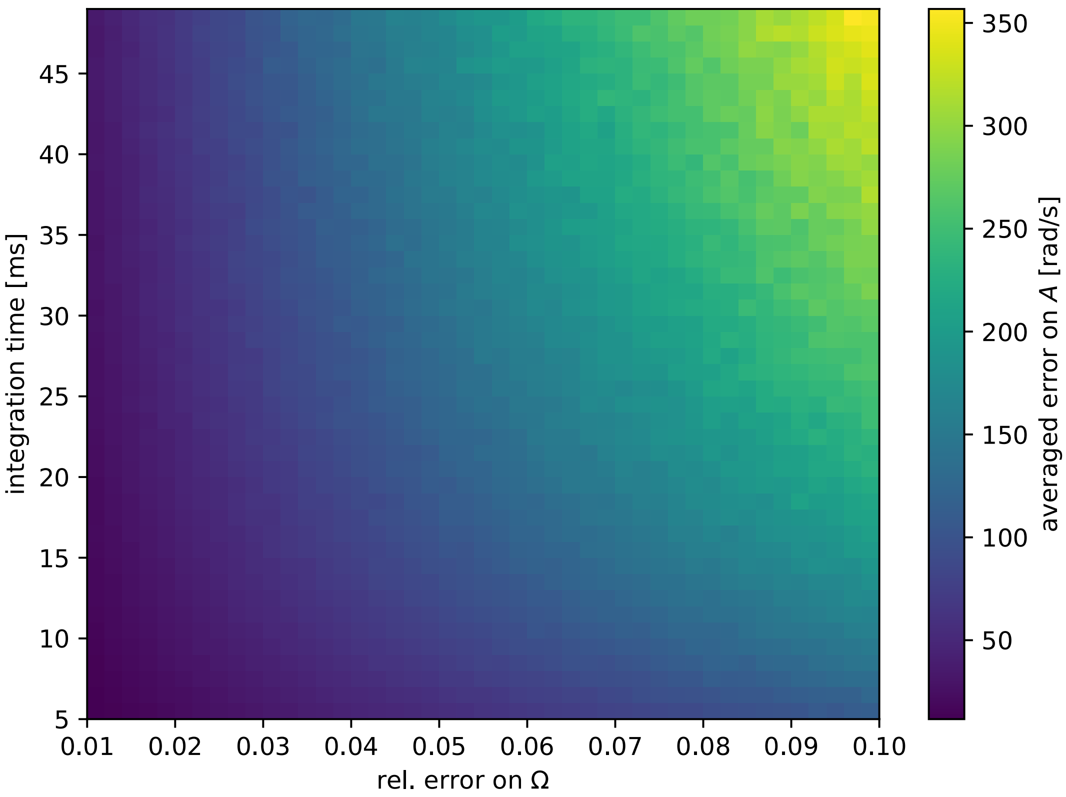

Figure 4.9: Numerical experiment for the rotation data, based on #34027, averaged error on the amplitude depending on the error of the raw data and the integration time

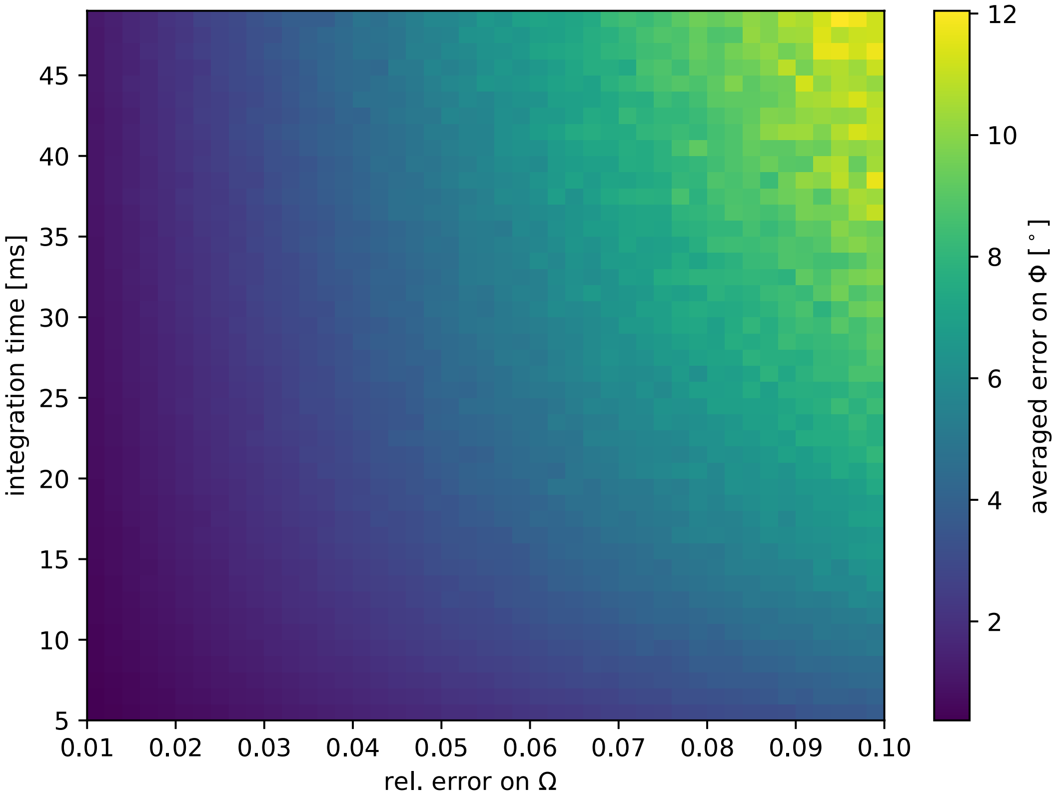

Figure 4.10: Numerical experiment for the rotation data, based on #34027, averaged error on the phase depending on the error of the raw data and the integration time

4.4 Comparison of discharges

Time-averaged profiles of the four most important quantities will be compared in this section for all cases listed in Table 4.1. The size of the error bars on the gradient profiles makes comparisons between the different curves difficult such that they were neglected.

Electron density n_e

In general, all density profiles (cf. Figure 4.11) and density gradient profiles agree within error bars.

The density data was also checked with Fourier methods. Since the density directly enters the transport equations, one demands a negligible modulation of the density to avoid a time-dependence of the transport parameter. As Figure 4.12 shows, the density in discharges #34048 and #34049 is modulated by $\sim 2\%$ which is significantly higher than is seen in the other discharges. These two discharges feature ECRH modulation in addition to the NBI modulation, which causes relatively large perturbations to the electron temperature profile (see Figure 4.13) and, as evidenced by the density profiles, changes in the plasma particle transport. For NBI modulation experiments at ASDEX Upgrade, one expects this behavior, since the fuelling from the NBI is very small. For this reason, these two cases were excluded from the analysis performed in this thesis.

Electron temperature T_e

The electron temperature profiles (cf. Figure 4.14) show that the discharge #34062 is an outlier. The electron temperature is too low, in agreement with the observation in Table 4.3, where this discharge has much lower heating power. In this discharge, the ECRH tripped, the lower heating power leads to a lower temperature.

The analysis of the amplitude profiles of the electron temperature especially reveal that the discharges with ECRH and ICRH modulation (#34048-51) are different as shown in Figure 4.13. These additional modulations clearly cause a perturbation in the T_e profile, which will propagate into the analysis via the electron-ion heat exchange. However, it is not a priori clear that this contribution will be problematic, and, as the steady-state profiles for #34050 and #34051 are in good agreement, only #34048 and #34049 are removed from the data set on account of the transport changes observed in the density profiles.

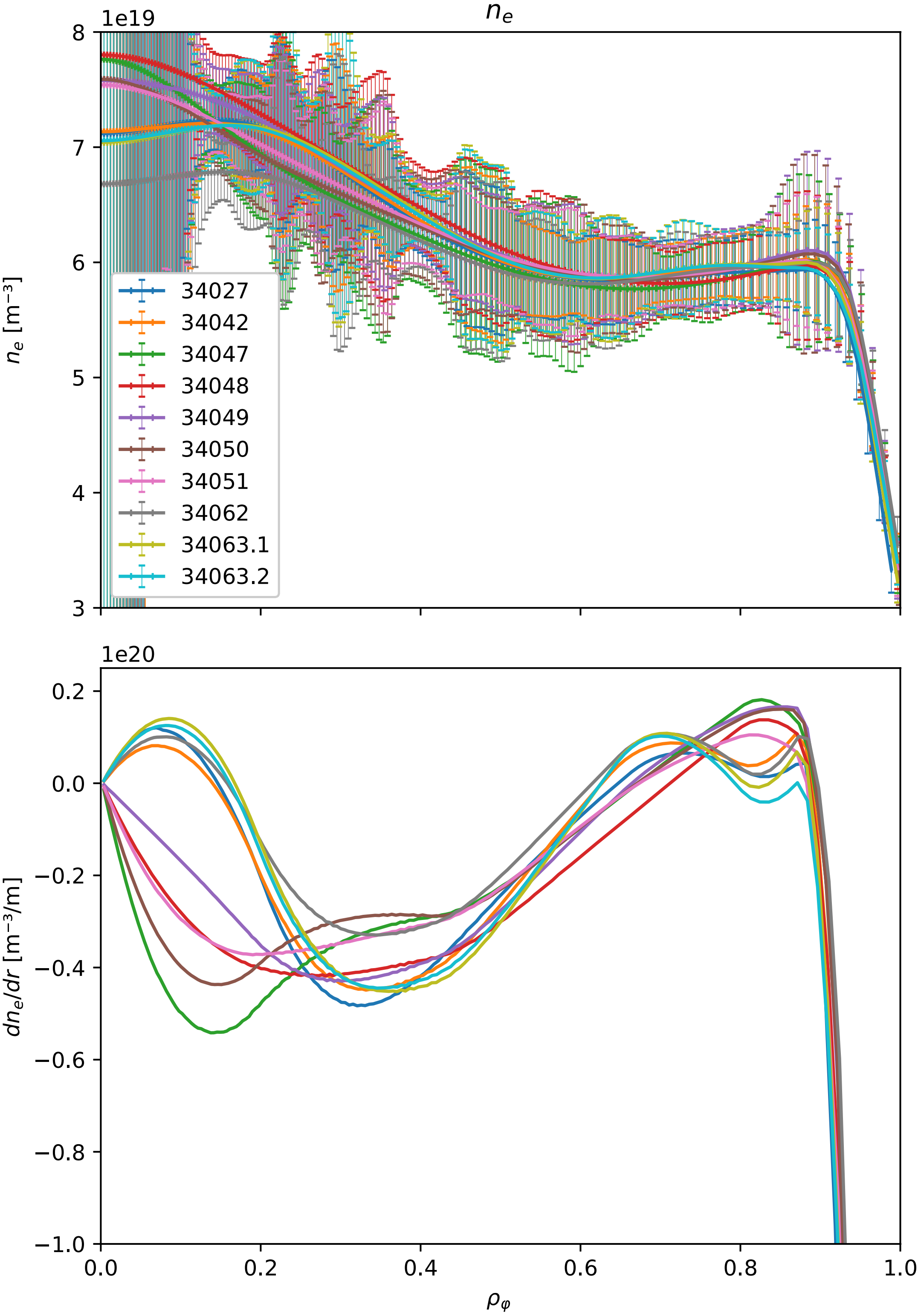

Figure 4.11: Experimental n_e profiles of the considered discharges

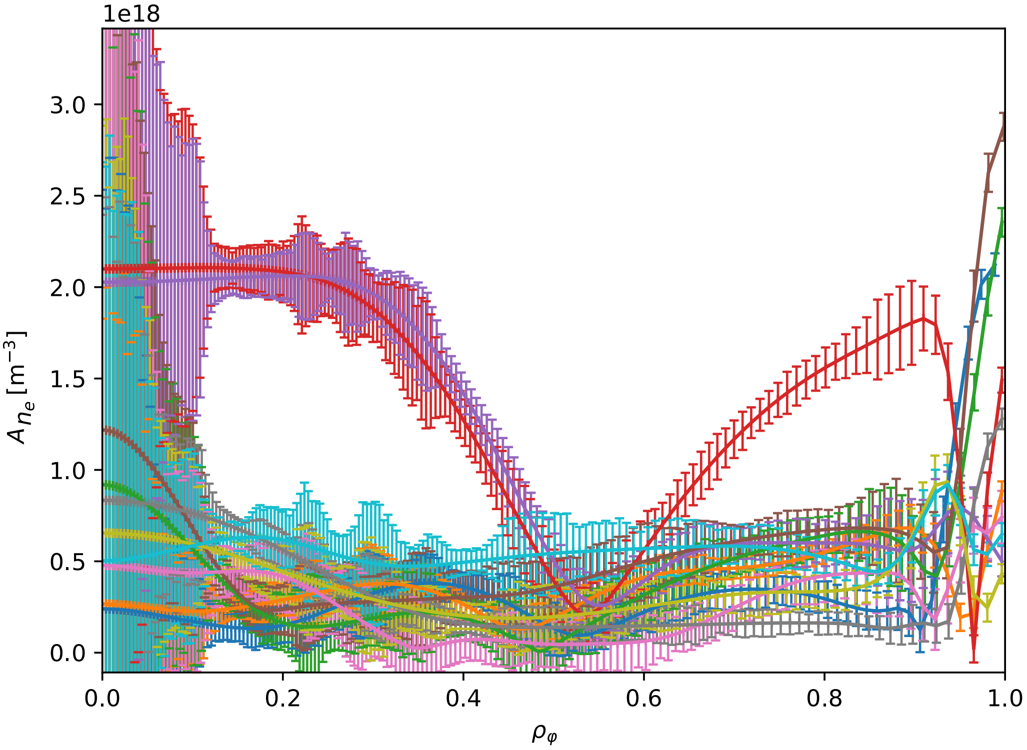

Figure 4.12: Amplitude profiles at f_{mod} for n_e, experimental data from IDA, legend as shown in Figure 4.13 below

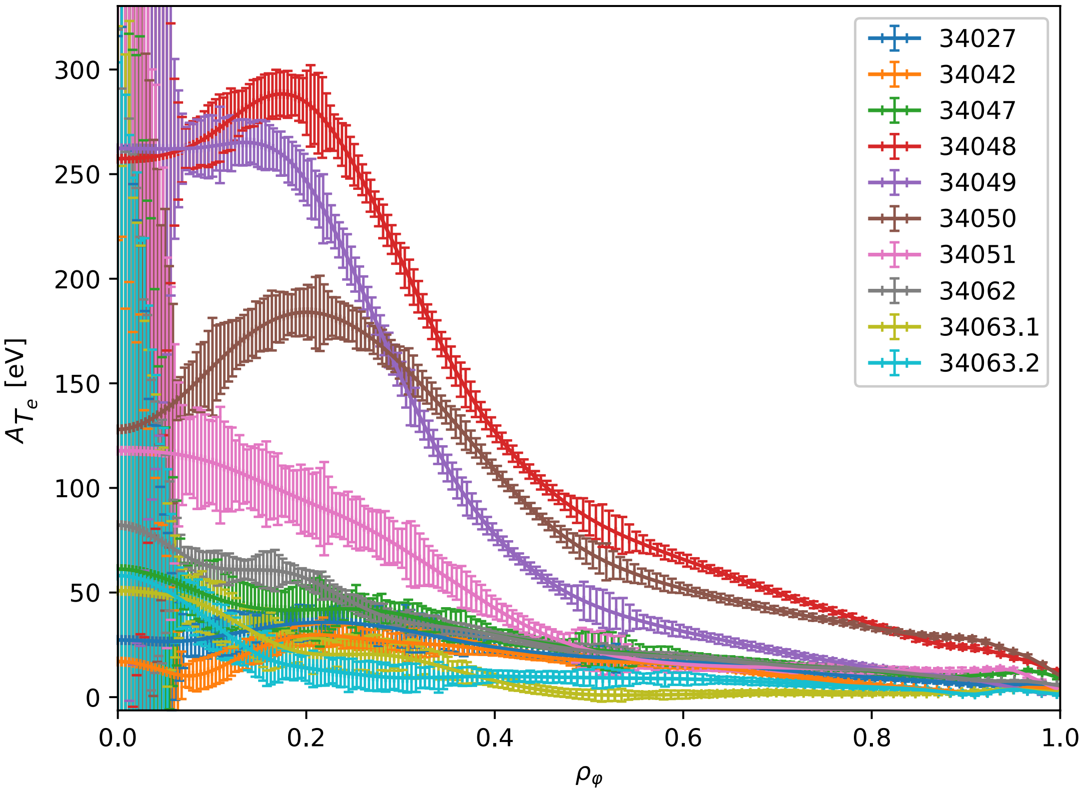

Figure 4.13: Amplitude profiles at f_{mod} for T_e, experimental data from IDA

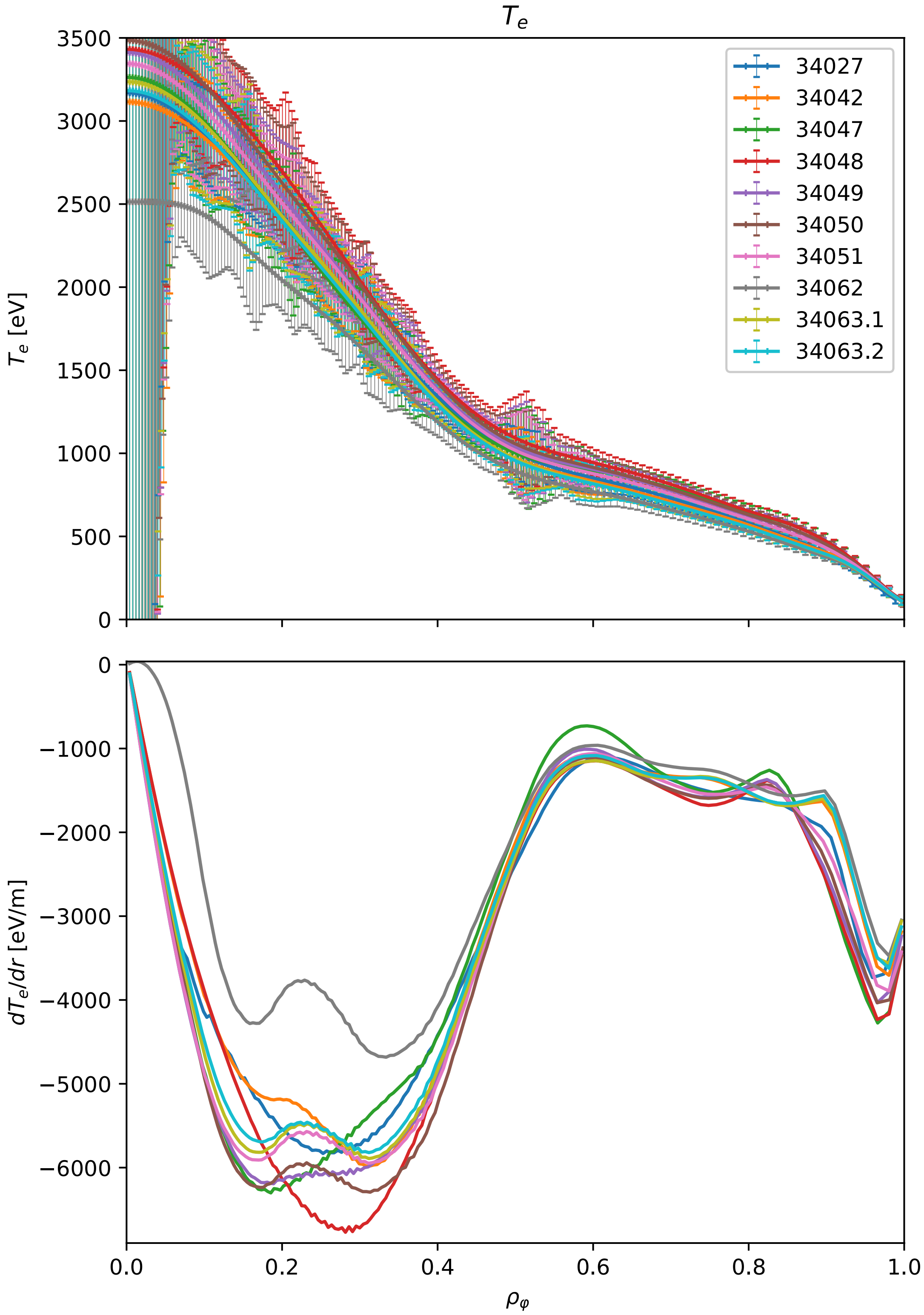

Figure 4.14: Experimental T_e profiles of the considered discharges

Ion temperature T_i

All ion temperature profiles were found to agree within error bars (cf. Figure 4.15). The amplitude and phase profiles show a clear modulation connected to the ICRH modulation in discharges like #34050 or the NBI modulation itself. However, this is to be expected, and, as all of the steady-state and perturbed profiles are similar, does not provide a reason for removing any data sets.

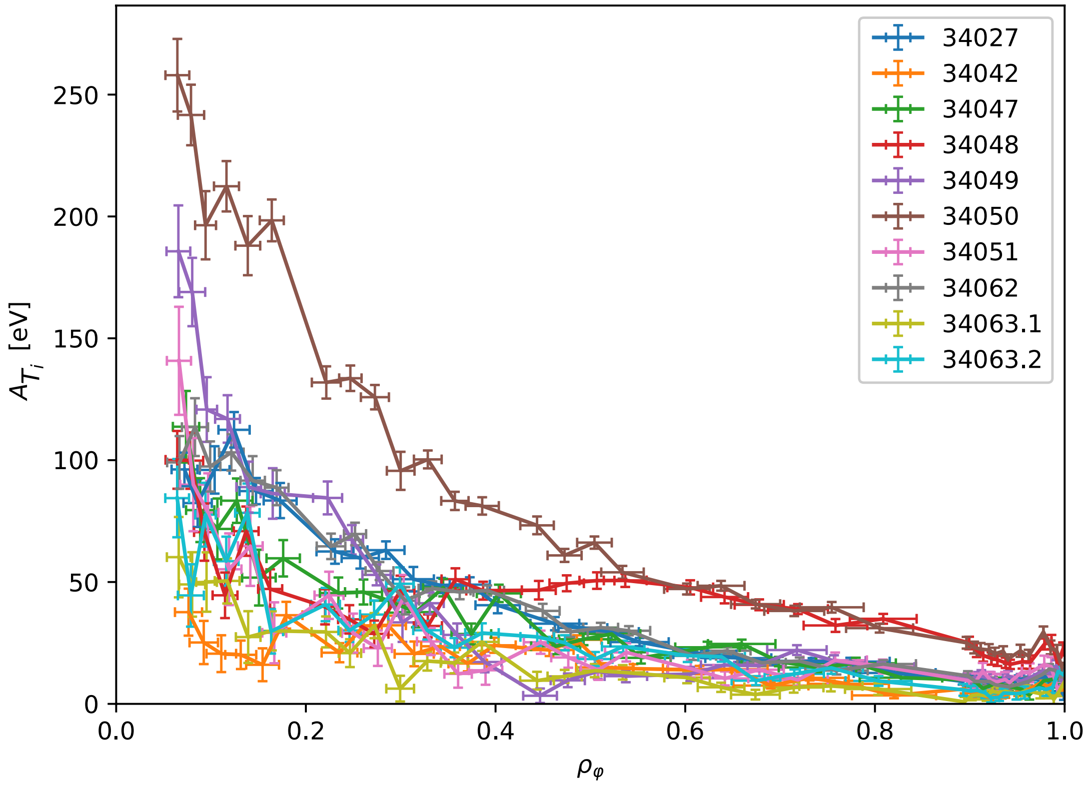

Figure 4.16: Amplitude profiles at f_{mod} for T_i, experimental data from CEZ

Rotation velocity v_{rot}

Comparing the rotation profiles (cf. Figure 4.17), the steady-state profiles of #34048 and #34062 are found to be outliers. Whereas #34048 has slightly too low values, #34062 is clearly above the other profiles.

The aim of the experiment was to produce similar steady-state profiles with deviating amplitude and phase profiles for the rotation. This was successful as depicted in Figure 4.18 and 4.19.

The phase profiles show variation, especially #34048 and #34050 covering nearly 200° phase difference at the edges. Within the radial range of interest different phase gradients are observed, which was the aim of the performed experiments. The lower values in #34048 are on account of the higher ECRH power, which is regularly observed to result in lower rotation [43]. This also explains why #34062 has higher rotation, as this is the case without any ECRH.

However, the noise on the data requires one to be critical of how much one can trust the calculated phase profiles and error bars.

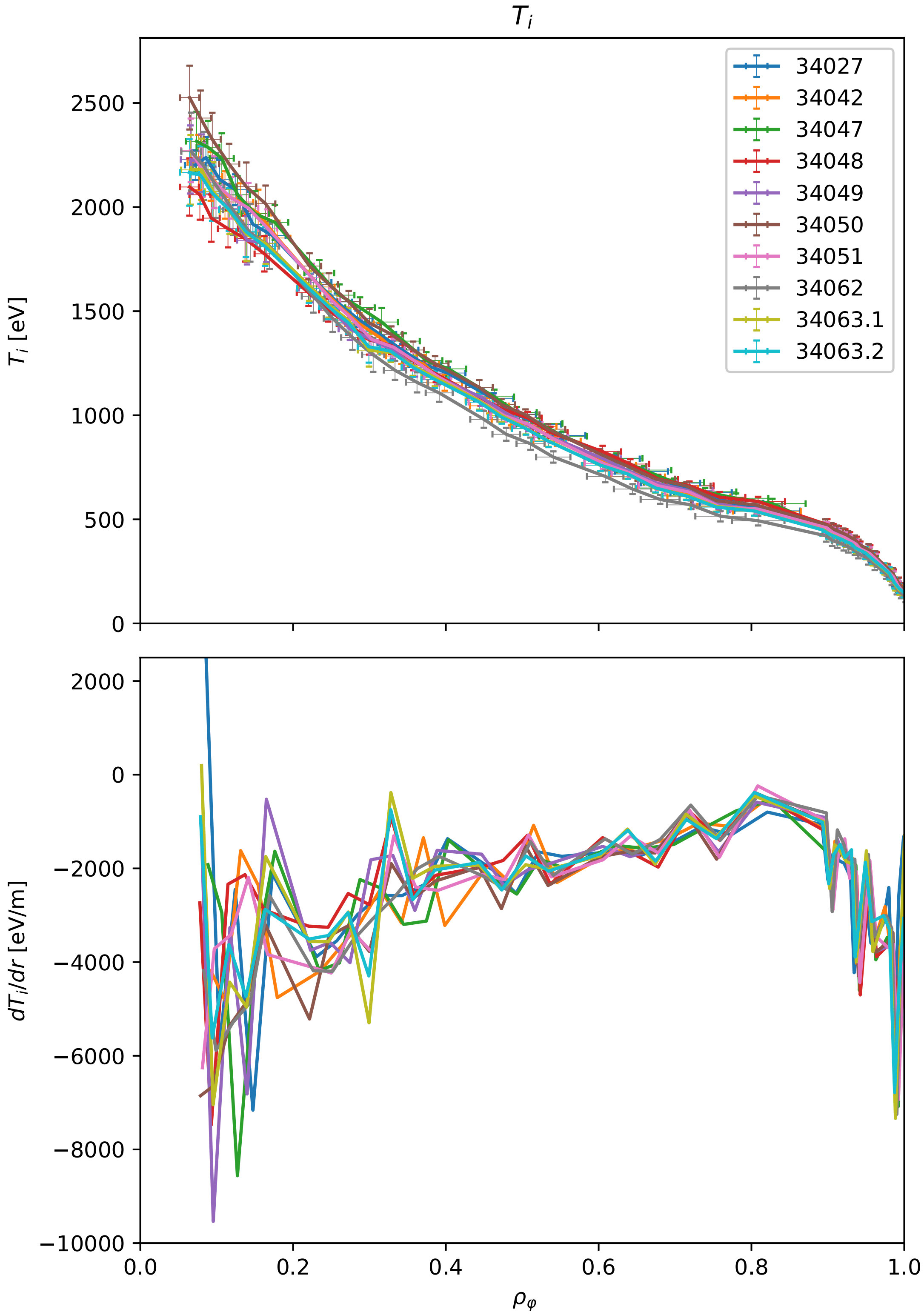

Figure 4.15: Experimental T_i profiles of the considered discharges

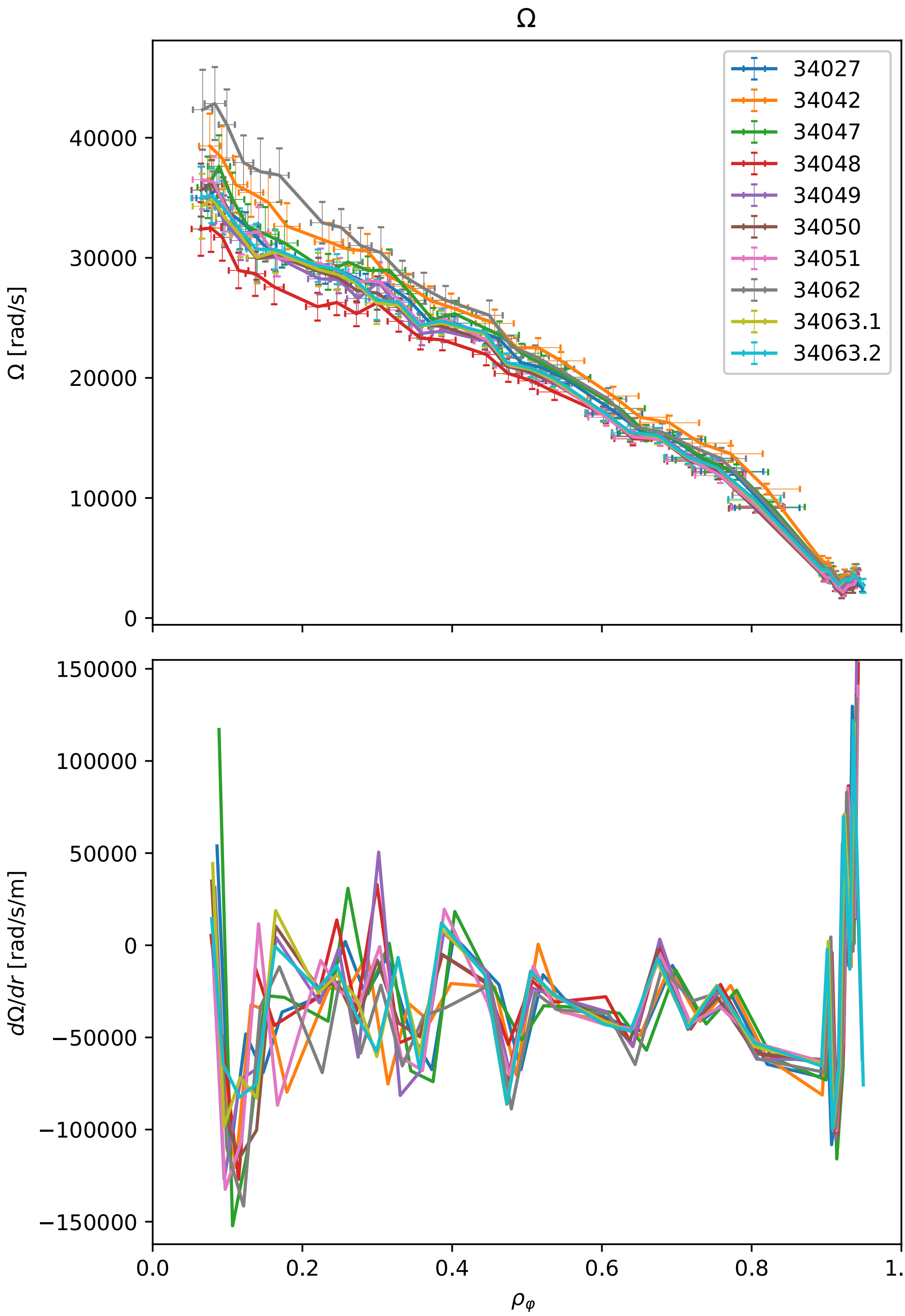

Figure 4.17: Experimental Ω profiles of the considered discharges

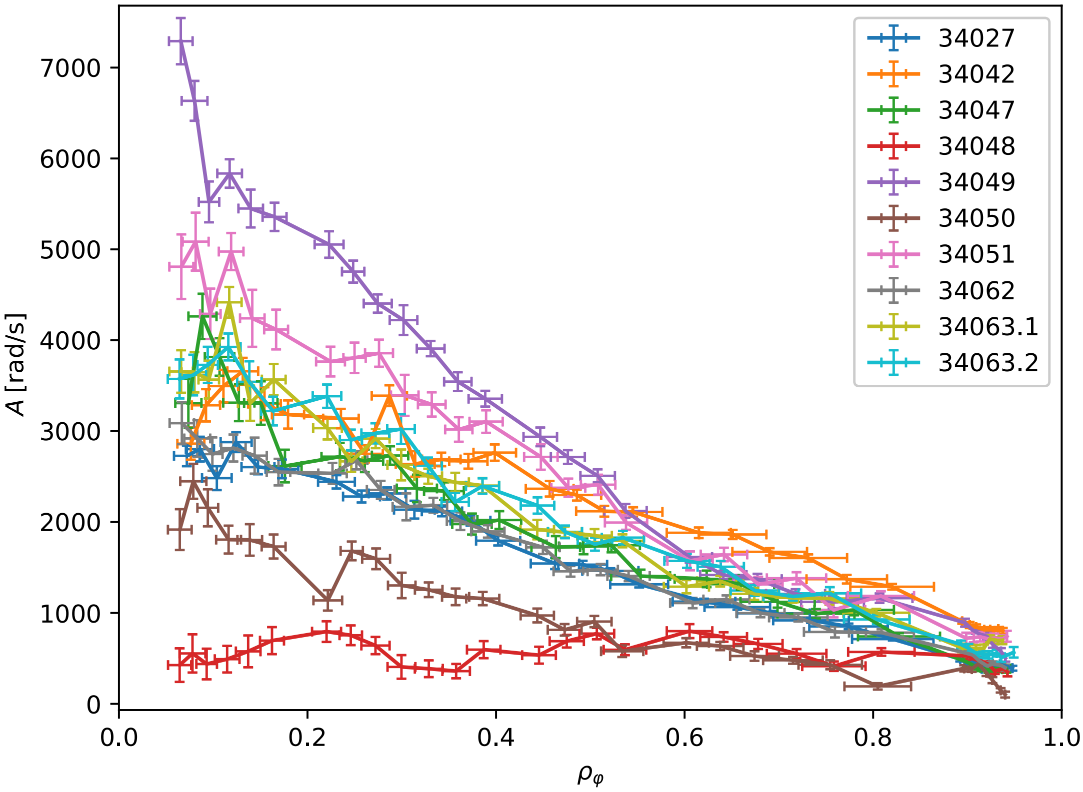

Figure 4.18: Amplitude profile at f_{mod} for Ω, experimental data from CEZ

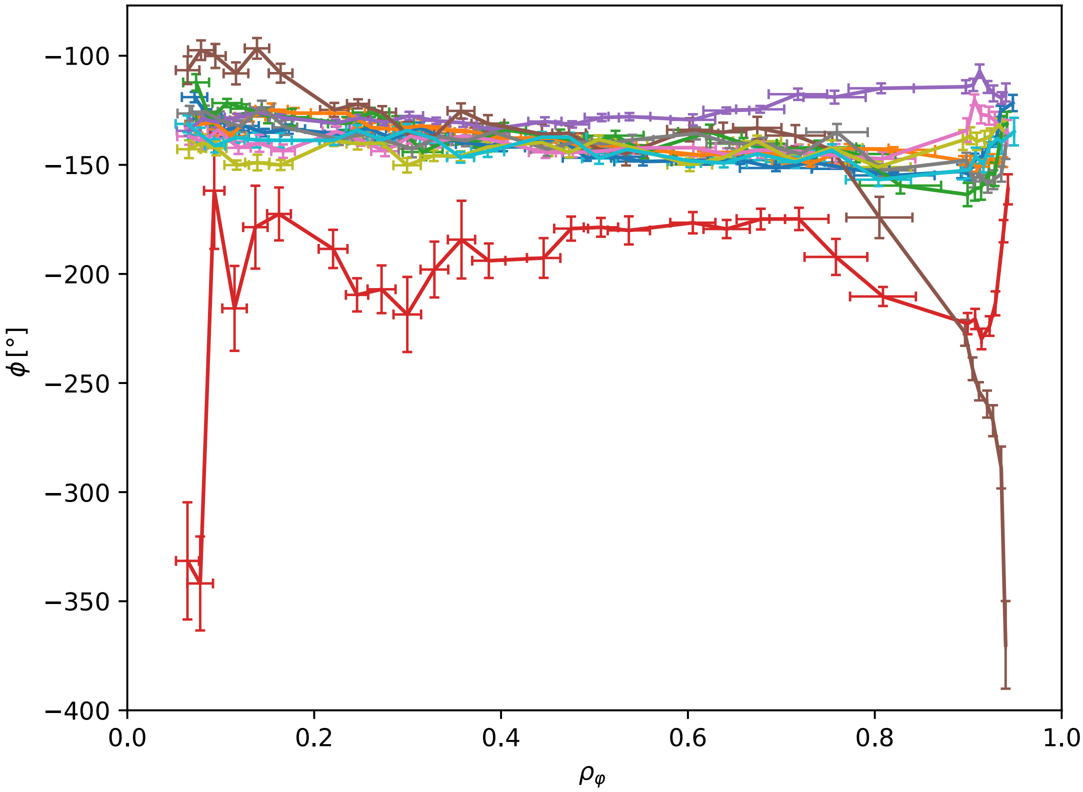

Figure 4.19: Phase profile at f_{mod} for Ω, experimental data from CEZ, legend as in Figure 4.18 above

4.5 Selected discharges

After this detailed analysis, three data sets had to be discarded. #34048 and #34049 due to large perturbation of T_e and thus modulation in the density. Furthermore, #34062 with a too low T_e and too high rotation. This is necessary since only plasma with same background profiles can be expected to have the same transport coefficients. Unfortunately, this selection limits the variation in the amplitude and phase profiles.

Finally, the following seven discharges were selected for further analysis: #34027, #34042, #34047, #34050, #34051, #34063.1 and #34063.2.

As proven in this chapter, these discharges have the same background profiles within error bars with different amplitude and phase profiles. To demonstrate the feasibility of extracting momentum transport coefficients, one has to obtain one set of parameters describing the experimental measured rotation. Furthermore, the aim of this work is to prove the robustness of the method, regardless of how the experiments are exactly designed and performed as long as they provide identical background profiles.

Chapter 5

Verification of Numerics

In this chapter the various checks performed on the data and the numerics are documented. This should help to get an intuitive feeling for the dependencies of the relevant quantities governing momentum transport and how the post-processing of the data impacts the results.

5.1 Data fitting and TRANSP

For such an analysis as carried out in this thesis, the way the experimental data is treated before it is passed to the numerics is a relevant step and has to be considered carefully to neither introduce artificial effects nor to neglect substantial pieces.

Evaluation of different fitting methods

Different fitting methods were tested before converging on the fitting concept already explained in Chapter 3.2). In this chapter the different approaches will be compared. TRANSP plays a central role in the flow of data. This is depicted in Figure 3.1. As explained, the time-dependent profiles for n_e, T_e, T_i, and v_{rot} are fitted manually and are crucial. The different fitting approaches differ in their degree of realism and smoothing. The following fitting procedures were studied for these profiles:

- `const`: time-averaged profile
- `fitted`: 2D spline fit with radial and temporal smoothing
- `sfull`: only smoothing over radius, no smoothing in time, considered to be closest to the raw data
- `mod1`: reconstructed signal by using a time-averaged profile, modifying this with a linear drift and superposing a sinusoidal signal, following the experimental amplitude and phase profiles for f_{mod}, using the 1^{st} harmonic
- `mod12`: like `mod1`, superposition of the 1^{st} and 2^{nd} harmonic

For the time traces of Z_{eff}, P_{NBI}, and P_{ECRH}:

- `smoothed`: fit the experimental data (cf. Chapter 3.2)
- `unsmoothed`: raw data, sampled down to reduce time points to a similar grid

With these different fitting methods a grid of TRANSP runs was performed as listed in Appendix A.3. This allows for the study of the influence of the different approaches. The aim is to reduce noise as much as possible without changing the steady-state profiles and the amplitude of the f_{mod} in the Fourier transformation of the different output quantities of TRANSP in particular like the χ_i (`CONDI`), χ_e (`CONDE`), χ_φ (`CHPHI`), and the torque `TQIN`.

Effective charge Z_{eff}, NBI power P_{NBI}, and ECRH power P_{ECRH}

For the time traces of Z_{eff}, P_{NBI}, and P_{ECRH}, especially the TRANSP run 34027A18 and 34027A35 were compared. These runs feature the same background profiles. The only difference is the smoothing on the time traces in these three quantities. It was found that the unsmoothed run exhibits more noise in all considered outputs. Fourier transformations of the conductivities, in particular, showed high-frequency effects. The amplitude for $f_{\text{mod}} = 3$ Hz was identical.

To go into detail, the Fourier transformation for `CONDI` of the unsmoothed computation shows more high-frequency effects up to 75 Hz. Looking at the `CONDI` time trace, a 15 % higher standard deviation was found. Similar behavior was found for `CONDE`, where strong peaks in the Fourier transformation were found for 65 Hz and 130 Hz. These peaks are the result of the ECRH blips performed in this discharge. The TRANSP results for `CHPHI` behave similarly as for the conductivities. Looking at the `TQIN`, the smoothing was successful, the time traces are less noisy.

Very clearly this smoothing increases the quality of the results, leading to less noise in high-frequency ranges which are not supposed to be studied within this thesis.

Electron density n_e

For the electron density, three methods were tested: averaging out of the time dependence (34027A18, `const`), using a 2D spline fit (34027A19, `fitted`), and using nearly raw data (34027A20, `sfull`). The other quantities were kept constant in time.

Considering the `CONDI` signal (cf. Figure 5.1), the `const` and the `fitted` cases were very similar. The averaged profiles were identical. The `sfull` case showed peaks in the Fourier transformation at 75 Hz and 140 Hz range due to ELMs. It is not necessary to preserve this in the data. Looking at `CONDI` itself, the `sfull` calculation was very noisy, `const` and `fitted` showed basically no deviation. The standard deviation in the `CONDI` signal of `sfull` was about five times higher than for `fitted`. Similar results were found for `CONDE`. In the time traces, large peaks were found for `sfull` coming from too sharp temporal changes in the given signal. Such a behavior clearly shows that TRANSP was not able to work correctly with such unsmoothed data. For the smoothed calculations, the absolute amplitude for f_{mod} and its 2$^{\text{nd}}$ harmonic in the conductivities was preserved very well. The `TQIN` signal showed no deviations, neither in the Fourier transformations, nor in the profiles or time traces. So the noise in `TQIN` only depends on the number of particles used in the TRANSP calculation and not on how n_e is fitted.

To sum up, the `const` and `fitted` routines showed no deviation. Both performed reasonably well when it comes to signals with lower frequencies, but they average over high-frequency effects. The `fitted` density performed very similarly to a time-averaged, constant signal. This means that the density profile is stable and one does not expect drifts in the transport over time. Overall, the author decided to use 2D spline fits for further work to be more flexible in the treatment of drifts.

Electron temperature T_e

For the electron temperature, a similar approach was taken, using `const`, `fitted` and `sfull` data.

There it was found that while `const` did not preserve the amplitude for the modulation frequency in the `CONDI` signal, the `fitted` did. Also, looking at the time trace of `CONDI`, the ramp-up within the signal was not preserved in `const`, the noise in `sfull` is significantly higher, the standard deviation about 17% higher. Looking at the `CONDE` signal, the `sfull` was very noisy and showed many peaks in the time trace originating from too fast temporal changes. The corresponding Fourier transformation showed that the amplitude for f_{mod} was in the noise for `sfull` as well as for `fitted`. In contrast, the `const` run showed a peak for the modulation frequency significantly above the noise level, since the the electron heat flux was modulated due to power changes, the electron temperature also should be. Neglecting changes in T_e by using constant temperature profiles lead to artifacts in `CONDE`. As the temperature does not enter into the calculation of `TQIN`, no changes were observed there.

It becomes obvious that neither the `const`, nor the `sfull` can be used for further calculations. `fitted` is a good compromise, including drifts and ramp-ups, averaging over noise.

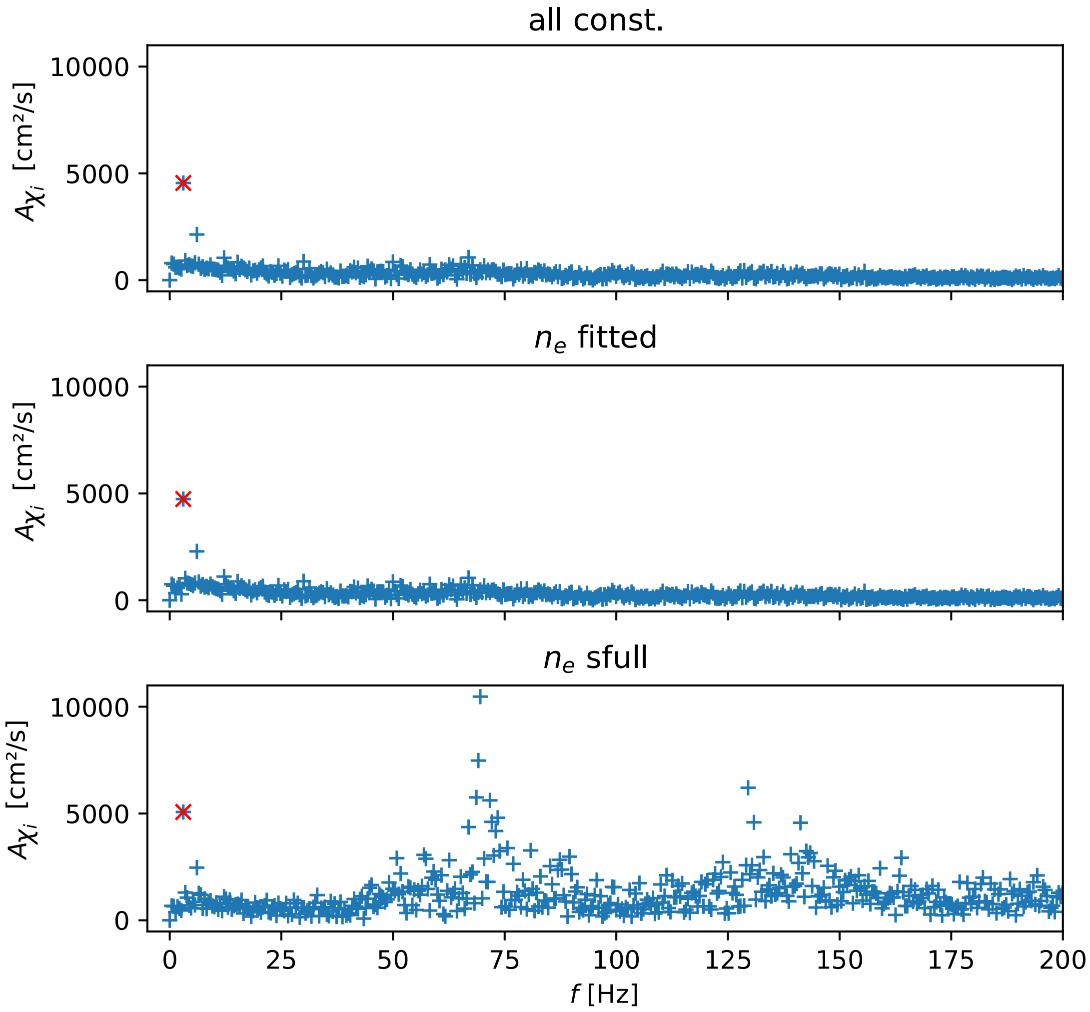

Figure 5.1: Fourier transformations of `CONDI` from different TRANSP runs with variation of the n_e-fitting methods, the amplitude for f_{mod} shown in red.

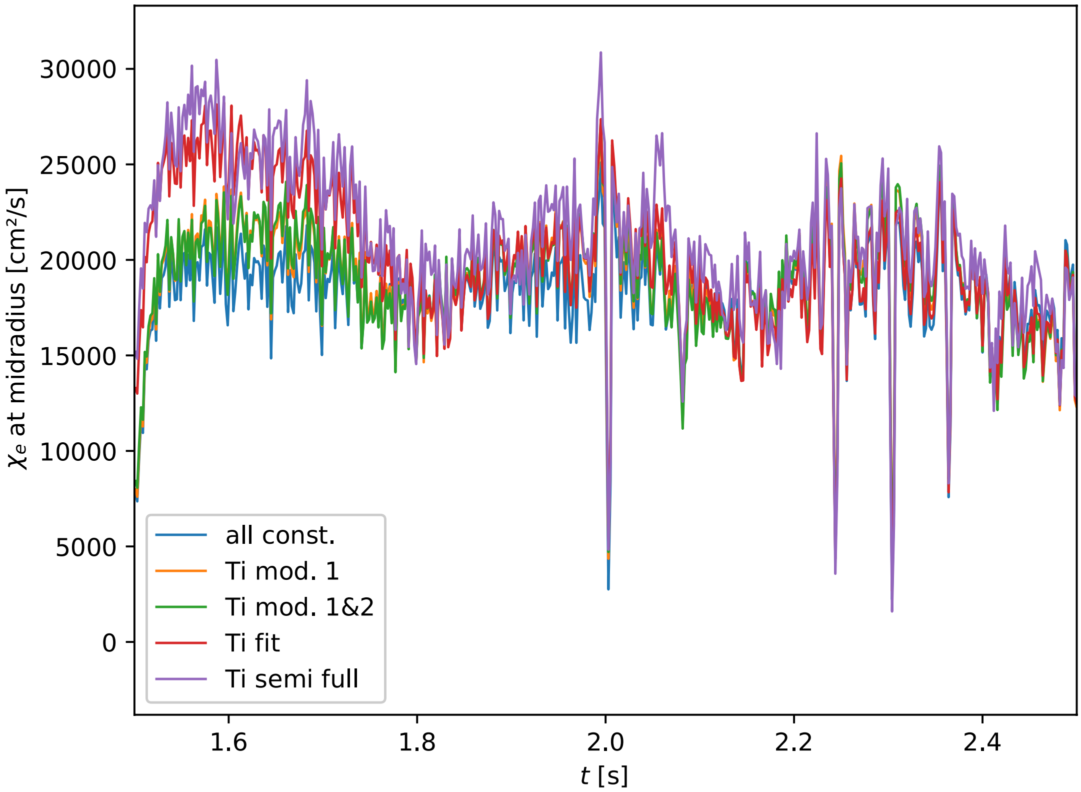

Figure 5.2: Time trace of χ_e (`CONDE`) for different fitting approaches. Only the nearly raw data and the 2D spline fit recover the ramp-down.

Ion temperature T_i

For the ion temperature, five different fitting methods were tested. A `const` (34027A18), a `fitted` (34027A25), a `sfull` (34027A26) and an ansatz following a reconstructed signal based on the Fourier profiles using the 1st harmonic `mod1` (34027A23) and additionally the 2nd `mod12` (34027A24). The other profiles were kept constant.

On the `CONDI` signal, the `const` fitting showed little noise, but did not preserve the amplitude for the modulation frequency. The other approaches did, but varied in the amount of noise. The reconstructed signals `mod1` and `mod12` exhibited very little noise, only for the nearly raw data `sfull`, the Fourier transformation revealed large noise, especially in higher frequency ranges. `CONDE` behaved similarly and showed missing ramp-down effects in `const` and the `mod1` & `mod12`. Here it concerns a time range which is excluded from the final analysis anyhow, but it is wise to find methods able to handle such effects as depicted in Figure 5.2. No effects while varying the fitting methods for T_i were observed on `TQIN` and `CHPHI` as expected. For the effective Prandtl number, especially the `sfull` data was very noisy.

To sum up, the `const` and the `mod` approaches do not recover the data sufficiently. The first one fails on the Fourier amplitude, the second one on the drifts. The `sfull` is very noisy. Again, the 2D spline fit seems to be a good compromise, recovering all of the important quantities of the raw data.

Rotation velocity v_{rot}

Here, similar approaches as for the T_i were made. The rotation is a very important quantity since the routines optimizing the transport parameters in ASTRA compare the simulated data to the fitted data.

As expected, the diffusivities χ_i (`CONDI`) and χ_e (`CONDE`) were not affected by these different approaches. Differences were observed in χ_φ (`CHPHI`), which is an effective momentum diffusivity, since TRANSP does not consider convective contributions, rather a purely diffusive equation is solved. Here, the `const` had a higher amplitude for $f_{\mathrm{mod}} = 3$ Hz and less high-frequency contributions. The `sfull` and `fitted` calculations exhibited much smaller peaks for the modulation frequency. The high amplitude for the f_{mod} is an artifact which can not be found in the nearly raw data and is not desired since this possibly leads to non-physical, time-changing Prandtl number. Besides that, the nearly raw data `sfull` did reveal more noise. This comparison is depicted in Figure 5.3. For the time trace, the `const` and `mod12` approach have a similar standard deviation, the `fitted` has a standard deviation ca. 25 % higher and for the `sfull` data it is more than twice the value. As only n_e and P_{NBI} affect the calculation for `TQIN`, no differences were found there.

Again, the `fitted` approach is the most reasonable to use. The `const` and `mod` approaches do not only lose information, but even induce artifacts in the data.

Summary

A very important outcome of these calculations was to observe the conductivities χ_i, χ_e, and χ_φ to be time-dependent, which will have impact on the further simulations. This time dependence and the time-averaged radial profile is depicted for χ_i in Figure 5.4. This raises suspicions if the Prandtl number is also time-dependent.

After this detailed analysis it became clear that the raw data can not be used. It is not only too noisy, but the code fails to handle the sharp gradients. While the time-averaged, constant approach works well for the density, it yields misleading results for the other parameters as it neglects relevant pieces of such a modulation experiment. Also the artificially reproduced data based on the Fourier profiles failed, being not able to recover drifts, ramp-ups, and effects with higher frequency sufficiently.

Overall, the 2D spline fitting is the most flexible approach and protects the calculations from unphysical artifacts. Therefore, this approach was chosen to prepare the experimental data.

Data transfer and preservation

An important step of the verification is to prove that the used fitting method preserves the input data, especially the Fourier profiles. Besides that, it is important to check that from a numerical point of view, the data is passed correctly. Within the work of this thesis, three versions of the data have to agree: the experimental data, the fitted input for TRANSP, and the output of TRANSP, used as an input for ASTRA. The comparisons in Figures 5.5, 5.6, 5.7, and 5.8 show the data flow for the TRANSP run 34027A01 with respect to the four relevant quantities.

It shows clearly that all steady-state profiles agree and that the necessary information for the time dependence is preserved. The author would like to draw the attention to Figure 5.8 in which the deviation from the fitted curve to the experimental rotation data is already visible. The simulated rotation data from ASTRA is compared against the experimental rotation data passed from TRANSP. The experimental data given to TRANSP is smoothed. This implies an unavoidable deviation of the optimized simulation results from the experimental data.

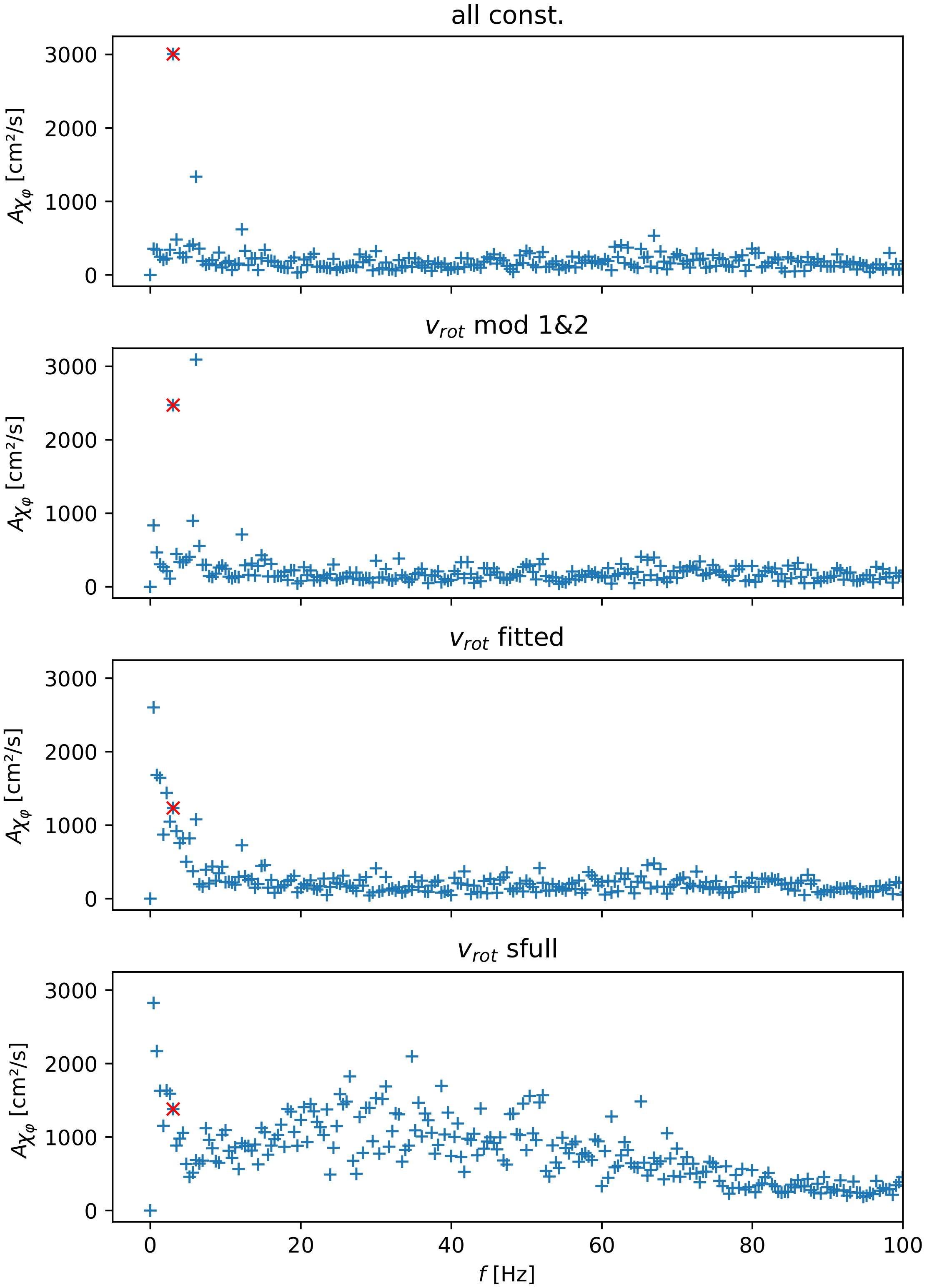

Figure 5.3: Fourier spectra for χ_φ (`CHPHI`) for different fitting approaches. The 2D spline approach recovers the nearly raw data better, the amplitude for f_{mod} shown in red.

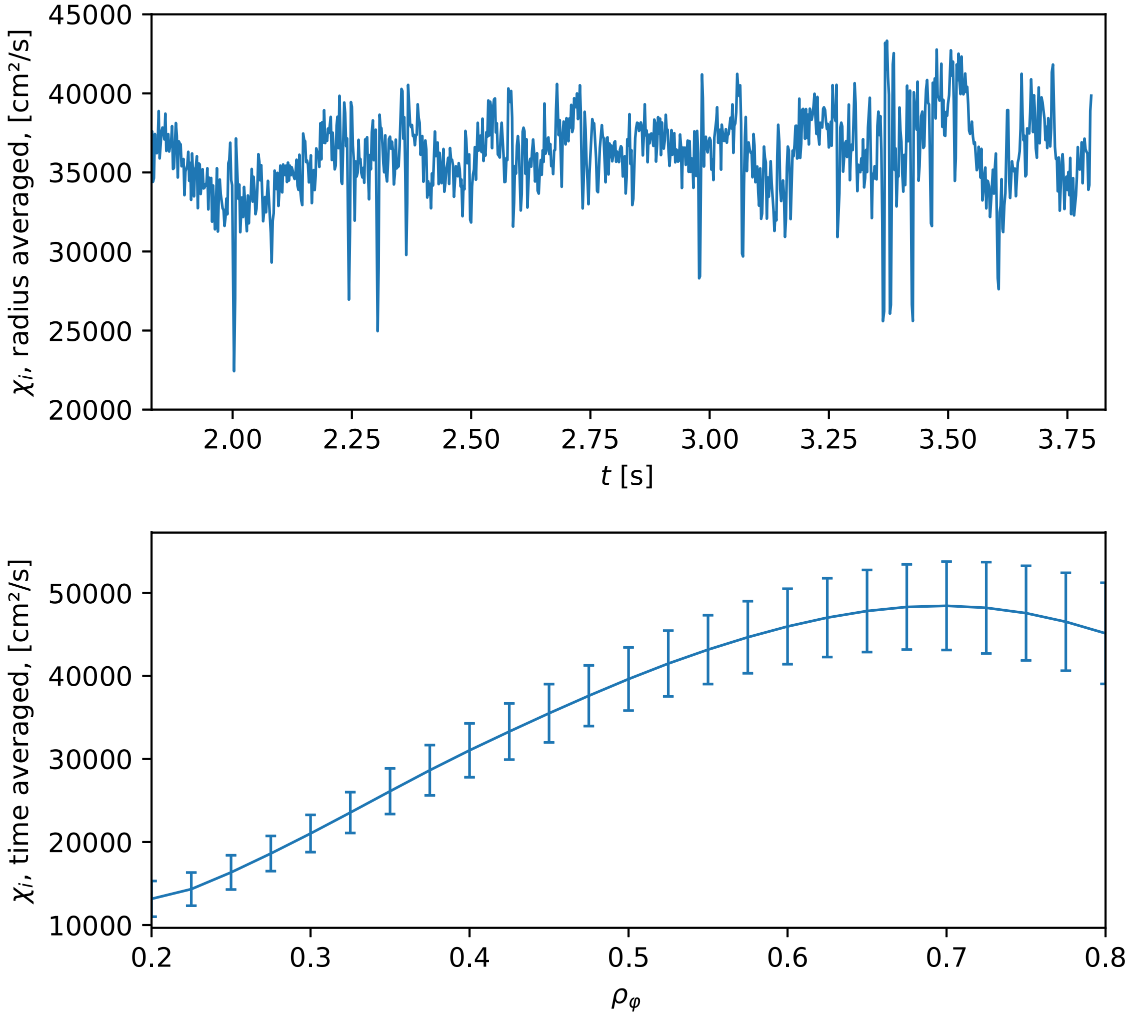

Figure 5.4: Ion heat conductivity from 34027A32, all quantities fitted

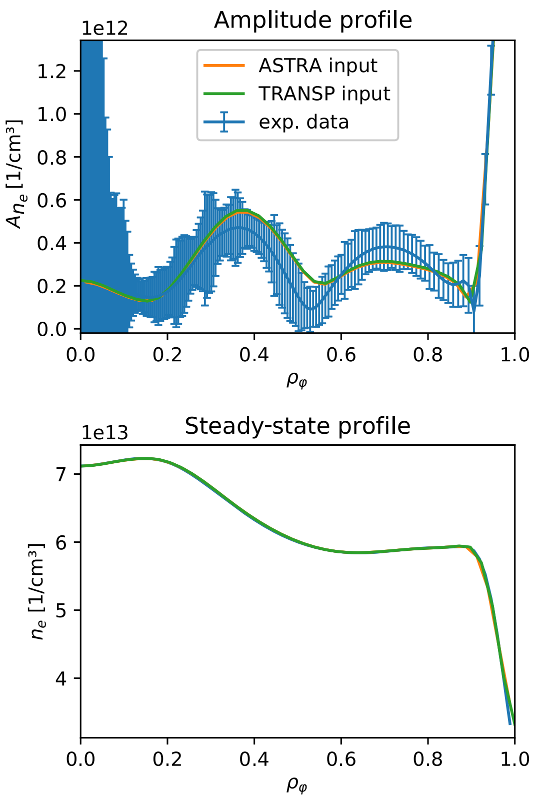

Amplitude profile

Phase profile

Steady-state profile

Timetrace at midradius

Figure 5.5: Flow of data for n_e, 34027A01, agreement between TRANSP input and ASTRA input, the effect of smoothing is visible for the Fourier profile. This is not crucial since the modulation in the density is very small (compare scaling for amplitude and steady state) and has small influence.

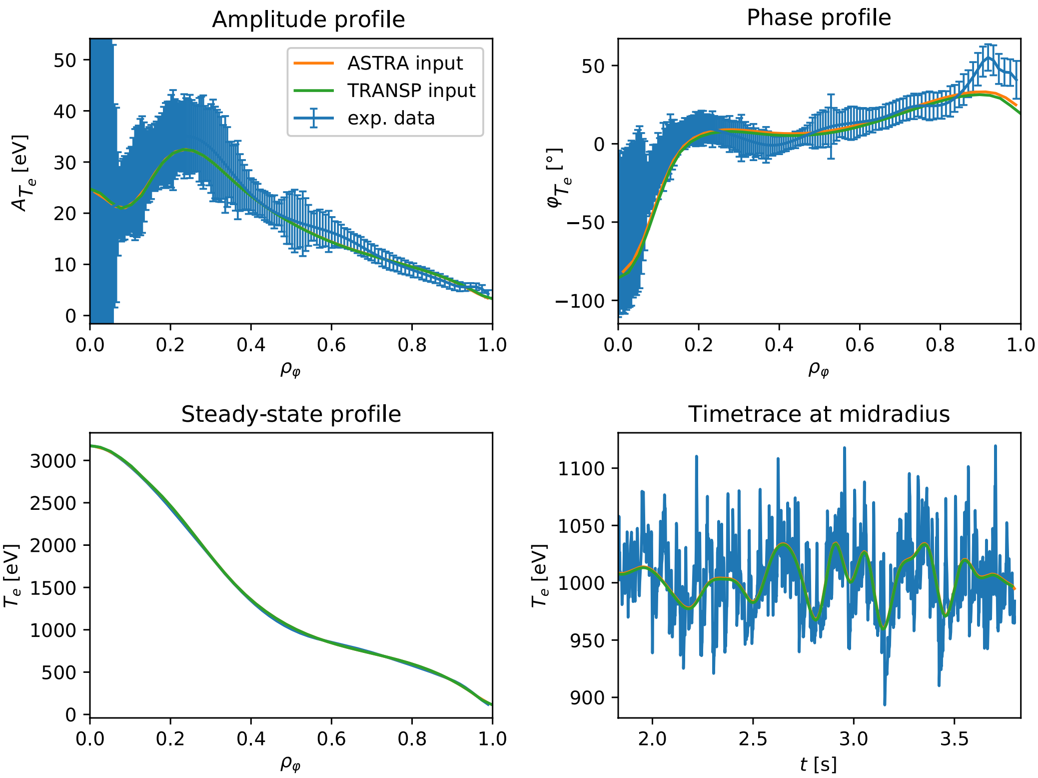

Amplitude profile

Phase profile

Steady-state profile

Timetrace at midradius

Figure 5.6: Flow of data for T_e, 34027A01, agreement between TRANSP input and ASTRA input, the effect of smoothing is visible for the Fourier profiles, but within error bars.

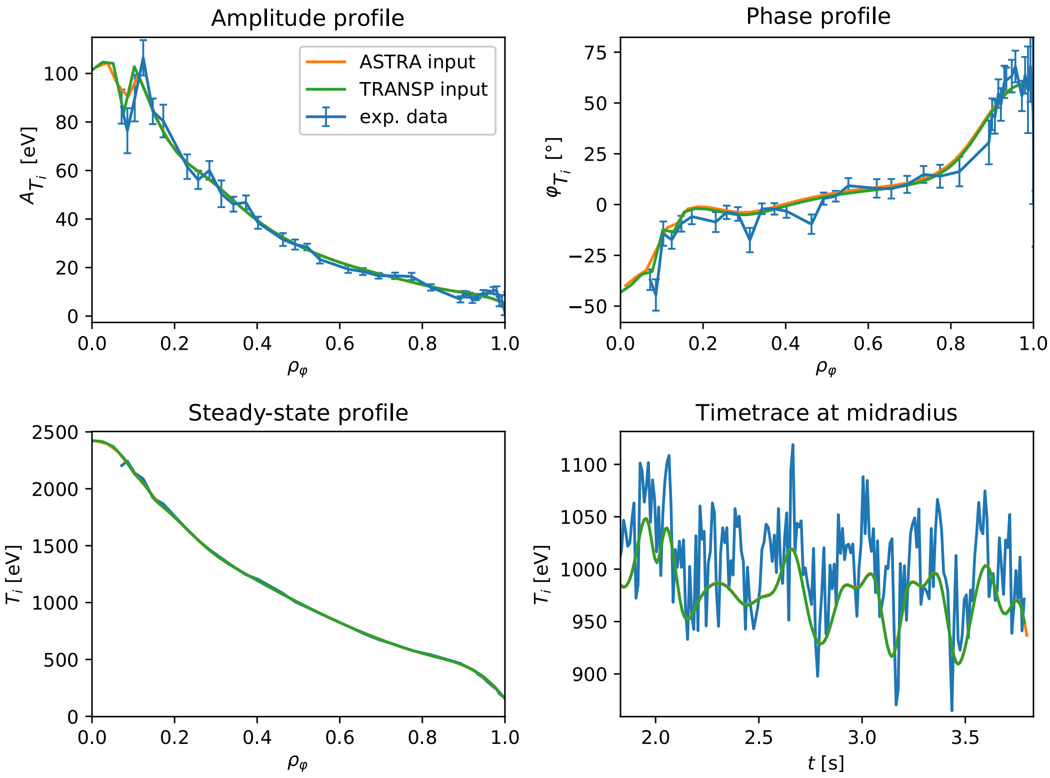

Figure 5.7: Flow of data for T_i, 34027A01, agreement between TRANSP input and ASTRA input, the effect of smoothing is visible for the phase profile but necessary to avoid noise.

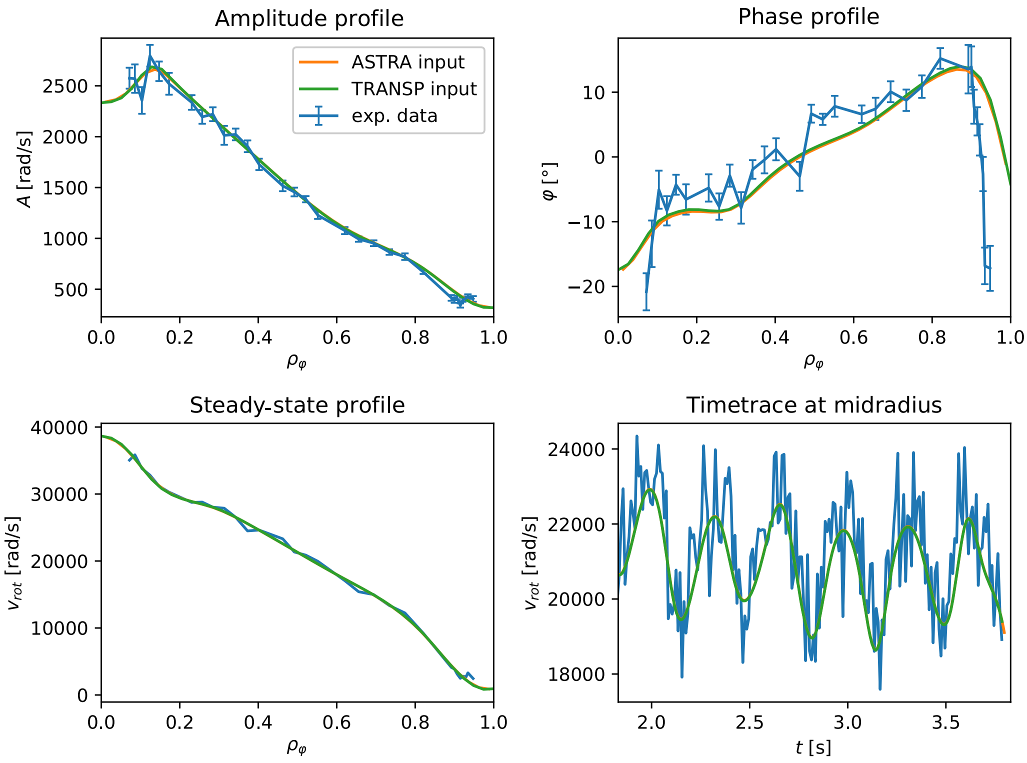

Figure 5.8: Flow of data for v_{rot}, 34027A01, agreement between TRANSP input and ASTRA input, the effect of smoothing is visible for the phase profile.

5.2 ASTRA

The detailed comparison in the last section showed that one can rely on ASTRA using correct and reasonably fitted input data for its simulation. In this section further comparison in calculations as well as a number of different test runs are performed in order to check and understand the basic behavior of the implemented model.

Countercheck the ion heat diffusivity χ_i

In the calculations performed for this thesis, TRANSP was used to calculate the influence of the NBI torque on the plasma. Besides that, TRANSP calculates the diffusivity χ_i. ASTRA also calculates it such that one can compare the two as a validity check on the calculations between ASTRA and TRANSP.

As can be seen in Figure 5.9, the χ_i from ASTRA and TRANSP do not agree. They deviate from each other by about 15%. Similar non-agreement was also found for χ_e. The radial profiles in Figure 5.10 show that the deviation increases with the radial position. This suggests a deviation in the metrics causing the difference to increase with the contained plasma volume.

After a detailed comparison of various parameters and data in fact a difference in the metric definition was found. In TRANSP the heat transport equation is given by

$$Q_i = n_i \frac{\partial T_i}{\partial \rho} S \langle \nabla \rho \rangle \chi_{i,\mathrm{T}}, \tag{5.1}$$

while in ASTRA it is defined as

$$Q_i = n_i \frac{\partial T_i}{\partial \rho} \frac{\partial Vol}{\partial \rho} \langle (\nabla \rho)^2 \rangle \chi_{i,\mathrm{A}}. \tag{5.2}$$

Combining the latter two equations, one finds

$$S \langle \nabla \rho \rangle \chi_{i,\mathrm{T}} = \frac{\partial Vol}{\partial \rho} \langle (\nabla \rho)^2 \rangle \chi_{i,\mathrm{A}} \tag{5.3}$$

with

$$\frac{\partial Vol}{\partial \rho} = \frac{S}{\langle \nabla \rho \rangle} \tag{5.4}$$

in ASTRA. Inserting Equation 5.4 in Equation 5.3 yields

$$S \langle \nabla \rho \rangle \chi_{i,\mathrm{T}} = \frac{S}{\langle \nabla \rho \rangle} \langle (\nabla \rho)^2 \rangle \chi_{i,\mathrm{A}} \tag{5.5}$$

and finally to a difference between the χ_i from ASTRA and TRANSP of

$$\chi_{i,\mathrm{T}} = \chi_{i,\mathrm{A}} \cdot \frac{\langle (\nabla \rho)^2 \rangle}{\langle \nabla \rho \rangle \langle \nabla \rho \rangle}, \tag{5.6}$$

where $\frac{\langle (\nabla \rho)^2 \rangle}{\langle \nabla \rho \rangle \langle \nabla \rho \rangle} \neq \mathbb{1}$, particularly at the edge. In practice, the heat diffusivity produced by TRANSP can be compared to the one from ASTRA by multiplying `SURF`$\cdot$`GXI`$\cdot \chi_{i,\mathrm{T}}$ (quantities from TRANSP output) and `G11`/`ROC` $\cdot \chi_{i,\mathrm{A}}$ (ASTRA variable names). This is shown in Figures 5.11 and 5.12.

There, `SURF` $= S = \langle \nabla \rho \rangle \cdot \frac{\partial Vol}{\partial \rho}$ is the flux surface area in cm^2 (has to be converted to m^2), `GXI` $= \langle \nabla \rho \rangle$ in cm^{-1} normalized to ρ, `G11` $= \langle (\nabla \rho)^2 \rangle \cdot \frac{\partial Vol}{\partial \rho}$ in m^2, and `ROC` $= \rho$ the toroidal minor radius at the last closed flux surface in m. These multiplications correspond to the factor

$$\frac{\langle (\nabla \rho)^2 \rangle}{\langle \nabla \rho \rangle \langle \nabla \rho \rangle} = \langle (\nabla \rho)^2 \rangle \frac{\partial Vol}{\partial \rho} \cdot \frac{\partial \rho}{\partial Vol} \frac{1}{\langle \nabla \rho \rangle} \cdot \frac{1}{\langle \nabla \rho \rangle \cdot \rho} = \mathtt{G11} \cdot \frac{1}{\mathtt{SURF}} \cdot \frac{1}{\mathtt{GXI}} \cdot \frac{1}{\mathtt{ROC}}. \tag{5.7}$$

This deviation in definitions should be noted by anyone making comparisons between the two codes. Within the work for this thesis, the diffusivities were calculated using the ASTRA definition of χ_i.

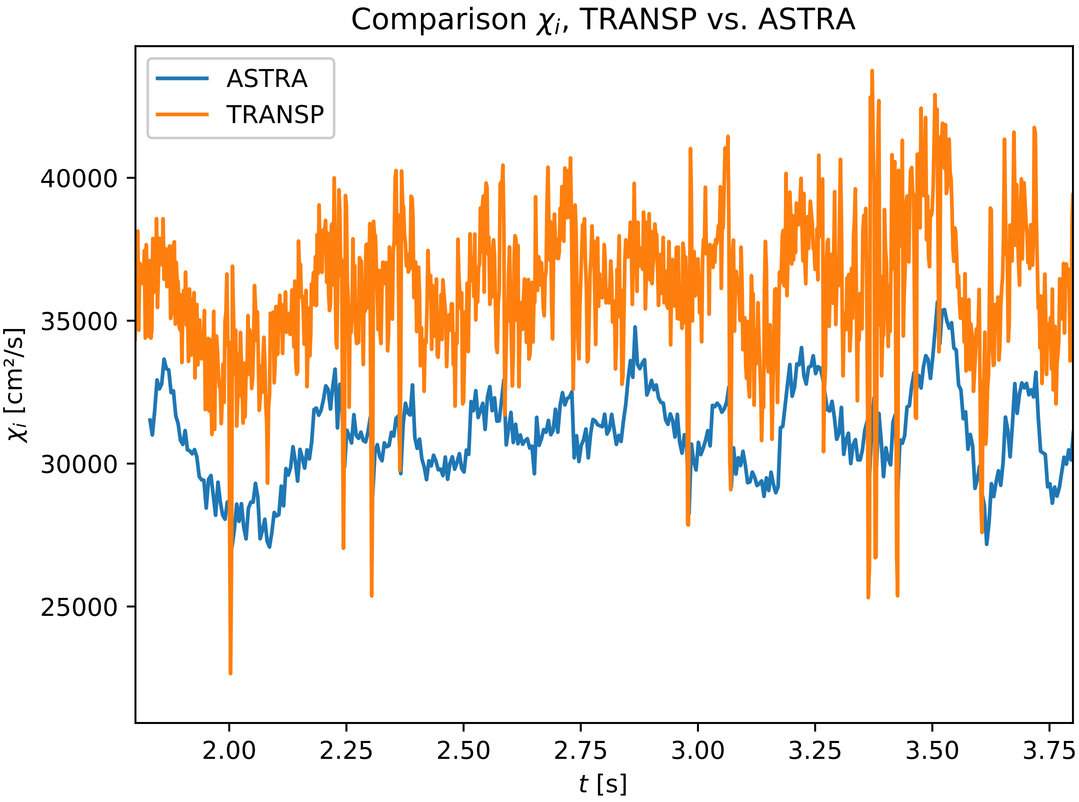

Figure 5.9: Comparison of χ_i from ASTRA and TRANSP, radius-averaged, #34027

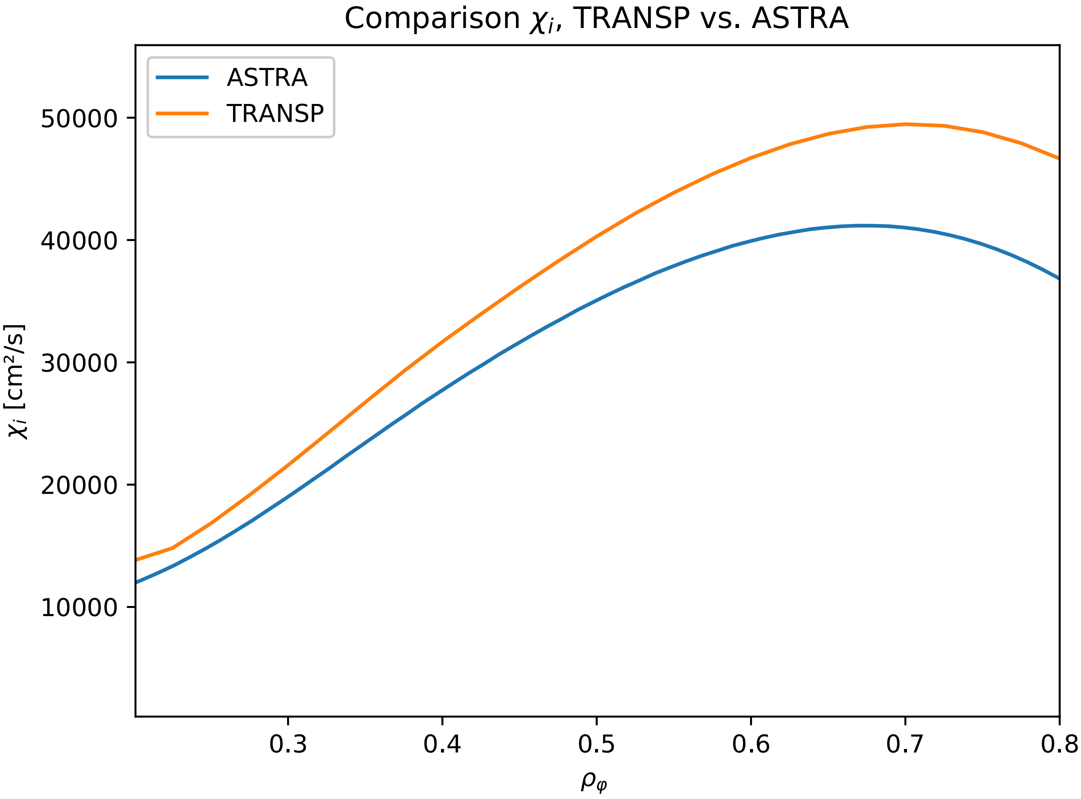

Figure 5.10: Comparison of χ_i from ASTRA and TRANSP, time-averaged profile, #34027

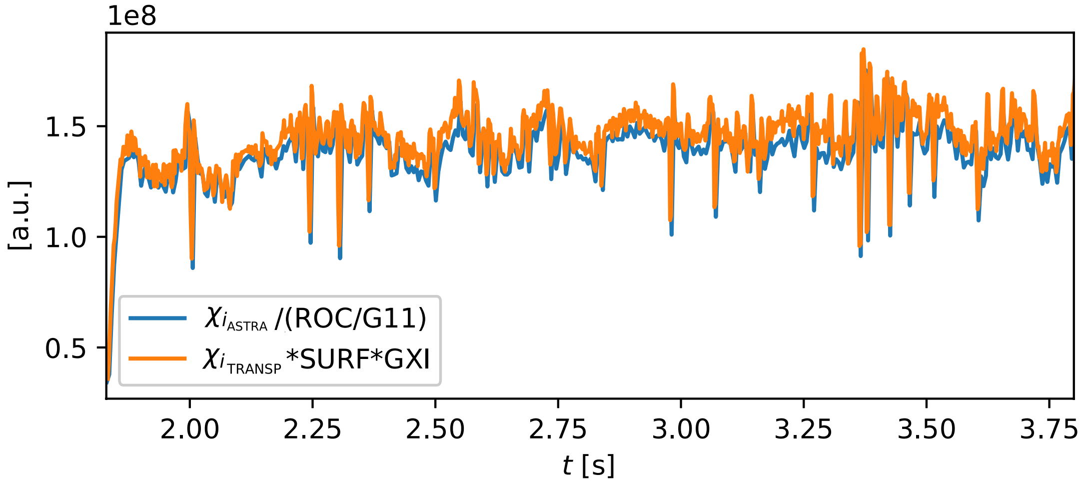

Figure 5.11: Comparison of the χ_i from TRANSP and ASTRA after multiplication by metric factor, radius-averaged, #34027

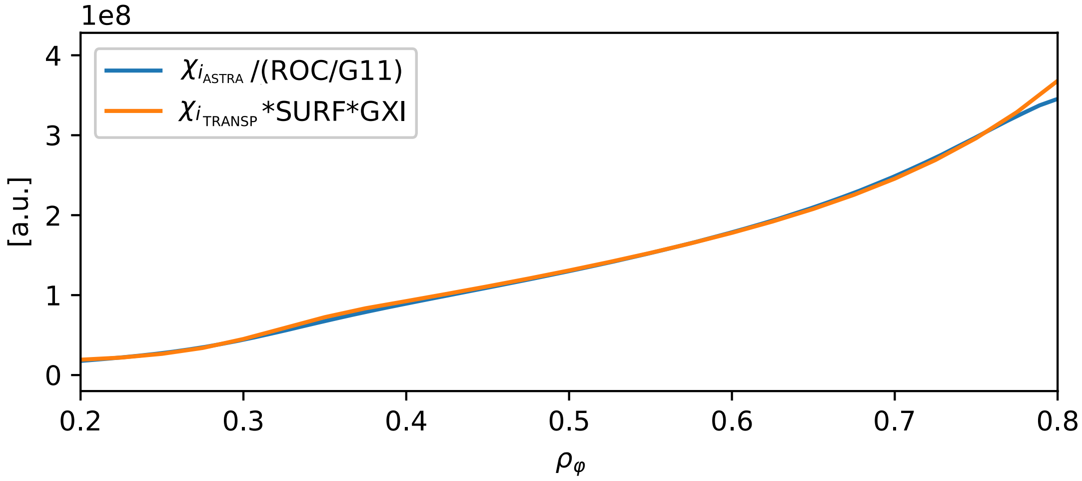

Figure 5.12: Comparison of the χ_i from TRANSP and ASTRA after multiplication by metric factor, time-averaged profile, #34027

Numerical experiments

In this section various numerical experiments were performed to gain intuition for the behavior of the different transport quantities.

Influence of the momentum diffusivity $\chi_{\|}$

First, the momentum diffusivity is set to a constant and scanned in magnitude. This is combined with zero inward pinch and residual stress. Within ASTRA, even for zero pinch, the convection is not entirely zero due to small geometric contributions.

A more realistic approach with a radially linear increasing diffusivity is shown in Figure 5.13. One observes the parallel velocity to increase with a lower momentum diffusivity, as expected since a lower diffusivity in Equation 2.2 is balanced with a larger rotation gradient, if convection is negligible and the residual stress is zero. With a lower parallel momentum diffusivity, the momentum pinch stays lower, since it scales with the diffusivity (cf. `CNPAR` $\sim$ `XUPAR` in Table A.4). The lower the momentum diffusivity, the steeper the phase profile, since it takes longer until the perturbation gets transported. Similarly the amplitude profile is higher for a lower momentum diffusivity since a higher diffusivity damps the perturbation more strongly, resulting in lower amplitudes.

Influence of the pinch velocity v_{Pinch}

As a next step, the $\chi_{\|}$ is coupled to χ_i with a trivial Prandtl number $Pr = 1$. The residual stress is neglected and an artificial pinch velocity is assumed. First, a linear increasing momentum pinch is introduced as one can see in Figure 5.14. With increasing outward pinch, the parallel velocity and the amplitude decreases, since the rotation is convected outwards. In contrast, an inward directed pinch accumulates the rotation leading to a high amplitude and rotation the center. The inward convection ($v_{\mathrm{Pinch}} < 0$) causes a delay in how long it takes a central perturbation to reach the edge, therefore one observes steeper phase profiles. The outward convection ($v_{\mathrm{Pinch}} > 0$) effects the profiles oppositely.

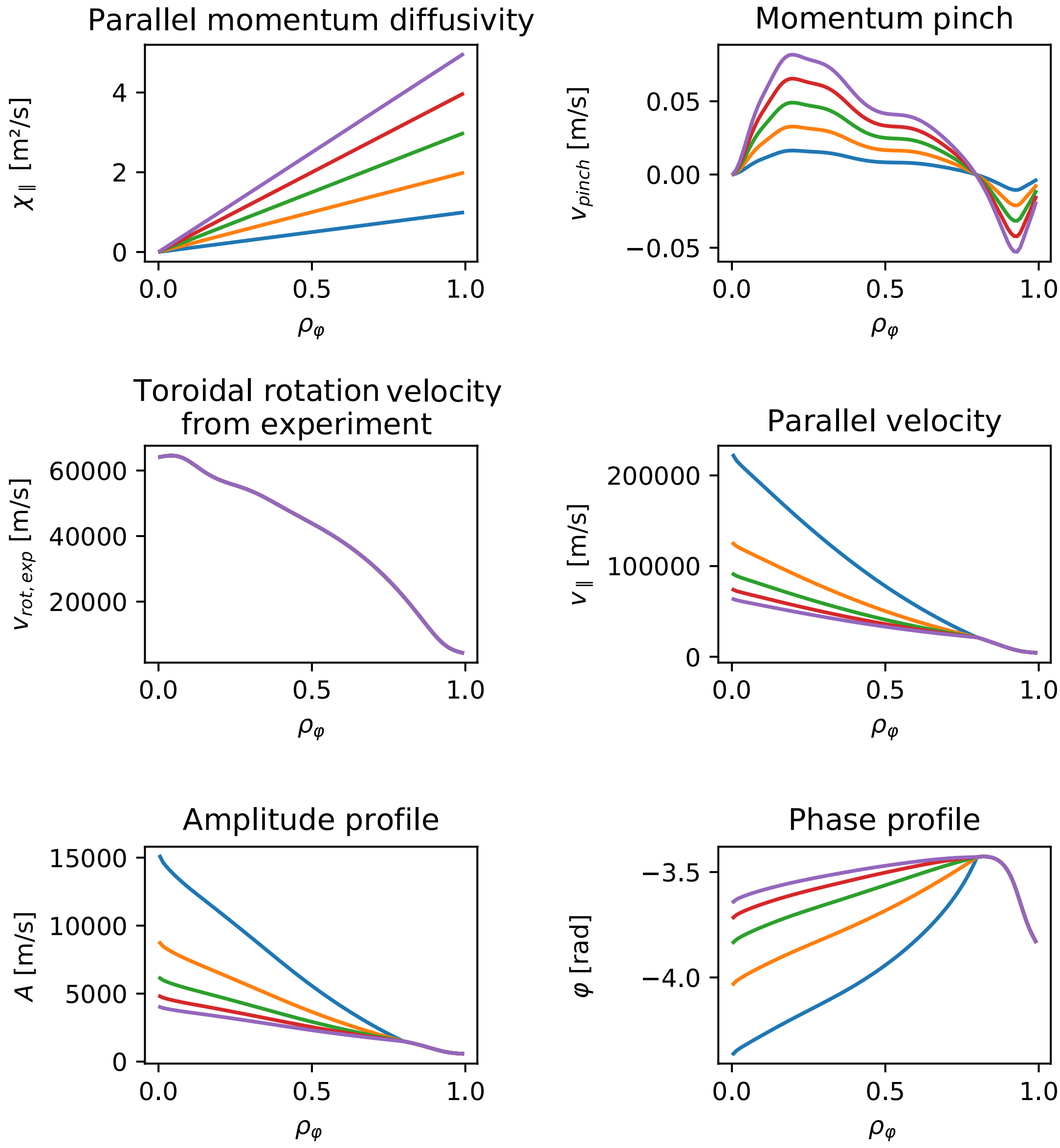

Figure 5.13: Numerical experiment, varying the $\chi_\parallel$

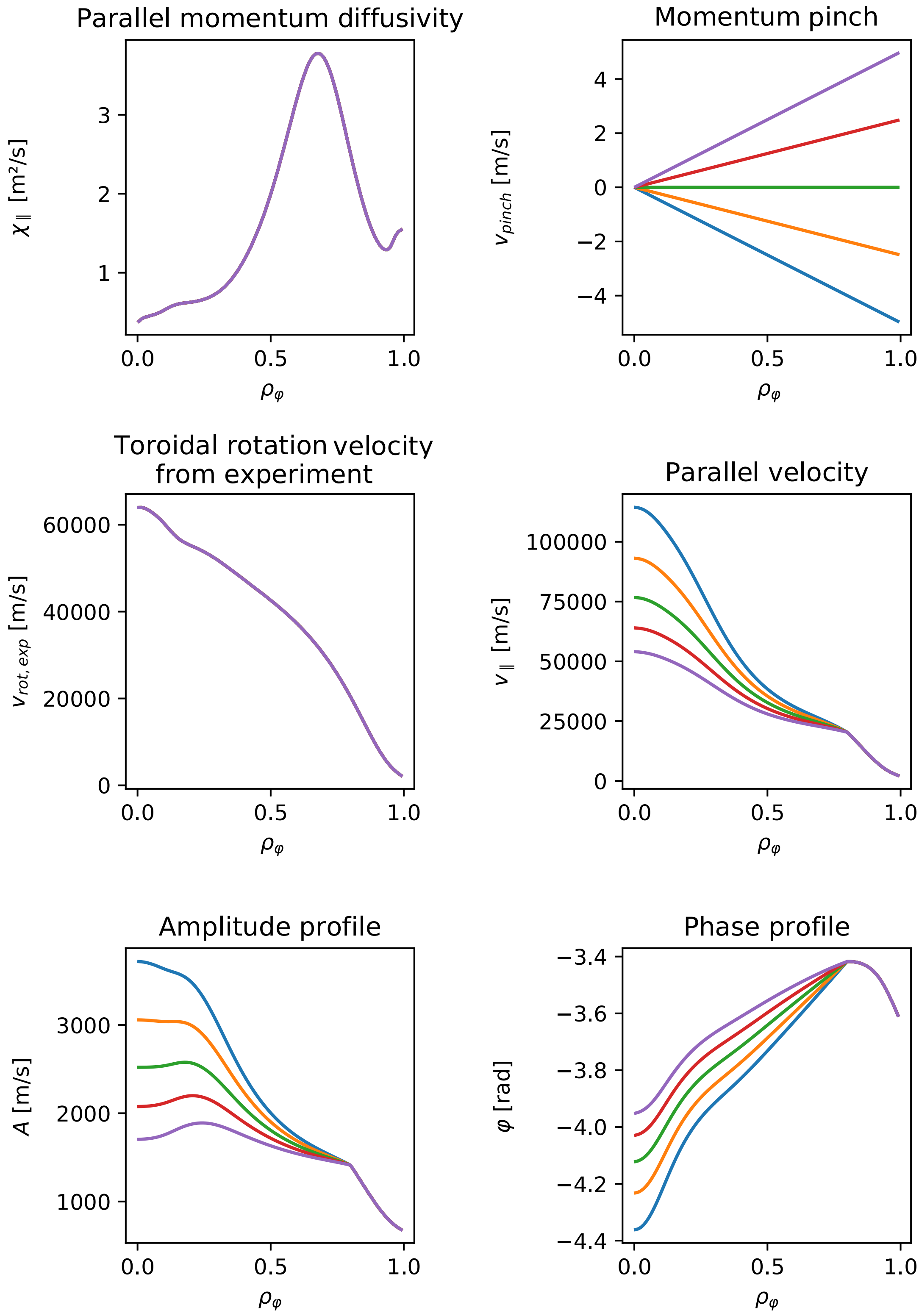

Figure 5.14: Numerical experiment, varying the v_{Pinch}

Influence of torque `TQIN`

To understand the reaction of the simulation to different torques, an artificial torque is imposed. This is done with a simple $Pr = 0.9$, the full pinch model, and no residual stress. The used parameters for the pinch and the Prandtl number are optimization results from an earlier version of the transport model, but do show a representative dynamic of the system. To produce the artificial torque profile, the `TQIN` signal from TRANSP was taken and averaged over time. Then, a NBI modulation is imposed in the form of

$$\frac{A_{max}}{\sqrt{2\pi\sigma^2}} \exp(-\frac{(\rho_\varphi - \mu)^2}{2\sigma^2}) \sin(2\pi t f) \tag{5.8}$$

with $f = 3$ Hz, $\sigma = 0.2$, $A_{max} = 7 * 10^{-9} * Z$, $Z \in [0, 2, 4, 6, 8]$, where $A_{max} = 7 * 10^{-8}$ kg/m/s^2 is the amplitude of the 3 Hz modulation in `TQIN`.

With varying Z and thereby the amplitude of the modulation, one can study different energy depositions. In Figure 5.15, one can see that the blue curve with $Z = 0$ has the lowest amplitude and the flattest phase profile. The purple one for the $Z = 8$ case has a much steeper phase and amplitude profile. This means increasing the size of the perturbation should help to avoid flat phase profiles, which are hard to model. It is observed that the phase profile shows an asymptotic behavior and that still a significant modulation of the rotation takes place even for no modulation of the torque (compare blue curve). This shows that different quantities, being modulated, influence the calculation, e.g. the momentum diffusivity.

The shown reaction of varying the deposited NBI energy can be validated against the experiment when comparing NBI discharges with different acceleration voltages. For example, in modulation experiments with $f_{\mathrm{mod}} = 7$ Hz, the acceleration voltages were varied. In agreement with the numerical experiment, one finds here that the amplitude is lower in discharges with lower energy deposition as depicted in Figure 5.16. One recovers the observation from the numerical experiment that the phase profile varies very little as shown in Figure 5.17.

In the second run of this numerical experiment (cf. Figure 5.18), the central position of the deposited torque was shifted to $\mu = 0.6$ to simulate off-axis beams. This clearly has an impact on the Fourier profiles. The maximum of the amplitude is shifted outwards and is reduced. The phase profiles flatten compared to the one in Figure 5.15. The steady-state profile of the rotation is not affected. Since a flatter phase profile is harder to analyze, off-axis deposition is not helpful for the analysis method used in this thesis. One recovers the observations of the numerical experiment within the experimental data: the amplitude profiles flatten, the phase profile become less steep for the off-axis heating as shown in Figures 5.19 and 5.20.

The simulations with artificial NBI torques appeared to react as expected: a higher torque gives a higher amplitude profile. Shifting the beam position lowers the modulation amplitude in the core. A short validation against experimental data recovers these predictions. This provides reasonable assurance that one is using ASTRA correctly and understanding for its behavior is given.

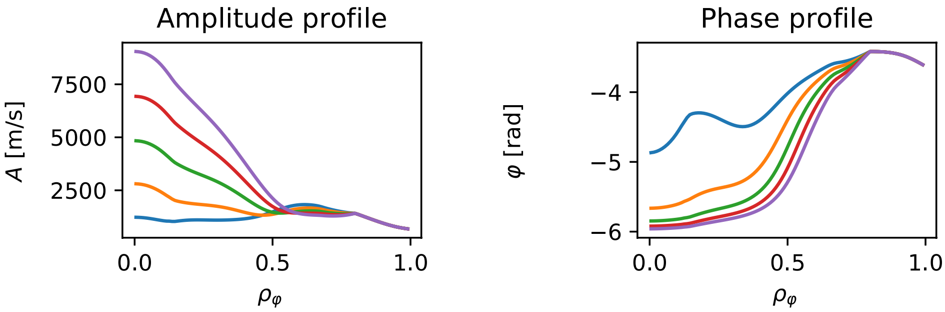

Figure 5.15: Numerical experiment, using an artificial NBI torque, scaling the deposited torque, blue curve corresponds to $Z = 0$ (cf. Equation 5.8), the purple one to $Z = 8$, $\mu = 0.2$

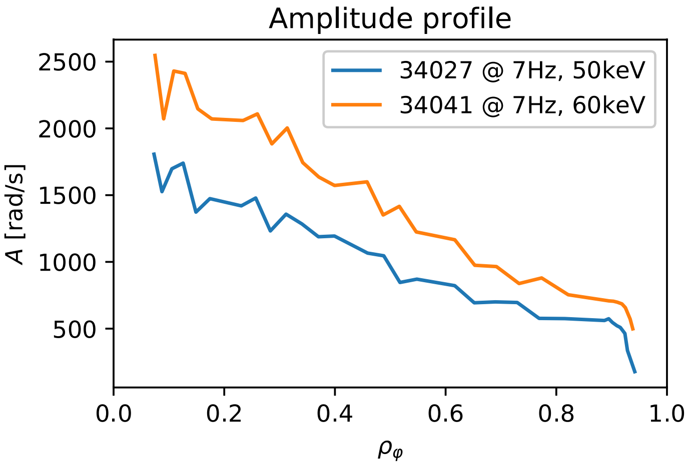

Figure 5.16: Experimental amplitude profiles with different NBI voltages to validate the numerical experiment. One expects the blue curve to be lower.

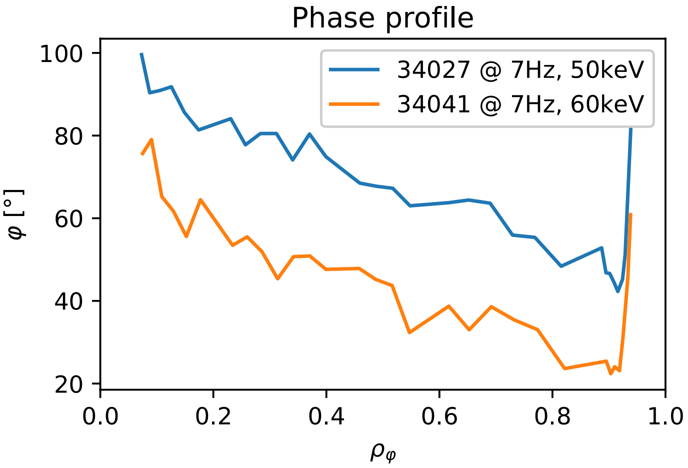

Figure 5.17: Experimental phase profiles with different NBI voltages to validate the numerical experiment. One expects to find similar phase gradients, since the variation of the NBI voltages is rather small.

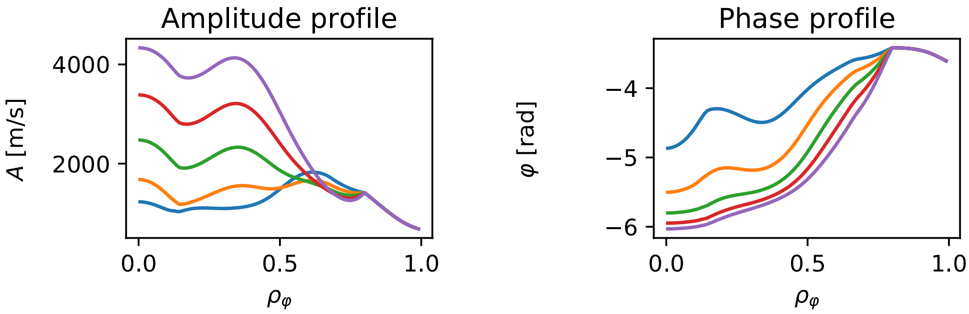

Figure 5.18: Numerical experiment, using an artificial NBI torque, changing the deposition position to $\mu = 0.6$, varying the amplitude of the torque modulation, blue curve corresponds to $Z = 0$ (cf. Equation 5.8), the purple one to $Z = 8$

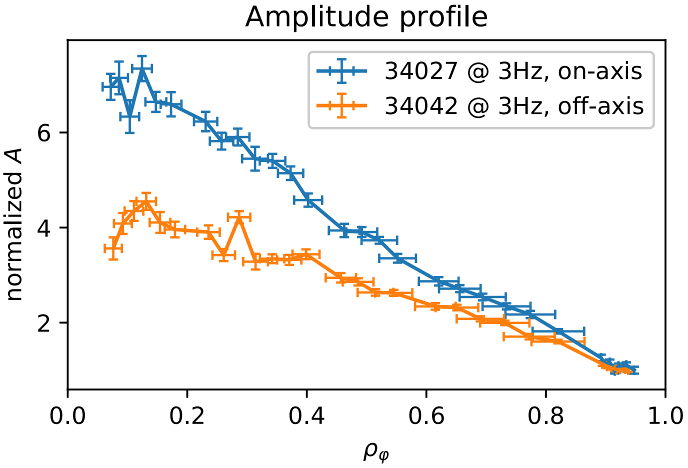

Figure 5.19: Experimental amplitude profiles with different NBI deposition positions to validate the numerical experiment. One expects the blue curve to be higher and steeper. The two curves have been normalized to their edge value to facilitate the comparison.

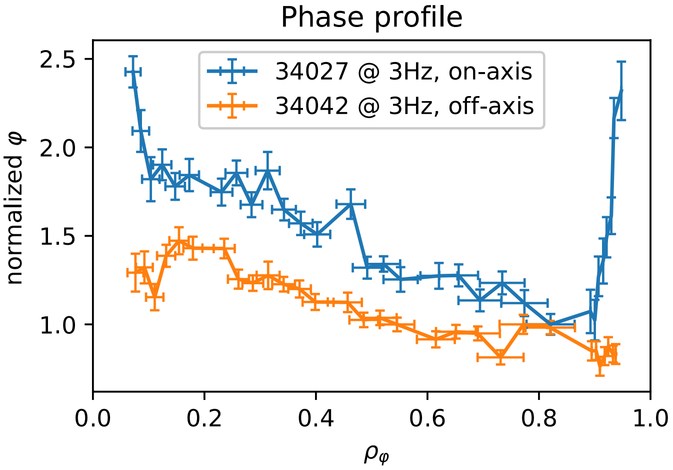

Figure 5.20: Experimental phase profiles with different NBI deposition positions to validate the numerical experiment. One expects the blue curve to be steeper overall. The two curves have been normalized to their edge value to facilitate the comparison.

Influence of the pinch model parameters

To get an impression for the two parameters in the pinch model used, a scan was performed. The $Pr = 0.9$ was fixed, the residual stress was neglected and a different set of parameters was tested for the pinch parameters scaling with the logarithmic density gradient (`CHE1`) and the shear (`CHE2`). This is shown in Figure 5.21. It demonstrates that the parameter `CHE1` determines the behavior of the pinch velocity for the outer radius, `CHE2` is governing until $\rho_\varphi \approx 0.8$. This is mainly a consequence of the different shape of the dimensionless profiles of R/L_{n_e} and s as depicted in Figure 5.22.

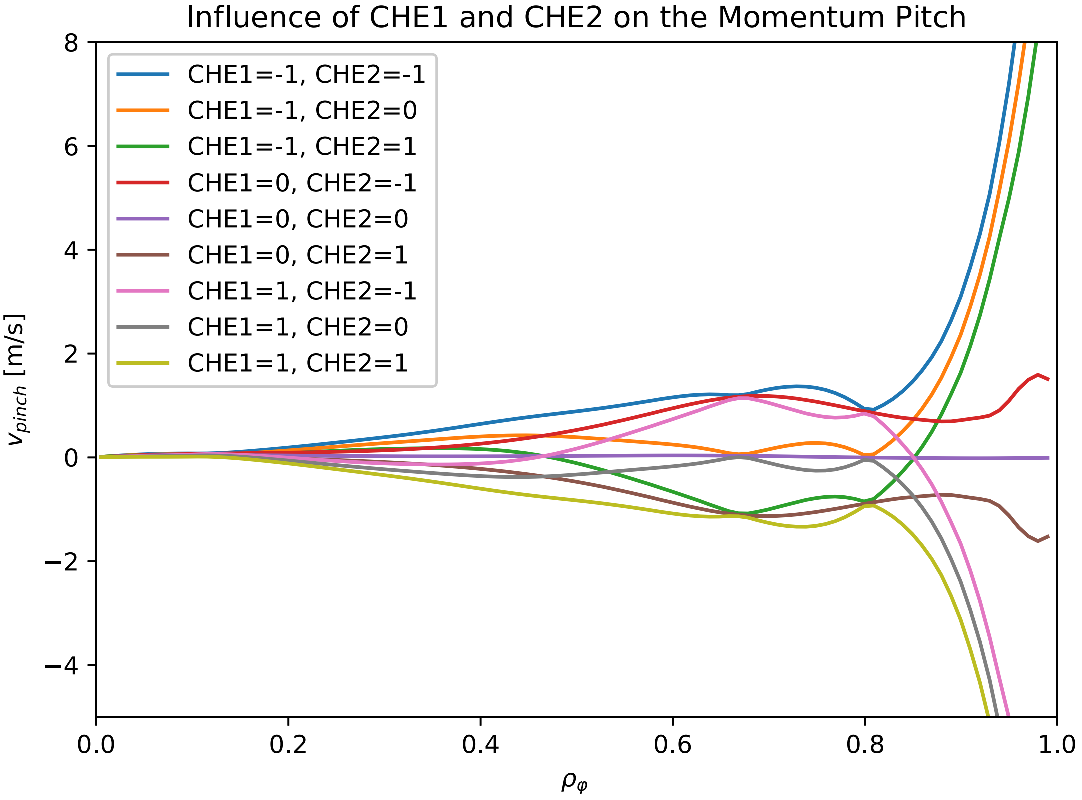

Figure 5.21: Numerical experiment, using different pinch parameter, #34027

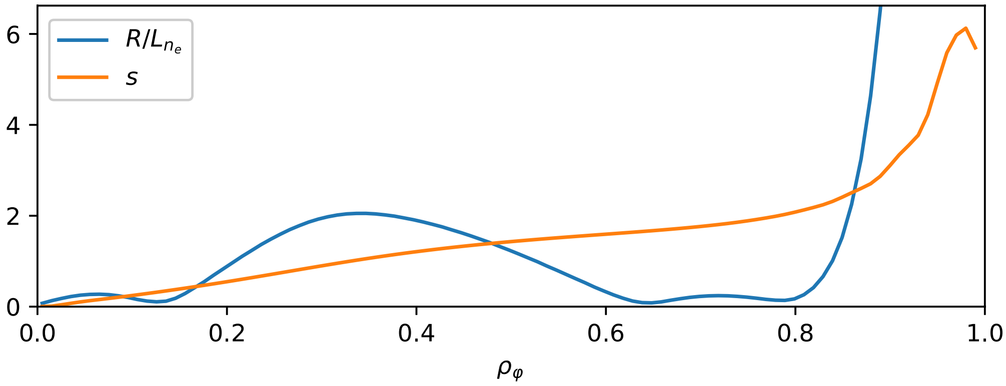

Figure 5.22: The logarithmic density gradient and the shear as used by ASTRA, time-averaged, #34027

Influence of the residual stress

To understand the dynamics of introducing a residual stress, a numerical experiment was carried out. In this, all profiles but the input torque `TQIN` were averaged in time and different magnitudes of residual stress were imposed. As one can clearly see in Figure 5.23, this does not change the amplitude and phase profiles, only the steady-state profile. This observation is of high importance for this thesis, since it justifies first to fit the transport parameters to match the Fourier profiles and afterwards adjusting the steady-state profile with the residual stress.

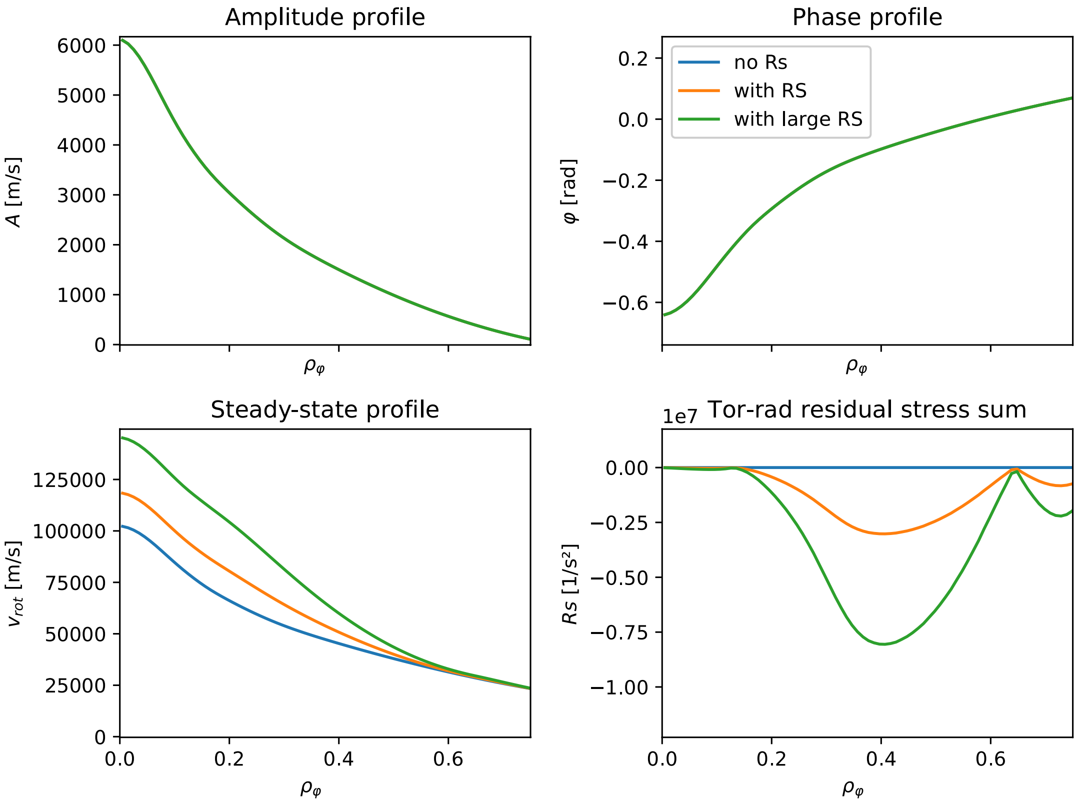

Figure 5.23: Numerical experiment, using different magnitudes of residual stress with constant background profiles, #34027

It is important to realize that in a realistic simulation with time-changing profiles, the residual stress can influence the amplitude and phase profiles if it depends on quantities like n_e or $\chi_{\|}$ that modulate.

Influence of the boundary conditions

The boundary condition for the rotation profiles can also impact the results of the simulation. To demonstrate this, a set of simulations was carried out by fixing the Prandtl number and the pinch velocity, neglecting the residual stress and with a variation of the boundary condition from $\rho_\varphi = 0.7...0.9$. The result is depicted in Figure 5.24.

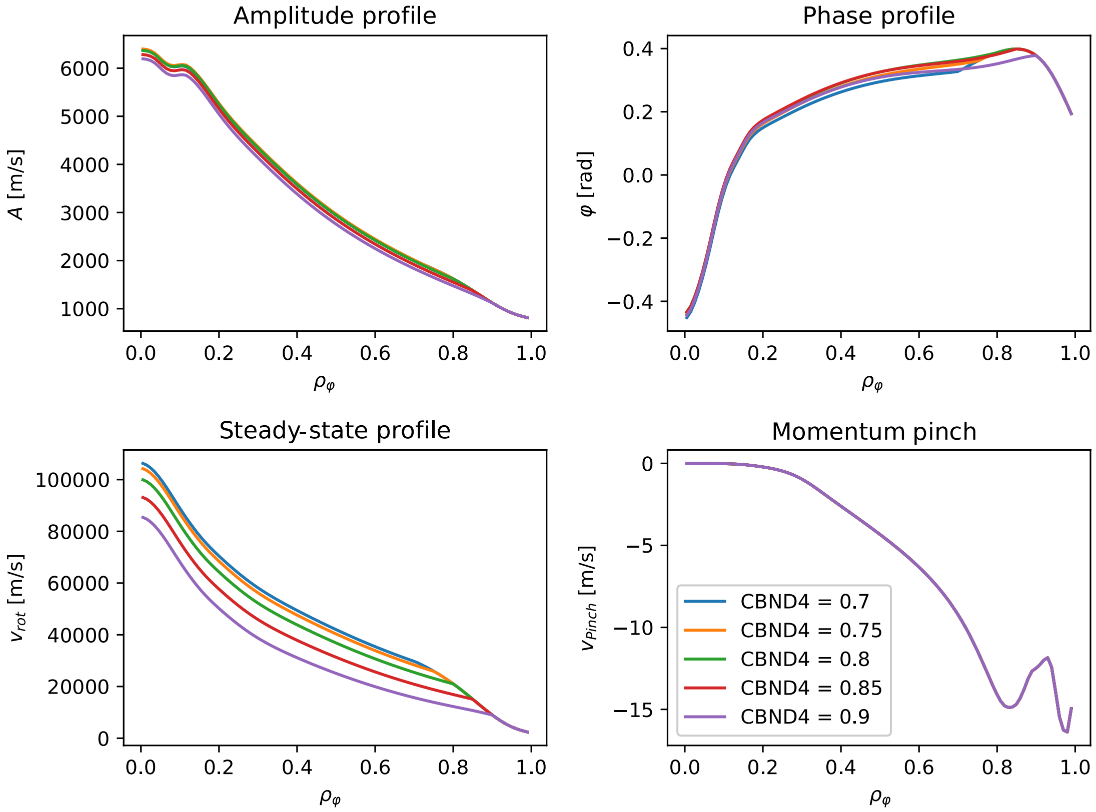

Figure 5.24: Numerical experiment, using different boundary parameters for the rotation

The influence of the boundary condition on the steady-state profile is clearly visible. The further outward it is set, the smaller the steady-state profile gets, because the rotation gradient becoming flatter. The amplitude and the phase profile are barely affected by these deviations.

Summary

After performing these different numerical experiments, a few basic outcomes should be kept in mind.

- $\chi_\parallel$: the lower the diffusivity, the higher the rotation and the amplitude profile, and the steeper the phase profile
- v_{Pinch}: an inward pinch will increase the rotation and amplitude profile. It affects the speed at which perturbations propagate radially and as such steepens the phase profile
- Π_{RS}: the presence of the residual stress itself does not effect the Fourier profiles, only the steady state. But it can impact these quantities if the residual stress used is proportional to quantities that modulate, e.g. n_e or χ_φ

Chapter 6

Optimization

In this chapter the introduced model and methods are applied to the experimental data and the results of different parameter scans are presented.

6.1 Fit transport parameters with constant Prandtl number

A first approach was to use a constant Prandtl number $Pr(\rho_\varphi) = Pr$ and to neglect the residual stress. To do so, a 3D scan was performed on the Prandtl number and the constants `CHE1` and `CHE2` such that the Pinch (cf. Equation 2.6) were varied through all possible combinations on a reasonably chosen grid. The optimization routines found `CHE1` $= 0$, `CHE2` $= 2.3$, and $Pr = 1.5$ for #34027. The resulting profiles are presented in Figure 6.1.

One can clearly see that the rotation and amplitude profiles are too low, especially for small ρ_φ. After learning about the dynamics of these quantities in the previous chapter, this is a clear indicator that one has to decrease the Prandtl number for small ρ_φ, but keep the value of $Pr = 1.5$ for the edge. This suggests a linearly increasing dependency.

It should be noted at this point that this calculation was also performed for #34047 and #34042 and gave similar results with $Pr(\#34047) = 1.2$ and $Pr(\#34042) = 1.25$. A promising observation is that the optimized parameters for the pinch are very close to the ones found for #34027 such that one can expect to recover similar transport coefficients for these discharges.

6.2 Predictions from GKW calculations

To give a first estimate for the linear dependence of the Prandtl number, the GKW code is used. The GKW calculation for this thesis was performed by Dr. Clemente Angioni. Since all relevant profiles used as inputs to GKW were found to agree within error bars, only one calculation was carried out for #34027.

As a result of these calculations one obtains the spectral averaged quantities $R\,v_\varphi/\chi_i$ and $R\,v_\varphi/\chi_\varphi$ for different radial positions, where v_φ is the pinch velocity.

$$\begin{aligned} \rho_\varphi &= \{0.3, 0.4, 0.5, 0.6, 0.7\} \\ (R\,v_\varphi/\chi_i)_{GKW} &= \{-0.37256, -0.674851, -1.01437, -1.29305, -1.39628\} \\ (R\,v_\varphi/\chi_\varphi)_{GKW} &= \{-0.592205, -0.879491, -1.08965, -1.21801, -1.0466\} \\ Pr_{GKW} &= \chi_\varphi/\chi_i = \left(\frac{R\,v_\varphi}{\chi_i}\right)_{GKW} \cdot \left(\frac{\chi_\varphi}{R\,v_\varphi}\right)_{GKW} \\ &\approx \{0.63, 0.77, 0.93, 1.06, 1.33\} \end{aligned}$$

This $Pr(\rho_\varphi)_{GKW}$ was linearly fitted [44] as shown in Figure 6.2. The fit yields

$$Pr = 0.0925 + 1.70428\,\rho_\varphi. \tag{6.1}$$

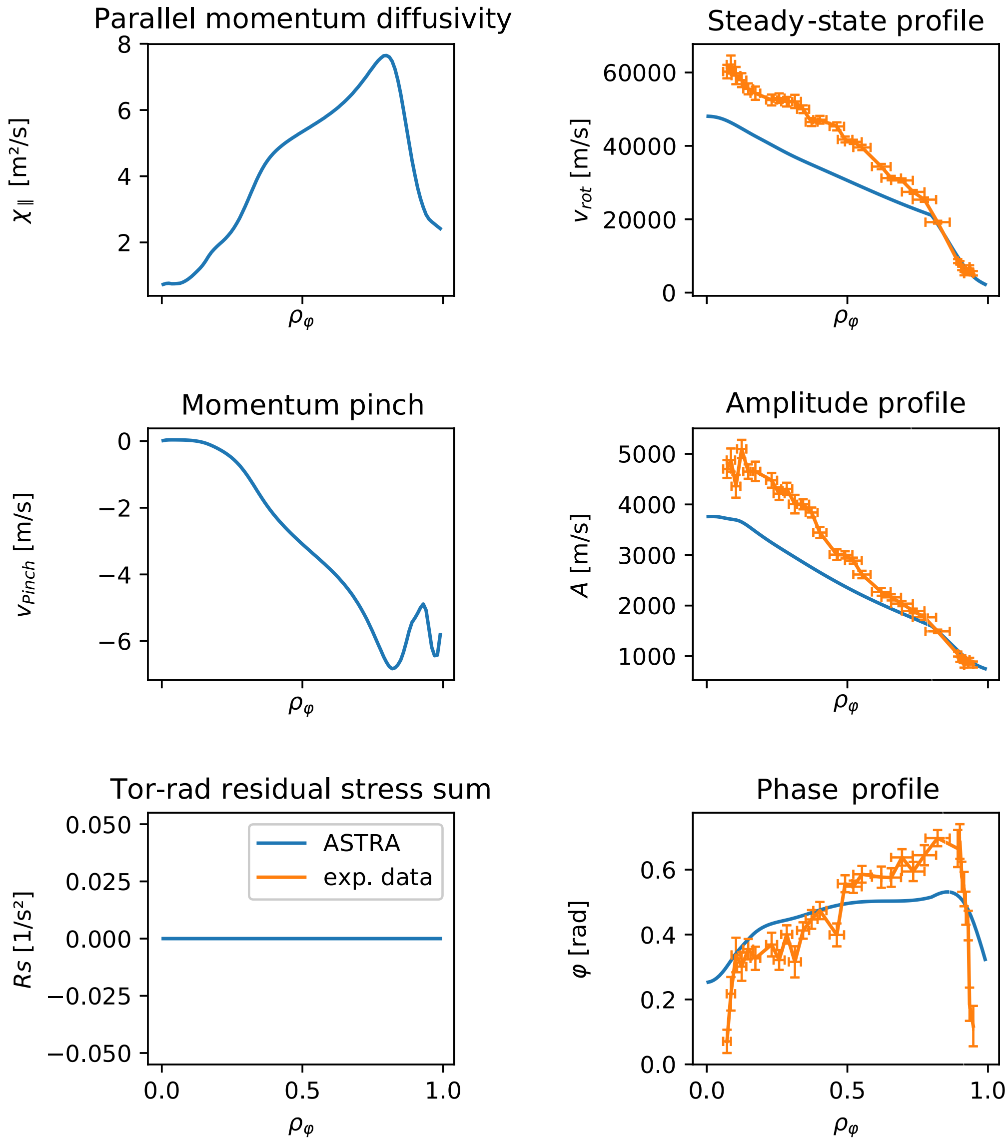

Figure 6.1: ASTRA simulations with a constant Prandtl number and optimized pinch, #34027

From these GKW calculations one can also compute the pinch velocity. GKW gives $(R\,v_\varphi/\chi_i)_{GKW}$ and from equilibrium reconstruction one can calculate R, the flux-surface-averaged major radius. Within these calculations the approximation $R = (R_{LFS} + R_{HFS})/2$ was used. To calculate the experimental ion heat diffusivity, one uses the TRANSP output (`CONDI` and `XINC`) and reconstructs the turbulent part of the heat diffusivity.

$$\begin{aligned}
\rho_\varphi &= \{0.3, 0.4, 0.5, 0.6, 0.7\} \\
R &= \{1.7049, 1.69864, 1.69192, 1.68492, 1.67773\}[\mathrm{m}] \\
\chi_{i,turb} = \mathtt{CONDI} - \mathtt{XKINC} &= \{0.648699, 1.12374, 2.09313, 3.62547, 4.45668\}[\mathrm{m}^2/\mathrm{s}] \\
(R\,v_\varphi/\chi_i)_{GKW} &= \{-0.37256, -0.674851, -1.01437, -1.29305, -1.39628\} \\
v_{\varphi,GKW} = \frac{\chi_{i,turb}}{R} \cdot \left(\frac{R\,v_\varphi}{\chi_i}\right)_{GKW} &= \{-0.141755, -0.44645, -1.25491, -2.78228, -3.70904\}[\mathrm{m/s}]
\end{aligned}$$

Also a fit is performed as shown in Figure 6.3. The used ansatz was

$$\begin{aligned}
v_\varphi(\rho_\varphi) &= a \cdot \arctan(b \cdot \rho_\varphi + d)\,[\mathrm{m/s}] \\
v_\varphi(\rho_\varphi = 0) &= 0\,[\mathrm{m/s}].
\end{aligned}$$

The fit parameters are:

$$\begin{aligned}
a &= -1.496 \\
b &= +12.152 \\
d &= -6.8.
\end{aligned}$$

An ASTRA simulation for #34027 making direct use of this Prandtl number and pinch while neglecting any residual stress leads to the profiles shown in Figure 6.4.

One can clearly see that this modification of the model goes into the right direction, especially the increase of the steady-state profile as well as the amplitude profile in the core. Since the Prandtl number is the most robust prediction from this kind of calculation, one makes use of the linear Prandtl number fit (cf. Equation 6.1) for all further calculations in this thesis.

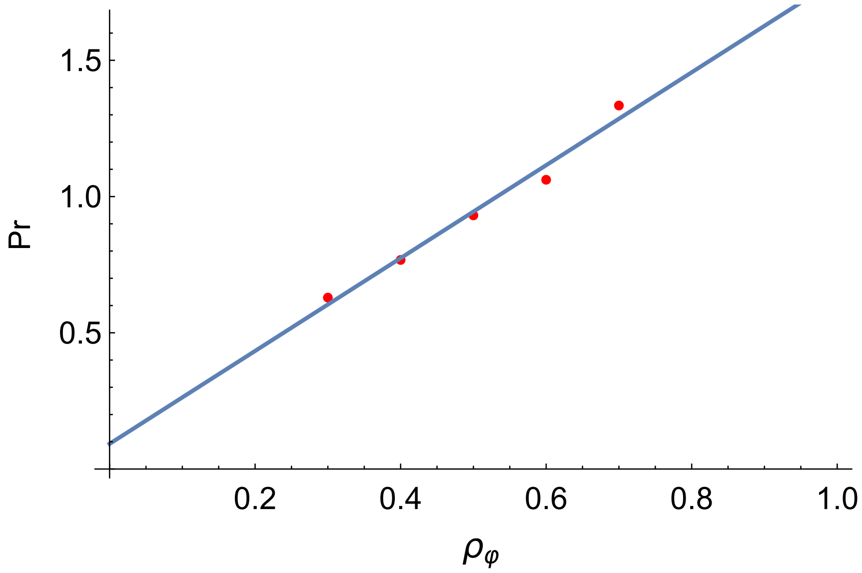

Figure 6.2: GKW-predicted Prandtl number for #34027 (linear fit in blue)

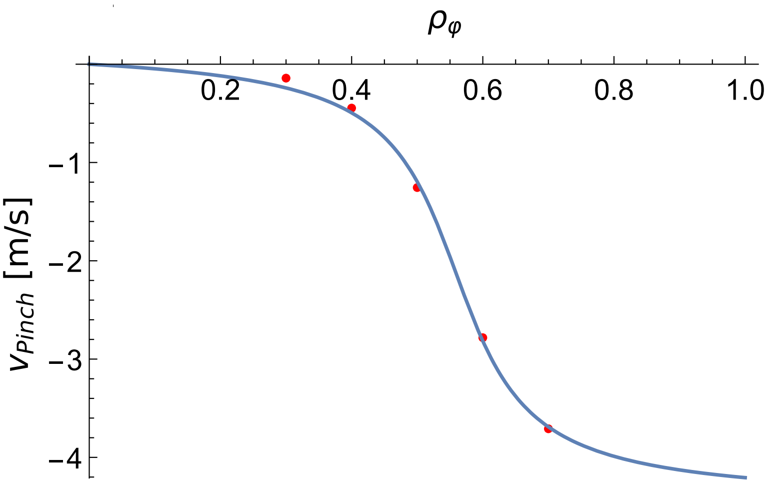

Figure 6.3: GKW-predicted pinch for #34027 (fit in blue)

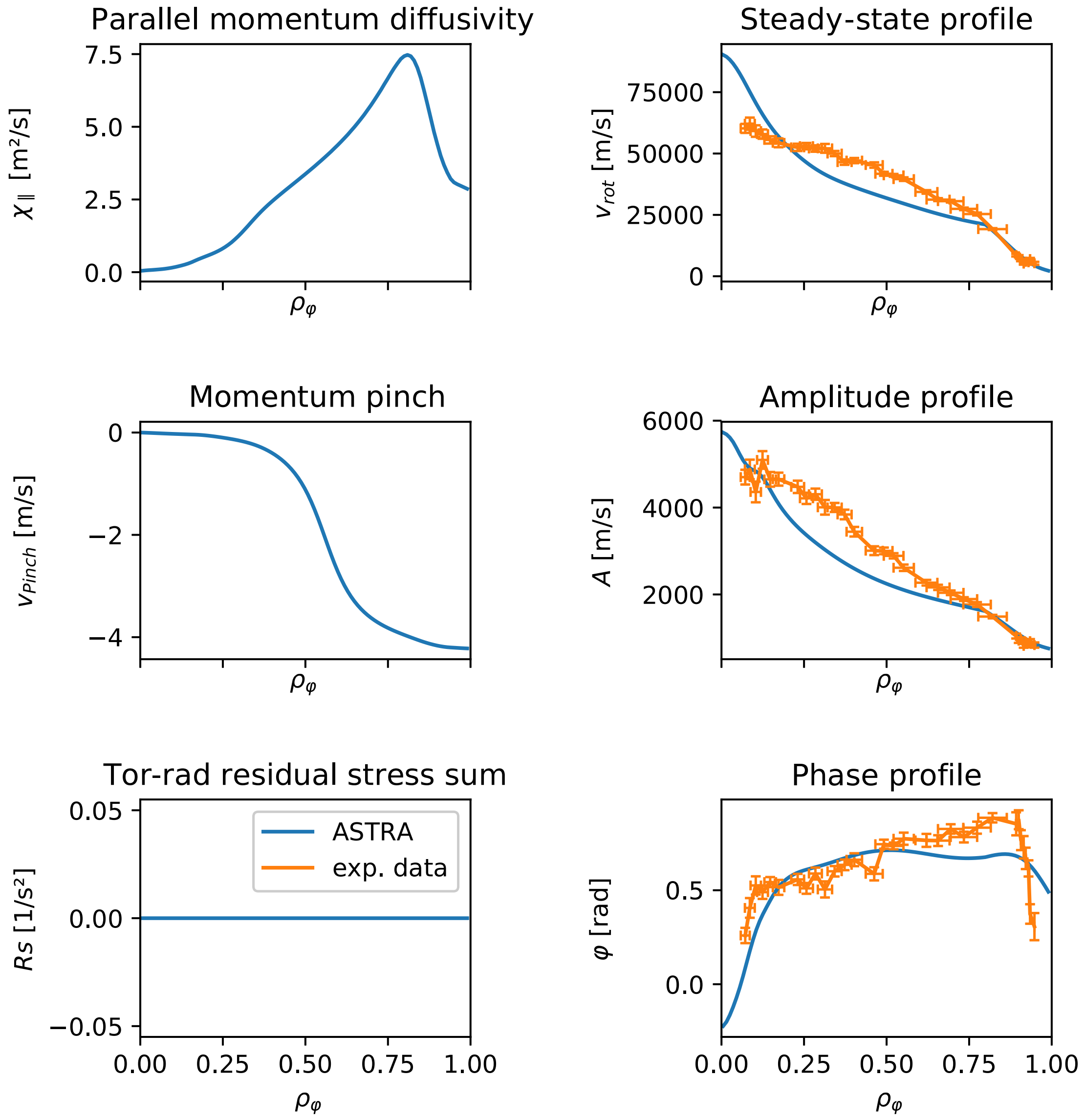

Figure 6.4: ASTRA simulation with GKW Pr and pinch, #34027

6.3 Fit transport parameters on Fourier profiles

Since the numerical experiments showed that the residual stress does not directly affect the Fourier profiles but only the steady state profiles, it should be possible to find the best solution for the Prandtl number and the pinch parameters by optimizing on the rotation modulation only, i.e. by subtracting off the steady-state profile before comparing (cf. Equation 3.2). This is done without including a residual stress. Once the best Prandtl number and pinch are found that reproduce the amplitude and phase profiles, a residual stress can be solved to match the experimental steady-state profile.

A parameter scan on a grid of parameters for the scaling of the Prandtl number (`CHE3`) and the two pinch parameters (`CHE1` and `CHE2`) is performed for all selected discharges. This leads to the results shown in Figure 6.5 and 6.6. In Figure 6.5, the best solution for the pinch parameters are shown. In general, the contribution to the pinch scaling with the density gradient, `CHE1`, is rather small compared to the shear part, `CHE2`. From an experimental point of view, this is because the pinch needed to reproduce the data is small in the center and increases towards the edge, making the shape of the shear profile better suited to providing the required pinch. `CHE2`, the scale factor on the shear, varies by a factor of three. This directly leads to a factor of three variation in the pinch and a similar deviation in the Prandtl number is then needed to reproduce the amplitude and phase profiles. This variation in the Prandtl number scaling is shown in Figure 6.6. However, for all of the considered discharges except #34063.2, it is possible to find a combination of `CHE2` and `CHE3`, that minimizes the `quality` value shown in Figure 6.7 for #34027. #34063.2 was removed due to this unexplained runaway behavior.

Obviously, it is not possible to find a set of common parameters for `CHE1`, `CHE2`, and `CHE3` to stay within the error bars of these results as shown in Figures 6.5 and 6.5. While in fact a minimum for `CHE3` was found, the differences in the phase and amplitude profiles produced with a given combination of `CHE2` and `CHE3` are almost negligibly small. This is shown in Appendix B. For a given `CHE2` or `CHE3` an equally good solution can be found. Therefore, one has to impose some constraints, e.g. fixing the GKW Prandtl number.

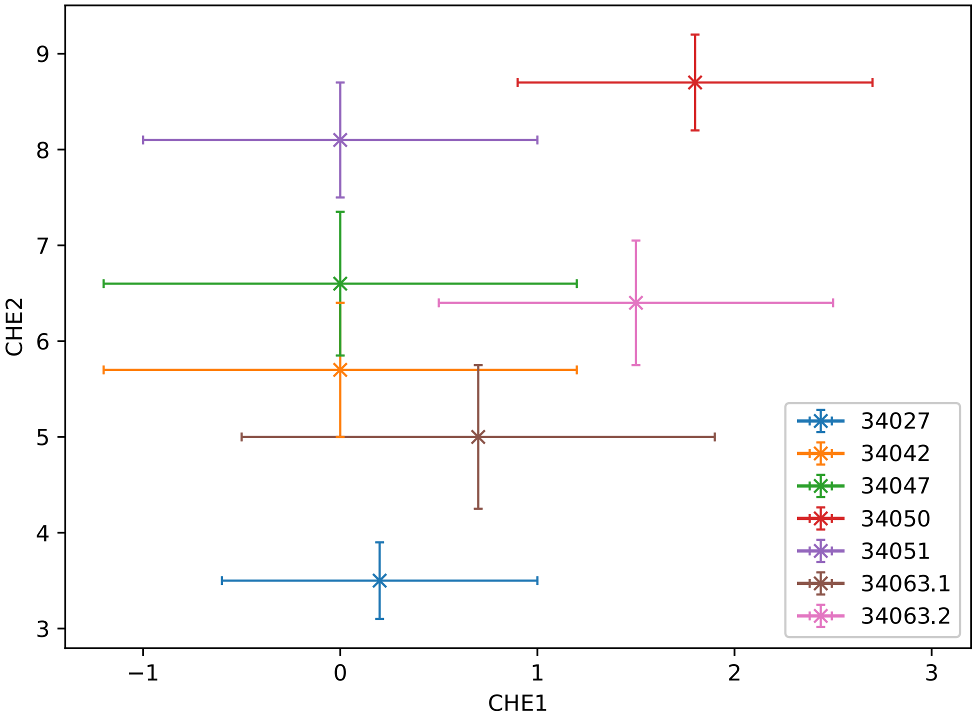

Figure 6.5: Best pinch parameters (`CHE1` and `CHE2`) when optimizing the pinch and the Prandtl number to reproduce the experimental phase and amplitude only

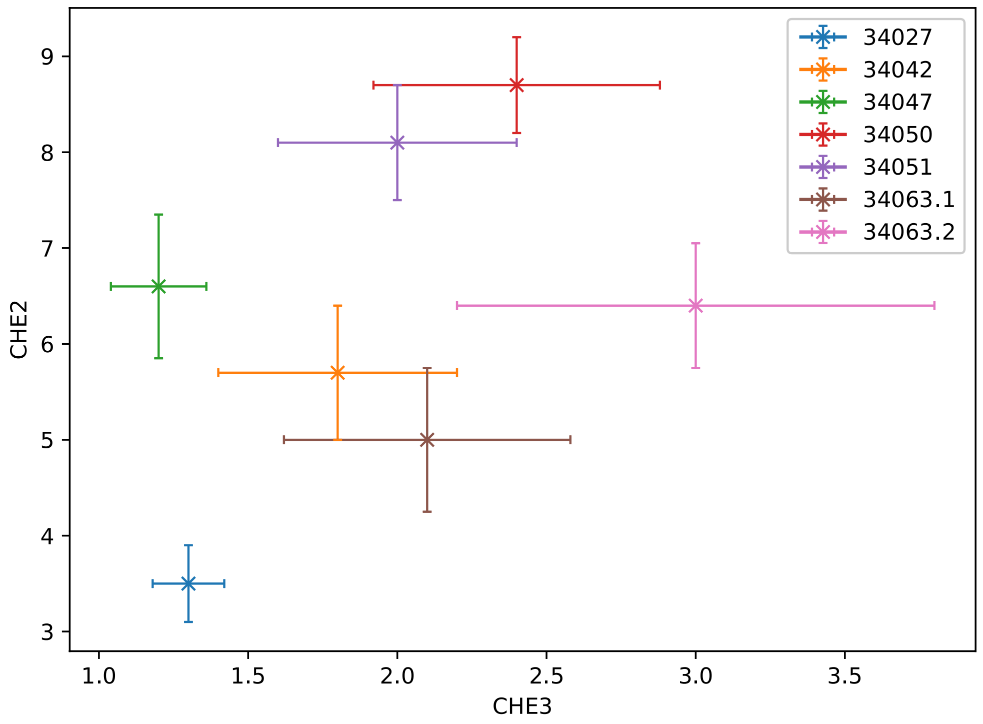

Figure 6.6: Best Prandtl number scaling (`CHE3`) and shear scaling pinch parameter (`CHE2`) when optimizing the pinch and the Prandtl number to reproduce the experimental phase and amplitude only

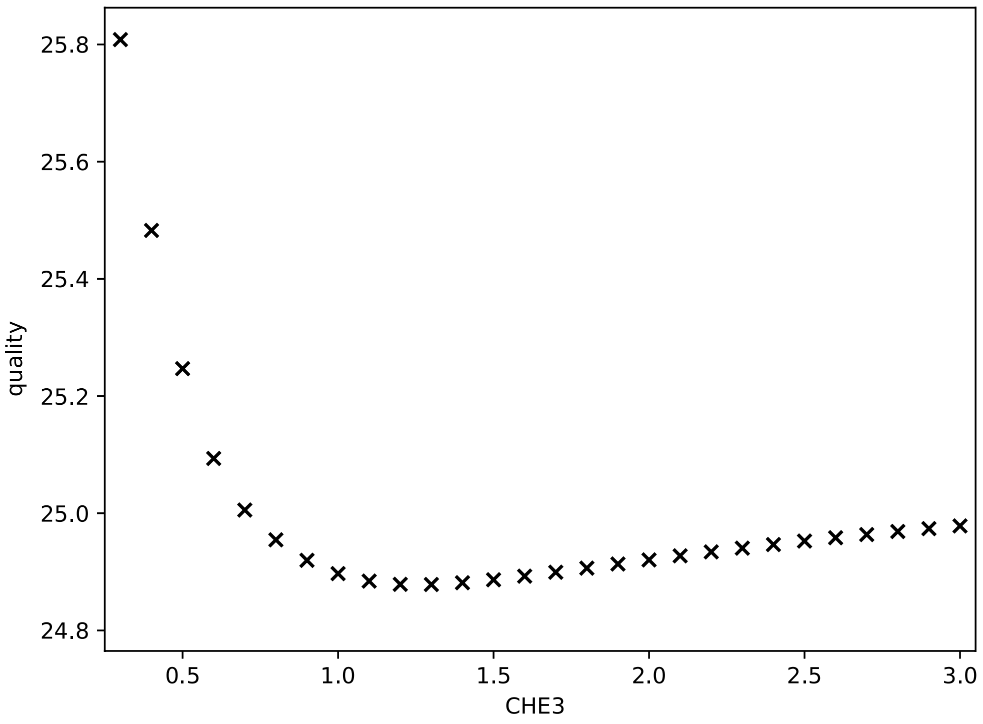

Figure 6.7: Scanning the parameter `CHE3` and the effect on the `quality` (to be minimized), #34027, when optimizing the pinch and the Prandtl number to reproduce the experimental phase and amplitude only

6.4 Fit transport parameters on full rotation profiles

Finally, an optimization is carried out on the full modulated rotation profile using Equation 3.1 in the optimization routines opposed to just fitting the phase and amplitude profile in the section before. The residual stress was neglected. As in the last section, degenerate solutions for the pinch and the Prandtl number were observed. By fitting `CHE1`, `CHE2`, and `CHE3` to the full rotation profiles, a runaway behavior was found for the parameter `CHE3` scaling the Prandtl number. Without finding significantly better solutions, this just lead to very large diffusivities and pinches. Therefore, the Prandtl number was set to the GKW Prandtl number by `CHE3` $= 1$. Thus, in all further calculations, the GKW Prandtl number was used without any scaling, leading to unique solutions for the pinch parameters.

In general, for all cases `CHE1` is nearly zero while `CHE2` is sizable and varies by about 20% as shown in Figure 6.8. In addition, there is a clear separation into two groups: the upper three data points (#34050, #34051, and #34063) correspond to the profiles with ICRH modulation. The fact that `CHE1` is near zero while `CHE2` is relatively large reflects the need for an inward pinch that increases from the center to the edge in order to reproduce the experimental modulation profiles. The experimental density profile seems to be too flat, especially in the outer half of the radius, to contribute to the pinch in the needed way (cf. Figure 5.22).

Comparing the resulting rotation profiles with best parameters to the experimental ones (cf. Chapter 7.1), one finds good agreement between the optimized ASTRA simulation and the experimental values for the amplitude profile for #34027, #34042, #34051, and #34063. #34050 is not well modelled, #34047 is slightly underestimated. Considering the phase profiles, the calculations match the experimental values for #34042, #34047, #34050, and #34051. #34027 is slightly too small for large radii. Regarding #34063, the experimental phase profile is too noisy to perform a valid comparison.

Looking at the profiles for the pinch v_{Pinch} and the momentum diffusivity $\chi_{\|}$, see Figure 6.10, one recovers the two groups found in the parameters as shown in Figure 6.8. #34063 is on the borderline between these two groups. In general, until a $\rho_{\varphi} \approx 0.7$, the profiles agree within error bars. To make comparison with other published results easier, Figure 6.9 shows the pinch number of two optimization results compared with the GKW prediction. While the two discharges, #34027 and #34050, show no agreement within error bars for the pinch and the diffusivity, the pinch number as a more general quantity does. The pinch number results are larger than predicted by GKW by a factor of two. The reason for this is unclear, but similar results were observed in other experiments as discussed in Chapter 7.2 and require further investigation.

All of the steady-state rotation profiles show a clear gap between the experimental and the simulated rotation. This suggests a missing contribution from a residual stress as can be seen for #34027 in Figure 6.11.

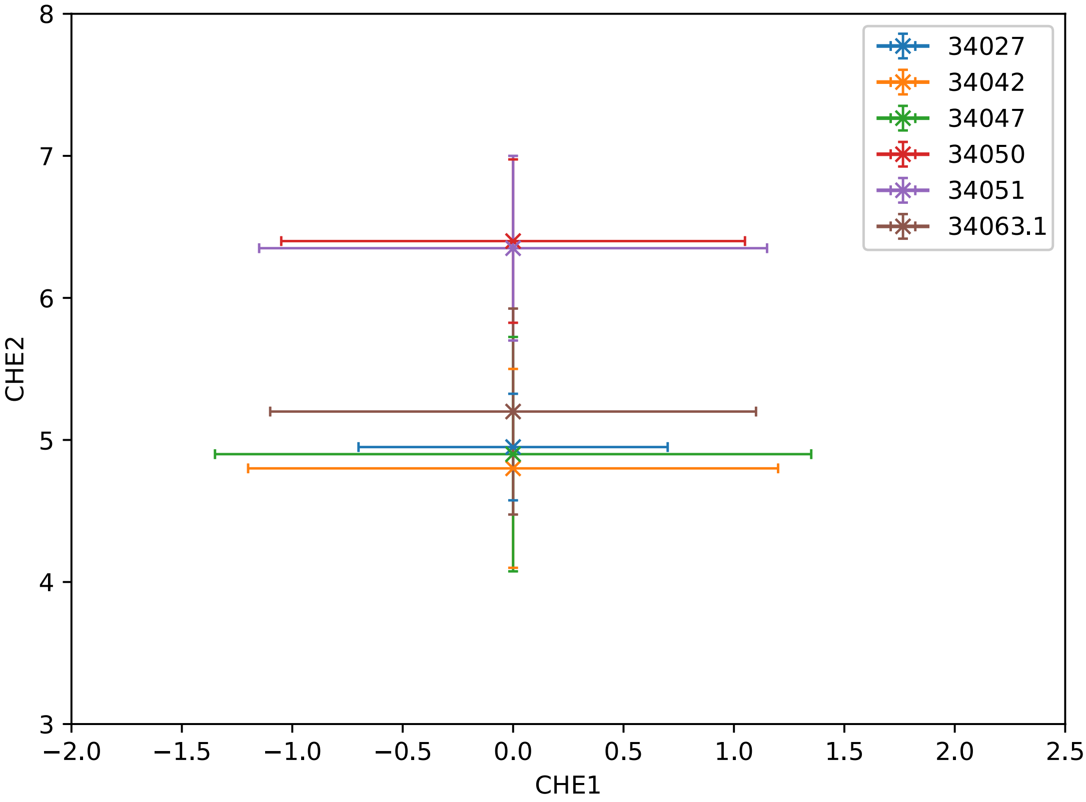

Figure 6.8: Best pinch parameters with GKW Prandtl number optimized to best match the full rotation profile

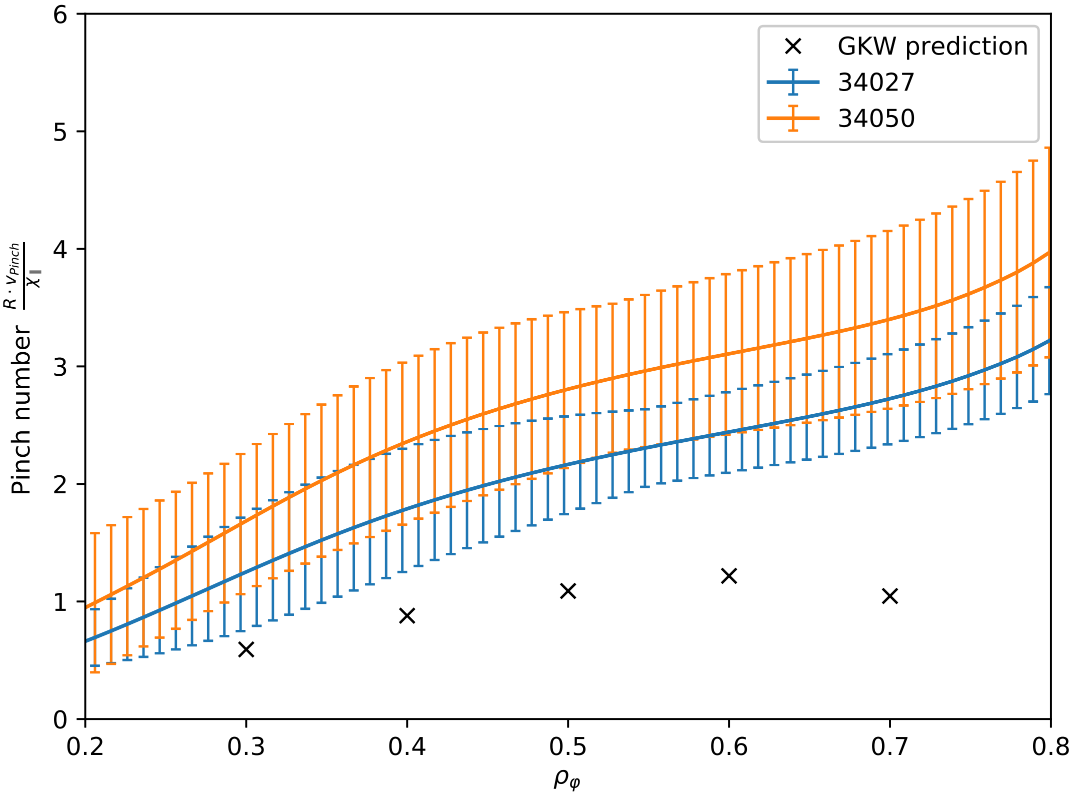

Figure 6.9: Pinch number of two optimization results compared with the GKW prediction

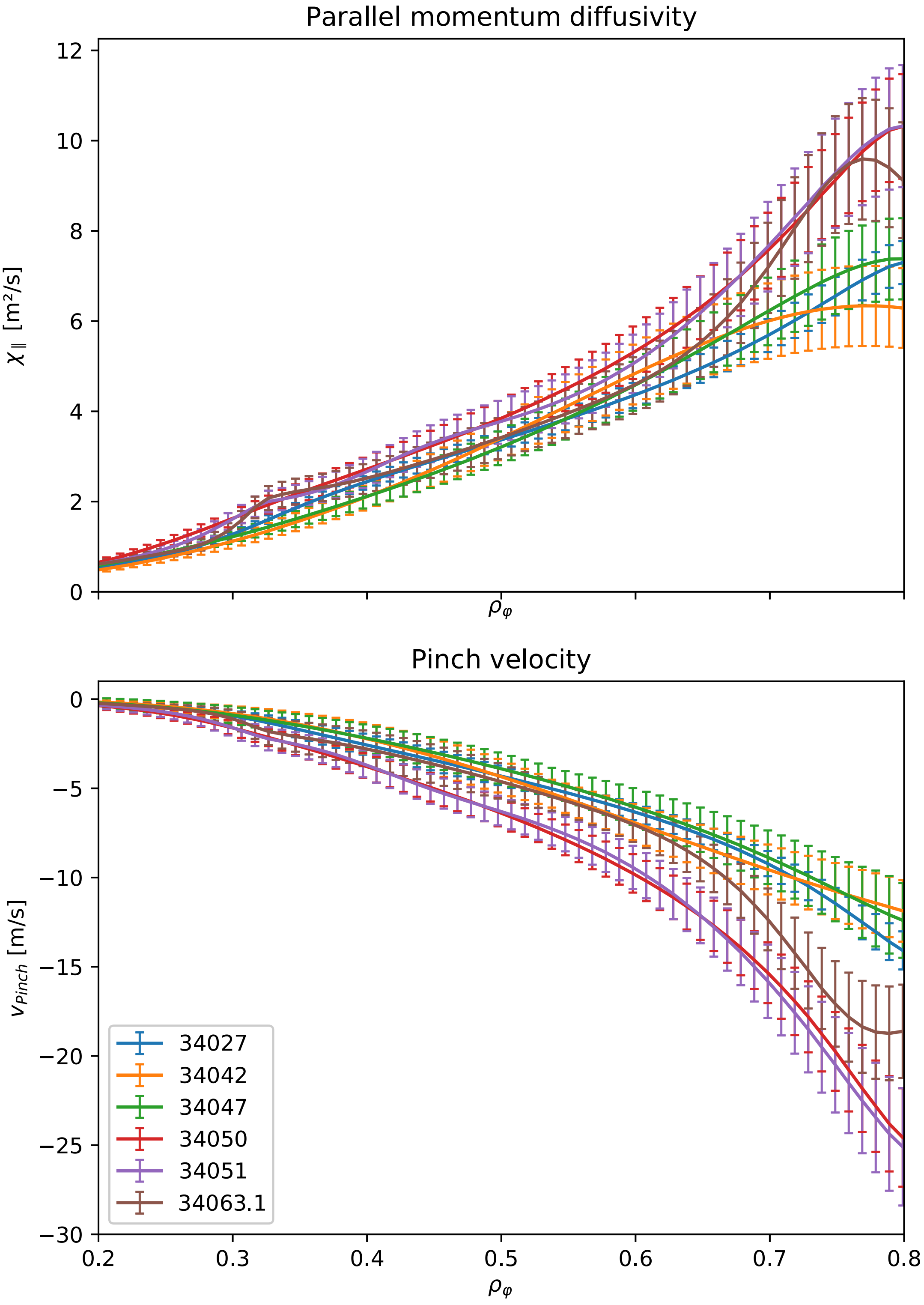

Figure 6.10: v_{Pinch} and $\chi_\parallel$ for best pinch parameters with GKW Prandtl number optimized to best match the full rotation profile

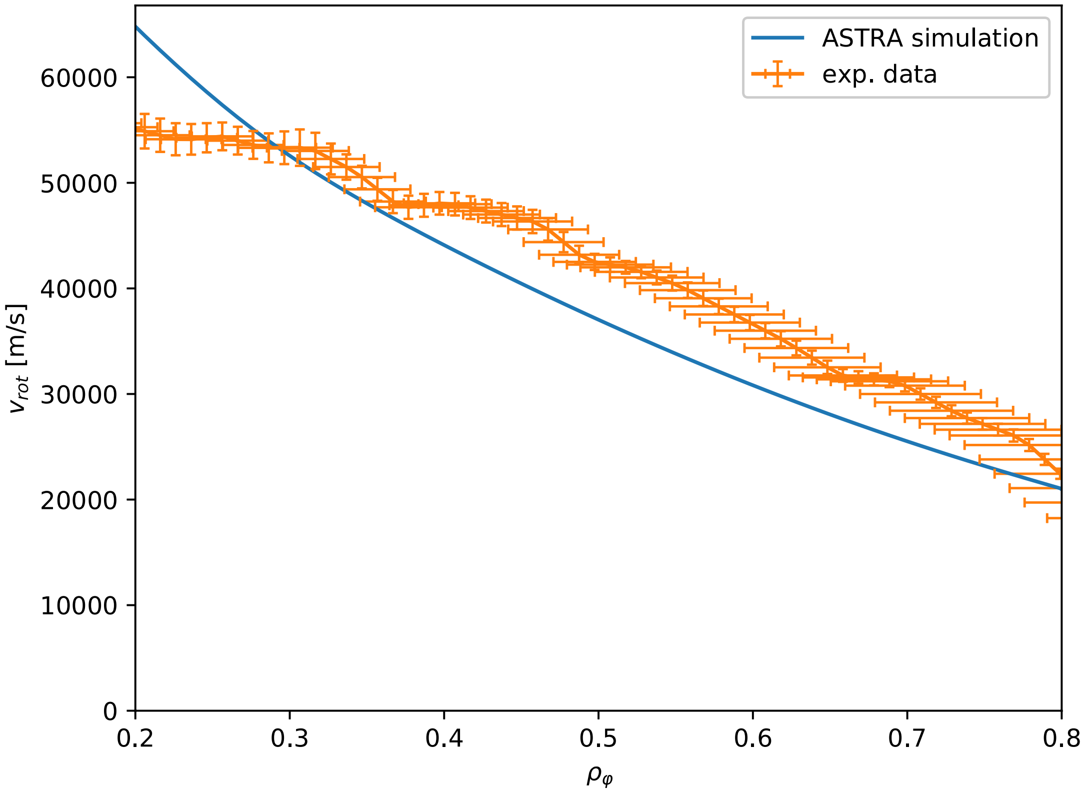

Figure 6.11: Comparison between the simulated rotation and the experimental data for best pinch parameters optimized to match the full rotation profile, #34027

6.5 Predictions for the residual stress

In this section predictions about the residual stress needed to explain the experimental results will be made. First, the intrinsic rotation caused by the residual stress is estimated. To do so, the difference between the simulated and the experimental rotation profiles is taken for all cases. This is shown in Figure 6.12. Remarkably, the difference is the same for all cases, indicating that the same residual stress is present in each of the plasmas. This is expected, as the plasmas are extremely similar, but the clarity of the result is impressive.

One observes the intrinsic rotation to act counter-current until $\rho_\varphi \approx 0.3$ and co-current above. Since MHD effects like sawteeths flatten the steady-state rotation profile, a comparison is invalid inside $\rho_\varphi < 0.3$. The residual stress needed to cause this intrinsic rotation is of the order of $\Pi_{RS} \approx 0.2$ Nm/m^3 at midradius and has roughly 70 % of the size of the NBI torque there. This was determined by altering the applied torque in ASTRA until the intrinsic rotation profile was brought to zero.

Fitting this residual stress with Equation 2.7 was tested within the work for this thesis, optimizing the pinch and the residual stress on the full profiles while fixing the Prandtl number. It was found that this leads to a very good agreement of the rotation profile and good results for the phase, but slightly underpredicts the amplitude profiles. A more detailed study with an improved ansatz for the residual stress and for the numerics is needed.

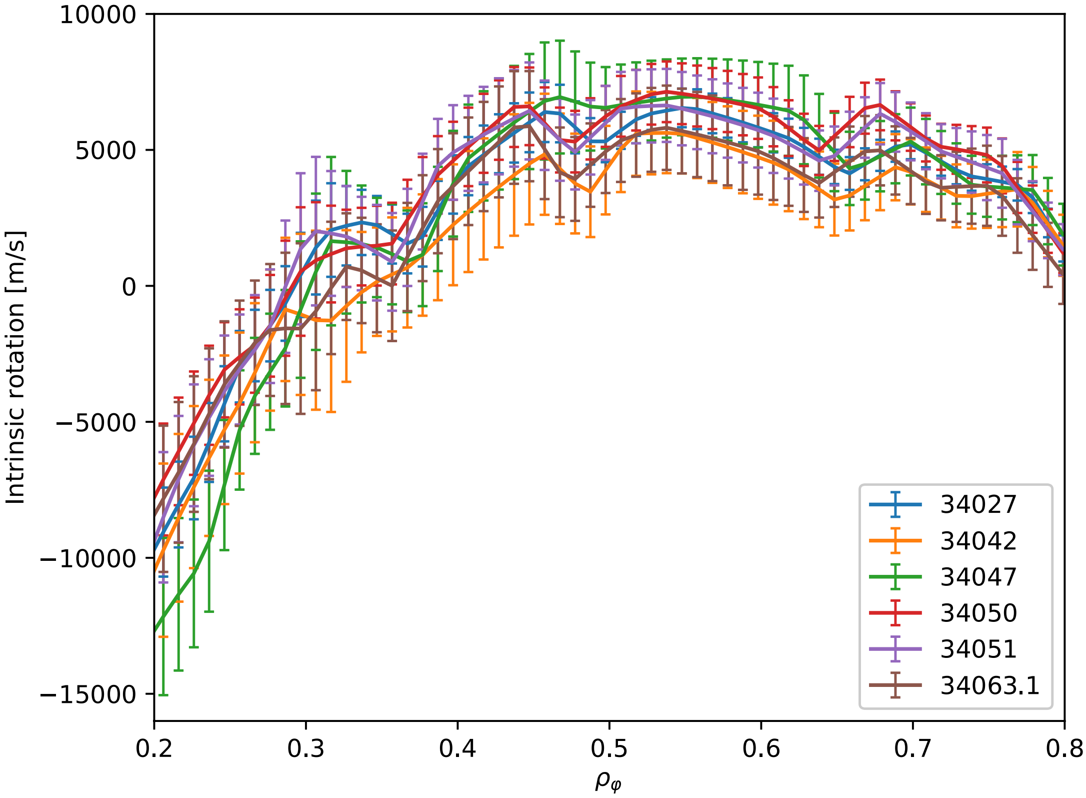

Figure 6.12: Estimated intrinsic rotation for the considered discharges, where sawtheeth effects were observed for $\rho_\varphi < 0.3$. Co-current intrinsic rotation observed for $\rho_\varphi > 0.3$. Error bars reflect the experimental uncertainty on the rotation profiles only.

Chapter 7

Summary

In this chapter an overview of the results is given. A discussion and an outlook close this thesis.

7.1 Results

Within this thesis, a methodology for extracting momentum transport coefficients from NBI modulation experiments was studied and validated. This was tested for a modulation frequency of $f_{\mathrm{mod}} = 3$ Hz, where the Fourier profiles of the rotation were found to have sufficiently small noise. After a detailed comparison, a set of seven discharges was found to show identical background profiles within error bars with variation of the imposed perturbation. Initial tests showed that it was not possible to reproduce the amplitude profiles with a constant Prandtl number, rather a linear one was needed increasing from the core to the edge. This turned out to be in very good agreement with the predictions from GKW. GKW, however, underpredicts the pinch.

Further tests showed that allowing the linear Prandtl number to vary provides too much flexibility and multiple solutions can be found for the Prandtl number and the pinch that reproduce the amplitude and the phase data almost equally well. Therefore, it was determined that the Prandtl number was fixed to the GKW prediction. After that it was possible to find pinch profiles that reproduce the Fourier profiles of the rotation very well as depicted in Figure 7.1-7.6. The used transport coefficients were found to agree within error bars (cf. Figure 6.10).

Considering the amplitude profiles, all were found to be in good agreement, only the graph for #34050 seems underpredicted, which could be the result of a higher over all heating power leading to small differences in the electron and ion temperature and modulation profiles (cf. Table 4.3). Looking at the phase profiles, good agreement was found in general, just #34063 does not match, but here the experimental phase profile is very noisy and hard to fit.

The pinch velocity and momentum diffusivity corresponding to the optimized transport coefficients show good agreement within error bars as shown in Figure 6.10. Four of six data sets can be reproduced with the same pinch and diffusion. The remaining, #34050 and #34051, require higher pinches. These data sets exhibit very flat phase profiles, making the modeling problematic. Here, ICRH heating was used in- and out-of-phase and they show the tendency of different temperature perturbations than the other four discharges. It should be noted that the pinch number for these discharges coincide within error bars.

The intrinsic rotation, calculated from the mismatch between the simulation and the experimental data for the rotation, acts mainly co-current in the considered radial position in agreement with theoretical predictions (cf. Chapter 2) and earlier analysis of ASDEX Upgrade discharges with dominant ITG turbulence. Also, observations at other machines have shown co-current residual stress, e.g. at DIII-D. All discharges with same background profiles exhibit the same residual stress, causing the same intrinsic rotation in size and shape.

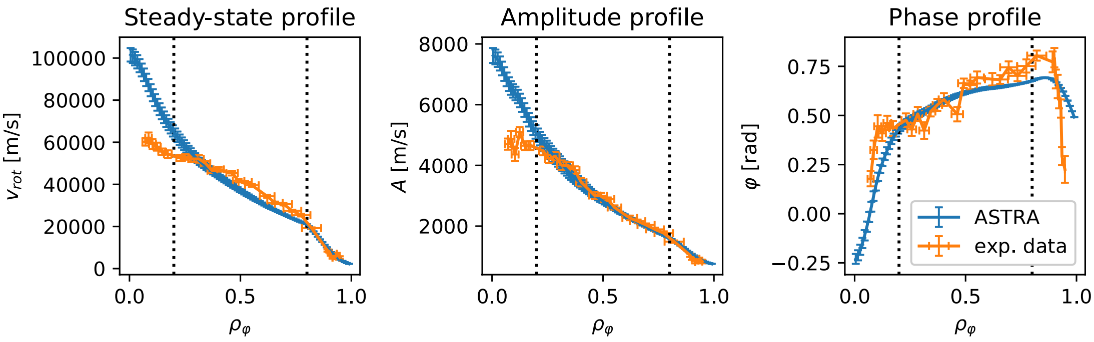

Figure 7.1: Optimization results, #34027

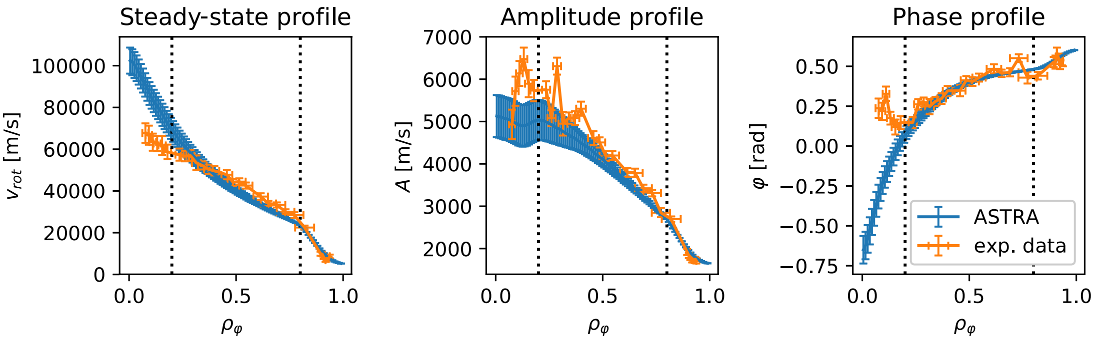

Figure 7.2: Optimization results, #34042

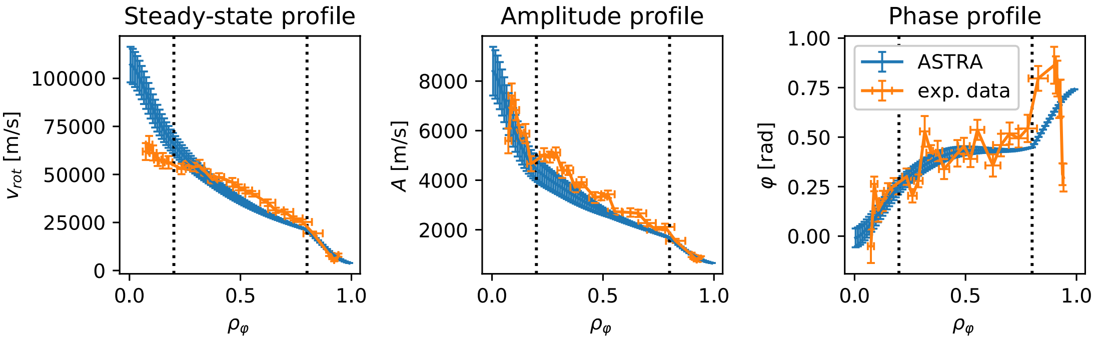

Figure 7.3: Optimization results, #34047

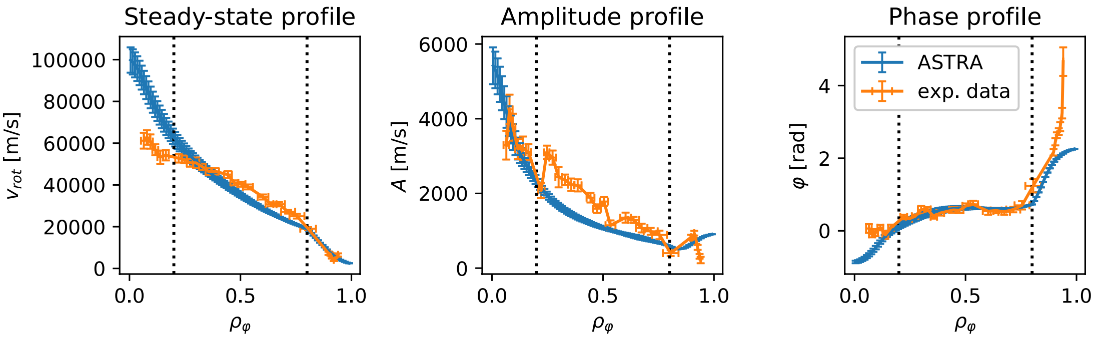

Figure 7.4: Optimization results, #34050

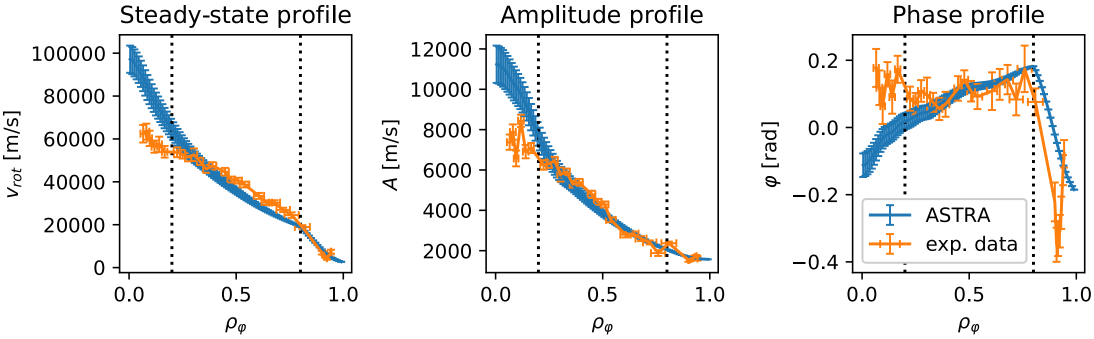

Figure 7.5: Optimization results, #34051

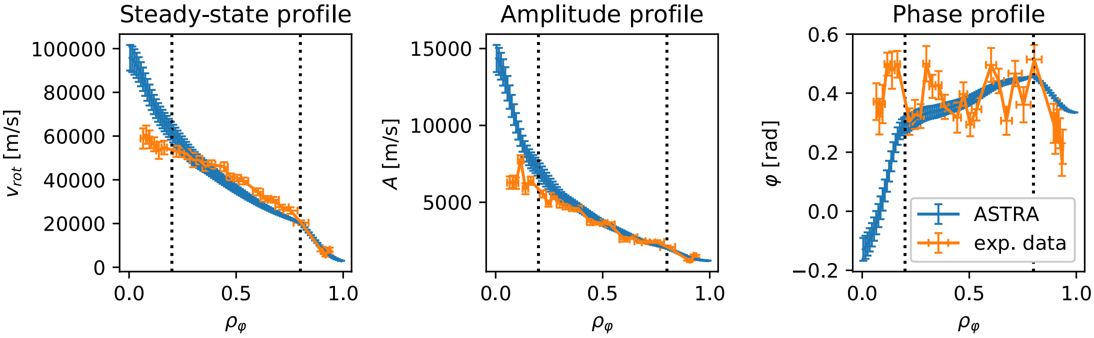

Figure 7.6: Optimization results, #34063.1

7.2 Discussion

The methodology and the results presented can be compared with previous analyses of this data as well as experiments performed at other devices. Firstly, this is done by comparing the results for the #34027 discharge between the best optimized solution from this work, the results of the GKW simulations, and the results of a optimization performed by Dr. Fable. Then, an overview of the results from other machines and discharges is given.

The first comparison between GKW, the results from Dr. Fable, and the ones obtained in this thesis is depicted for #34027 in Figure 7.7. One has to mention that the residual stress Dr. Fable found is not included in this comparison. The results from the GKW simulation are shown in orange. This combination underestimates the amplitude profile and results in a much flatter profile than seen in the experiment. The optimized solution from this thesis (blue) on the other hand and the solution from Dr. Fable (green) reproduce the experimental data quite well.

The corresponding transport coefficients on the other hand are quite different. Dr. Fable assumed a fixed Prandtl number of 0.9, while the here optimized solution used the Prandtl number from GKW. These lead to different pinch profiles needed to reproduce the phase. With the lower Prandtl number, Fable's result also needs a smaller pinch, so it is in better agreement with the GKW result. The optimized solution on the other hand with the GKW Prandtl number requires a larger pinch to balance the outward diffusion. The resulting profiles are very similar, reminiscent of the degeneracy discussed previous in Section 6.3. However, in this case, the optimized solution does a better job of reproducing the experimental phase profile, and this is a direct result of using a linear varying Prandtl number instead of a fixed one.

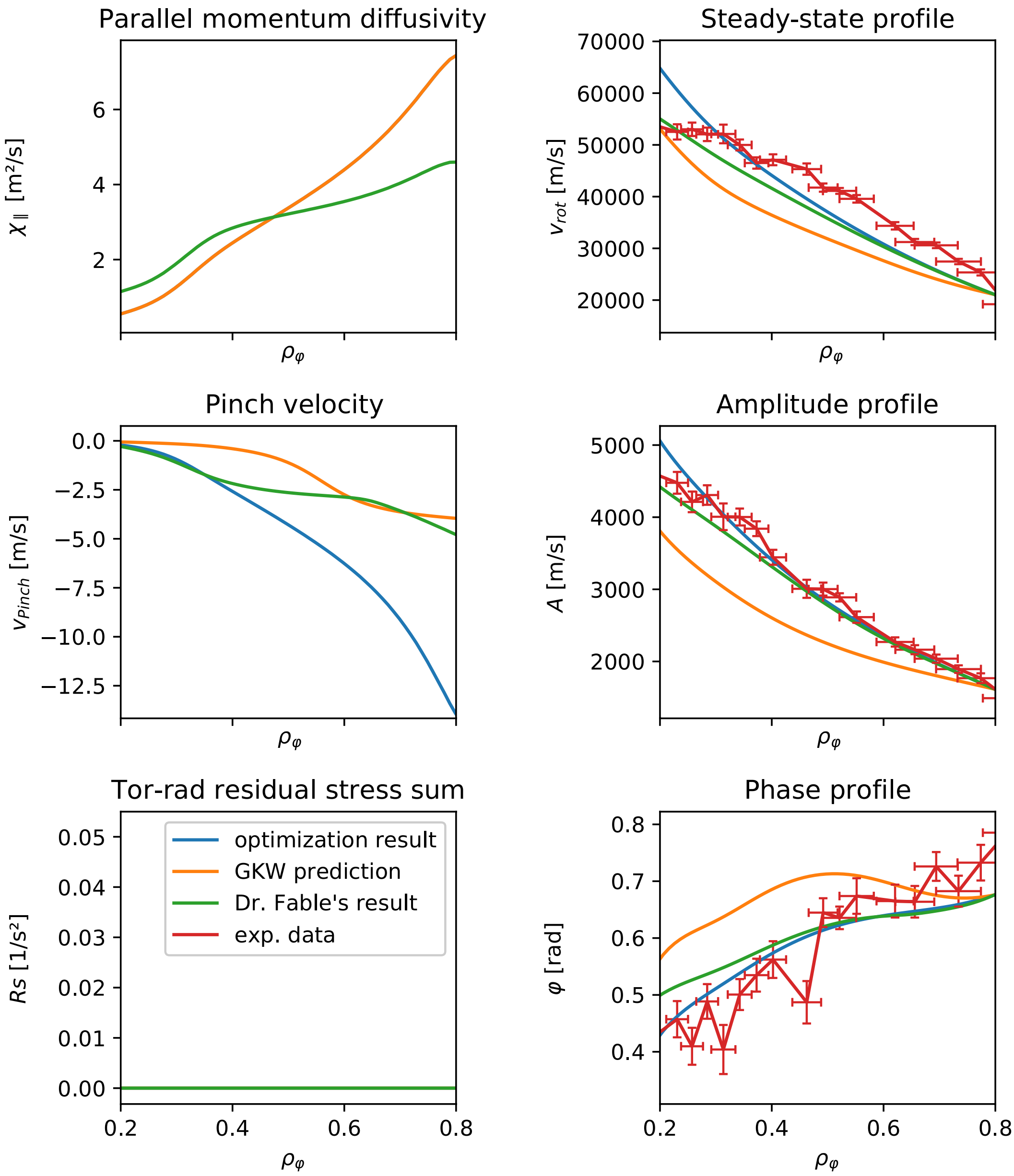

Figure 7.7: Comparison of the results of this thesis with GKW predictions and Dr. Fable's results, #34027

Already in 2007, Tala *et al* [45] found good qualitative agreement between theoretical predictions and experimental observations for the Prandtl number and the pinch for JET, where he saw a strong inward Pinch velocity leading to a low effective Prandtl number. In 2011, Tala *et al* [46] compared discharges at JET with GS2 and GKW simulations. There, a similar approach was taken: NBI modulation in a plasma dominated by ITG modes, using TRANSP and ASCOT to calculate the torque, neglecting high-frequency MHD modes such as sawteeths, ELMs, and equilibrium recalculation and comparing the simulation with the experiment. Both in theory and experiment, a strong dependence of the pinch on the inverse density gradient was found. The safety factor, which is connected with the shear, contributed only weakly to the pinch. The results for the pinch number are qualitatively similar. In agreement with Tala's observations, it is radially increasing. The boundaries coincide. Further agreement can not be demanded, because the plasmas are different. In general, the theoretical predicted pinch was found to be smaller by Tala than the experimental obtained one. This agrees with the results of this thesis.

The Prandtl number Tala found in his simulations is of the same size and same shape as the one found in this thesis. Tala's results suggest the experimental Prandtl number is larger by a factor of two than the theoretically predicted value. The intrinsic rotation found by Tala is, compared to the rotation background, of the same relative size as the intrinsic rotation found in this thesis. Tala *et al* [47] also recovered similar results in a study of DIII-D discharges.

Weisen *et al* [48] analyzed the non-diffusive momentum transport in JET and found a slightly higher experimental effective pinch number compared to the one obtained in this work. This is expected, since in Weisen's work the pinch includes also the contribution from a possible residual stress. If this residual stress is co-current, it increases the effective pinch number. The effective pinch number found in this work was also larger than the one predicted by GKW. However, the interpolation of that comparison is not as clear as it is in this work, due to the lack of separation of residual stress and convective contribution. In addition, the comparison with GKW in Weisen et al is carried out using only two wave numbers, while in this work a broader spectral average was taken.

Yoshida *et al* [49] investigated the parameter dependence of momentum transport coefficients in typical JT-60U L-mode plasma, where they found a similar shape and magnitude for the pinch velocity. It demonstrates the rather big variation of the pinch velocity.

McDermott *et al* [50] studied the influence of the intrinsic rotation in ASDEX Upgrade. The intrinsic rotation in ITG-dominated plasmas was found to be of the same size and shape as in this thesis. Furthermore, it agrees on the strong dependence on the inverse density gradient.

Recently, a similar modulation analysis has been carried out at KSTAR by Yang *et al* [51]. They found that large amplitude perturbations in T_i and χ_i can lead to artificially high momentum transport coefficients. This is very important for this work, where one included χ_i time dependence, and so found transport coefficients that overlap for all cases, including the ICRH cases, but these cases do have slightly larger transport coefficients, consistent with the results of the KSTAR study. This might suggest that in this work one have not yet fully accounted for the time dependence in the Prandtl number or χ_i.

7.3 Outlook

Besides the rather successful calculation of the transport parameters shown in the previous section, it has to be noted that in the use of the introduced model questions remained unanswered. Within the writing process of this thesis, the room for possible solutions was observed to be degenerate such that multiple solutions for the pinch and the Prandtl number were found matching the experimental data equally well. This lead to the situation that the optimization routines showed a runaway behavior with increasingly large pinch velocities compensated by increasingly large diffusivities. Besides the fact that scans with more parameters increase the computation time significantly, this rather unstable behavior is also the reason why no higher dimensional scans for more parameters were performed, but rather to fix one parameter as done with the GKW Prandtl number.

Maybe this asks for either better numerical approaches like a combined fitting of the full profile and the Fourier profiles or more detailed predictions and models or it could be a ubiquitous feature, inherent to the problem. It would be valuable to use GKW to reevaluate the theoretical transport parameters for the other considered discharges to get a feeling how small changes in the profiles affect the calculations and how a time-dependent calculation for cases with ICRH modulation would affect the so far time-independent Prandtl number.

Finding the pinch parameter scaling with the logarithmic density gradient to be zero for the calculations raises suspicions if it is reasonable to constrain the two pinch parameters to positive numbers. Alternatively, one could just demand the total contributions of both to remain positive. One gets the impression that the parameters were merely used as basis functions to a fitting problem rather than to reflect correct physics. To investigate this, more discharges with varying density gradients has to be performed in ASDEX Upgrade.

Besides that, it is in fact very promising to recover the same intrinsic rotation in all these discharges with similar background profiles. One should take more time to implement the residual stress properly in the used model, maybe considering other dependencies beyond the density gradient as done for example by Dr. Camenen [23].

Among the performed modulation discharges at ASDEX Upgrade were a number of discharges with NBI modulation frequencies of 7 Hz and 10 Hz. For all of the 7 Hz discharges, the TRANSP runs were performed with the suffix `A02`. The 7 Hz discharges provide an even wider variation in applied NBI modulation than was considered here, and if the noise proves to be sufficiently small, the analysis of these discharges would provide further validation of the methods and results of this thesis. Furthermore, an analysis of the Fourier profiles for the second harmonics of the modulation frequency should be studied in detail. The study carried out in this thesis should be the starting point to check the found parameters against the theoretically suggested dependencies like done by Dr. Peeters [22, 19, 8], Dr. Strintzi [20], or Dr. Camenen [23]. This not only requires to look at different discharges from the past, but also to consider new experiments at ASDEX Upgrade and as a next step also in other medium-sized tokamaks.

More time should be taken to assess and improve the numerical approaches, especially towards a more automatic procedure to access transport coefficients for a implemented model from experimental data. Beyond the data flow between the different calculations and simulations, the implemented fitting methods should be optimized to work more stably and be less time-consuming.

Main data source for the work in this thesis was the CXRS data and also here, a detailed study of the effects of the machine condition and its boronization on the data, its quality, and on the transport parameters should be discussed. Especially flat phase profiles should be avoided in modulation experiments since these discharges were problematic to analyze. Based on section 5.2, one could attempt to use higher NBI power modulation in the event of flat phase profiles. Depending on the plasma, however, this may not be compatible with maintaining constant background parameters.

In the long run, one would also have to take care of the used boundary conditions. The proposed model for the rotation still depends on the experimental rotation profile as a boundary condition. To develop a fully self-consistent model requires to also improve this part. The results gained in this thesis are promising as they show that with a detailed study it is possible to reproduce experimental rotation data. Furthermore, and that proves the feasibility of this method, it is possible to agree on the same transport coefficients for discharges with similar background profiles, but different applied perturbations. The caveat regarding the assumed Prandtl number, however, remains and requires further investigation. The author believes that it is necessary to spend more time investigating the dependencies of the built-up transport model to extrapolate it to future machines like ITER.

Bibliography

[1] *Fusion Physics*. Vienna: International Atomic Energy Agency, 2012. [Online]. Available: https://www-pub.iaea.org/books/IAEABooks/8879/Fusion-Physics

[2] J. D. Lawson, "Some criteria for a power producing thermonuclear reactor," *Proceedings of the Physical Society. Section B*, vol. 70, no. 1, pp. 6 – 10, Jan. 1957. [Online]. Available: https://doi.org/10.1088%2F0370-1301%2F70%2F1%2F303

[3] Академия наук СССР и Российская академия наук, *Успехи физических наук*. Гос. изд-во технико-теорет. лит-ры, 1996, no. 166. [Online]. Available: https://books.google.de/books?id=nTUXAQAAMAAJ

[4] R. Bilato and R. Kleiber, "IPP Summer University for Plasma Physics," *IPP Intranet*, Sep. 2012.

[5] B. Streibl, P. Lang, F. Leuterer, J.-M. Noterdaeme, and A. Stäler, "Machine design, fueling, and heating in ASDEX Upgrade," *Fusion Science and Technology*, vol. 44, pp. 578 – 592, Nov. 2003.

[6] W. Hornsby, C. Angioni, Z. Lu, E. Fable, I. Erofeev, R. M. McDermott, A. Medvedeva, A. Lebschy, and A. Peeters, "Global gyrokinetic simulations of intrinsic rotation in ASDEX Upgrade Ohmic L-mode plasmas," *Nuclear Fusion*, vol. 58, no. 5, Mar. 2018. [Online]. Available: https://doi.org/10.1088%2F1741-4326%2Faab22f

[7] C. Angioni, Y. Camenen, F. Casson, E. Fable, R. McDermott, A. Peeters, and J. Rice, "Off-diagonal particle and toroidal momentum transport: a survey of experimental, theoretical and modelling aspects," *Nuclear Fusion*, vol. 52, no. 11, Oct. 2012. [Online]. Available: https://doi.org/10.1088%2F0029-5515%2F52%2F11%2F114003

[8] A. Peeters, C. Angioni, A. Bortolon, Y. Camenen, F. Casson, B. Duval, L. Fiederspiel, W. Hornsby, Y. Idomura, T. Hein, N. Kluy, P. Mantica, F. Parra, A. Snodin, G. Szepesi, D. Strintzi, T. Tala, G. Tardini, P. de Vries, and J. Weiland, "Overview of toroidal momentum transport," *Nuclear Fusion*, vol. 51, no. 9, Aug. 2011. [Online]. Available: https://doi.org/10.1088/0029-5515/51/9/094027

[9] P. Diamond, C. McDevitt, O. Gürcan, T. Hahm, W. X. Wang, E. Yoon, I. Holod, Z. Lin, V. Naulin, and R. Singh, "Physics of non-diffusive turbulent transport of momentum and the origins of spontaneous rotation in tokamaks," vol. 49, no. 4, Mar. 2009. [Online]. Available: https://doi.org/10.1088%2F0029-5515%2F49%2F4%2F045002

[10] X. Garbet, P. Mantica, C. Angioni, E. Asp, Y. Baranov, C. Bourdelle, R. Budny, F. Crisanti, G. Cordey, L. Garzotti, N. Kirneva, D. Hogeweij, T. Hoang, F. Imbeaux, E. Joffrin, X. Litaudon, A. Manini, D. C. McDonald, H. Nordman, V. Parail, A. Peeters, F. Ryter, C. Sozzi, M. Valovic, T. Tala, A. Thyagaraja, I. Voitsekhovitch, J. Weiland, H. Weisen, A. Zabolotsky, and the JET EFDA Contributors, "Physics of transport in tokamaks," *Plasma Physics and Controlled Fusion*, vol. 46, no. 12B, pp. B557 – B574, Nov. 2004. [Online]. Available: https://doi.org/10.1088%2F0741-3335%2F46%2F12b%2F045

[11] P. Mantica, C. Angioni, N. Bonanomi, J. Citrin, B. A. Grierson, F. Koechl, A. Mariani, and G. M. Staebler, "Progress and challenges in understanding core transport in tokamaks in support to ITER operations," *Plasma Physics and Controlled Fusion*, vol. 62, no. 1, p. 014021, Dec. 2019. [Online]. Available: https://doi.org/10.1088%2F1361-6587%2Fab5ae1

[12] C. Angioni, E. Fable, M. Greenwald, M. Maslov, A. Peeters, H. Takenaga, and H. Weisen, “Particle transport in tokamak plasmas, theory and experiment,” *Plasma Physics and Controlled Fusion*, vol. 51, no. 12, p. 124017, 2009.

[13] H. Biglari, P. Diamond, and P. Terry, “Influence of sheared poloidal rotation on edge turbulence,” *Physics of Fluids B: Plasma Physics*, vol. 2, no. 1, pp. 1 – 4, 1990.

[14] F. Casson, R. M. McDermott, C. Angioni, Y. Camenen, R. Dux, E. Fable, R. Fischer, B. Geiger, P. Manas, L. Menchero *et al.*, “Validation of gyrokinetic modelling of light impurity transport including rotation in ASDEX Upgrade,” *Nuclear Fusion*, vol. 53, no. 6, p. 063026, 2013.

[15] C. Angioni, P. Mantica, T. Pütterich, M. Valisa, M. Baruzzo, E. Belli, P. Belo, F. Casson, C. Challis, P. Drewelow *et al.*, “Tungsten transport in JET H-mode plasmas in hybrid scenario, experimental observations and modelling,” *Nuclear Fusion*, vol. 54, no. 8, p. 83028, 2014.

[16] K. Burrell, “Effects of E×B velocity shear and magnetic shear on turbulence and transport in magnetic confinement devices,” *Physics of Plasmas*, vol. 4, no. 5, pp. 1499 – 1518, 1997.

[17] F. Hinton and R. D. Hazeltine, “Theory of plasma transport in toroidal confinement systems,” *Reviews of Modern Physics*, vol. 48, no. 2, p. 239, 1976.

[18] Y. Kim, P. Diamond, and R. Groebner, “Neoclassical poloidal and toroidal rotation in tokamaks,” *Physics of Fluids B: Plasma Physics*, vol. 3, no. 8, pp. 2050 – 2060, 1991.

[19] A. G. Peeters and C. Angioni, “Linear gyrokinetic calculations of toroidal momentum transport in a tokamak due to the ion temperature gradient mode,” *Physics of Plasmas*, vol. 12, no. 7, Jul. 2005. [Online]. Available: https://doi.org/10.1063/1.1949608

[20] D. Strintzi, A. G. Peeters, and J. Weiland, “The toroidal momentum diffusivity in a tokamak plasma: A comparison of fluid and kinetic calculations,” *Physics of Plasmas*, vol. 15, no. 4, 2008. [Online]. Available: https://doi.org/10.1063/1.2907370

[21] N. Mattor and P. H. Diamond, “Momentum and thermal transport in neutral-beam-heated tokamaks,” *Physics of Fluids*, vol. 31, no. 5, p. 1180, 1988. [Online]. Available: https://doi.org/10.1063/1.866747

[22] A. G. Peeters, C. Angioni, and D. Strintzi, “Toroidal momentum pinch velocity due to the Coriolis drift effect on small scale instabilities in a toroidal plasma,” *Physical Review Letters*, vol. 98, no. 26, Jun. 2007. [Online]. Available: https://doi.org/10.1103/physrevlett.98.265003

[23] Y. Camenen, Y. Idomura, S. Jolliet, and A. Peeters, “Consequences of profile shearing on toroidal momentum transport,” *Nuclear Fusion*, vol. 51, no. 7, Jun. 2011. [Online]. Available: https://doi.org/10.1088%2F0029-5515%2F51%2F7%2F073039

[24] R. Fischer, C. J. Fuchs, B. Kurzan, W. Suttrop, E. Wolfrum, and the ASDEX Upgrade Team, “Integrated data analysis of profile diagnostics at ASDEX Upgrade,” *Fusion Science and Technology*, vol. 58, no. 2, pp. 675 – 684, 2010. [Online]. Available: https://doi.org/10.13182/FST10-110

[25] M. Willensdorfer, G. Birkenmeier, R. E. Fischer, F. M., Laggner, E. Wolfrum, G. Veres, F. Aumayr, D. Carralero, L. Guimarãis, and B. Kurzan, “Characterization of the lithium beam emission spectroscopy at ASDEX Upgrade,” 2013.

[26] R. Fischer, E. Wolfrum, and J. Schweinzer, “Probabilistic lithium beam data analysis,” *Plasma Physics and Controlled Fusion*, vol. 50, no. 8, Jun. 2008. [Online]. Available: https://doi.org/10.1088%2F0741-3335%2F50%2F8%2F085009

[27] A. Mlynek, G. Schramm, H. Eixenberger, G. Sips, K. McCormick, M. Zilker, K. Behler, J. Eheberg, and the ASDEX Upgrade Team, “Design of a digital multiradian phase detector and its application in fusion plasma interferometry,” *Review of scientific instruments*, vol. 81, no. 3, p. 033507, 2010.

[28] R. Fischer, J. Hobirk, L. Barrera, A. Bock, A. Burckhart, I. Classen, M. Dunne, J. Fuchs, L. Giannone, K. Lackner, P. McCarthy, E. Poli, R. Preuss, M. Rampp, S. Rathgeber, M. Reich, B. Sieglin, W. Suttrop, and E. Wolfrum, “Magnetic equilibrium reconstruction using geometric information from temperature measurements at ASDEX Upgrade,” vol. 1, pp. 673 – 676, Jan. 2013.

[29] R. Fischer, A. Bock, M. Dunne, J. Fuchs, L. Giannone, K. Lackner, P. McCarthy, E. Poli, R. Preuss, M. Rampp, M. Schubert, J. Stober, W. Suttrop, G. Tardini, and M. Weiland, “Coupling of the flux diffusion equation with the equilibrium reconstruction at ASDEX Upgrade,” *Fusion Science and Technology*, vol. 69, pp. 526 – 536, Apr. 2016.

[30] The ASDEX Team, the ICRH Team, the LH Team, the NI Team, U. Schneider, W. Poschenrieder, M. Bessenrodt-Weberpals, J. Hofmann, A. Kallenbach, K. Krieger, E. Müller, H. Niedermeyer, F. Ryter, J. Roth, F. Söldner, A. Stäbler, K. Steuer, O. Vollmer, and F. Wagner, “Boronization of ASDEX,” *Journal of Nuclear Materials*, vol. 176-177, pp. 350 – 356, 1990. [Online]. Available: http://www.sciencedirect.com/science/article/pii/002231159090071T

[31] R. M. McDermott, A. Lebschy, B. Geiger, C. Bruhn, M. Cavedon, M. Dunne, R. Dux, R. Fischer, A. Kappatou, T. Pütterich, and E. Viezzer, “Extensions to the charge exchange recombination spectroscopy diagnostic suite at ASDEX Upgrade,” *Review of Scientific Instruments*, vol. 88, no. 7, Jul. 2017. [Online]. Available: https://doi.org/10.1063/1.4993131

[32] E. Viezzer, T. Pütterich, R. Dux, and R. M. McDermott, “High-resolution charge exchange measurements at ASDEX Upgrade,” *Review of Scientific Instruments*, vol. 83, no. 10, Oct. 2012. [Online]. Available: https://doi.org/10.1063/1.4755810

[33] P. Virtanen, R. Gommers, T. E. Oliphant, M. Haberland, T. Reddy, D. Cournapeau, E. Burovski, P. Peterson, W. Weckesser, J. Bright, S. J. van der Walt, M. Brett, J. Wilson, K. Jarrod Millman, N. Mayorov, A. R. J. Nelson, E. Jones, R. Kern, E. Larson, C. Carey, İ. Polat, Y. Feng, E. W. Moore, J. Vand erPlas, D. Laxalde, J. Perktold, R. Cimrman, I. Henriksen, E. A. Quintero, C. R. Harris, A. M. Archibald, A. H. Ribeiro, F. Pedregosa, P. van Mulbregt, and S. . . Contributors, “SciPy 1.0: Fundamental Algorithms for Scientific Computing in Python,” *Nature Methods*, vol. 17, pp. 261 – 272, 2020.

[34] J. Breslau, M. Gorelenkova, F. Poli, J. Sachdev, and X. Yuan, “Transp,” 2018. [Online]. Available: https://www.osti.gov/doecode/biblio/12542

[35] A. Pankin, D. McCune, R. Andre, G. Bateman, and A. Kritz, “The tokamak monte carlo fast ion module NUBEAM in the National Transport Code Collaboration library,” *Computer Physics Communications*, vol. 159, no. 3, pp. 157 – 184, 2004.

[36] J. Breslau, M. Gorelenkova, F. Poli, J. Sachdev, and X. Yuan, “Transp,” 2018. [Online]. Available: https://www.osti.gov/doecode/biblio/12542

[37] A. Peeters, Y. Camenen, F. Casson, W. Hornsby, A. Snodin, D. Strintzi, and G. Szepesi, “The nonlinear gyro-kinetic flux tube code GKW,” *Computer Physics Communications*, vol. 180, no. 12, pp. 2650 – 2672, 2009, 40 YEARS OF CPC: A celebratory issue focused on quality software for high performance, grid and novel computing architectures. [Online]. Available: http://www.sciencedirect.com/science/article/pii/S0010465509002112

[38] A. G. Peeters and D. Strintzi, “The effect of a uniform radial electric field on the toroidal ion temperature gradient mode,” *Physics of Plasmas*, vol. 11, no. 8, pp. 3748 – 3751, 2004. [Online]. Available: https://doi.org/10.1063/1.1762876

[39] S. Jolliet, A. Bottino, P. Angelino, R. Hatzky, T. Tran, B. Mcmillan, O. Sauter, K. Appert, Y. Idomura, and L. Villard, “A global collisionless PIC code in magnetic coordinates,” *Computer Physics Communications*, vol. 177, no. 5, pp. 409 – 425, 2007. [Online]. Available: http://www.sciencedirect.com/science/article/pii/S0010465507002251

[40] Dr. Clemente Angioni (IPP Garching), “private communication,” 2020.

[41] G. Pereverzev and P. N. Yushmanov, “ASTRA Automated System for TRansport Analysis in a tokamak,” Germany, Tech. Rep., 2002. [Online]. Available: http://inis.iaea.org/search/search.aspx?orig_q=RN:33018446

[42] E. Fable, “A toroidal momentum transport equation for axisymmetric 1D transport codes,” *Plasma Physics and Controlled Fusion*, vol. 57, no. 4, p. 045007, 2015.

[43] R. M. McDermott, C. Angioni, R. Dux, A. Gude, T. Pütterich, F. Ryter, G. Tardini *et al.*, “Effect of electron cyclotron resonance heating (ECRH) on toroidal rotation in ASDEX Upgrade H-mode discharges,” *Plasma Physics and Controlled Fusion*, vol. 53, no. 3, p. 035007, 2011.

[44] W. R. Inc., “Mathematica, Version 12.1,” 2020. [Online]. Available: https://www.wolfram.com/mathematica

[45] T. Tala, K. Crombé, P. C. de Vries, J. Ferreira, P. Mantica, A. G. Peeters, Y. Andrew, R. Budny, G. Corrigan, A. Eriksson, X. Garbet, C. Giroud, M.-D. Hua, H. Nordman, V. Naulin, M. F. F. Nave, V. Parail, K. Rantamäki, B. D. Scott, P. Strand, G. Tardini, A. Thyagaraja, J. Weiland, and K. Zastrow, “Toroidal and poloidal momentum transport studies in tokamaks,” *Plasma Physics and Controlled Fusion*, vol. 49, no. 12B, pp. B291 – B302, Nov. 2007. [Online]. Available: https://doi.org/10.1088%2F0741-3335%2F49%2F12b%2Fs27

[46] T. Tala, A. Salmi, C. Angioni, F. Casson, G. Corrigan, J. Ferreira, C. Giroud, P. Mantica, V. Naulin, A. Peeters, W. Solomon, D. Strintzi, M. Tsalas, T. Versloot, P. de Vries, and K. Zastrow, “Parametric dependencies of momentum pinch and Prandtl number in JET,” *Nuclear Fusion*, vol. 51, no. 12, p. 123002, Nov. 2011. [Online]. Available: https://doi.org/10.1088%2F0029-5515%2F51%2F12%2F123002

[47] T. Tala, R. M. McDermott, J. Rice, A. Salmi, W. Solomon, C. Angioni, C. Gao, C. Giroud, W. Guttenfelder, J. Ferreira *et al.*, “Tokamak experiments to study the parametric dependences of momentum transport,” in *24th IAEA Fusion Energy Conference*. International Atomic Energy Agency IAEA, 2012.

[48] H. Weisen, Y. Camenen, A. Salmi, T. Versloot, P. de Vries, M. Maslov, T. Tala, M. Beurskens, and C. Giroud, “Identification of the ubiquitous Coriolis momentum pinch in JET tokamak plasmas,” *Nuclear Fusion*, vol. 52, no. 4, p. 042001, Mar. 2012. [Online]. Available: https://doi.org/10.1088%2F0029-5515%2F52%2F4%2F042001

[49] M. Yoshida, Y. Koide, H. Takenaga, H. Urano, N. Oyama, K. Kamiya, Y. Sakamoto, G. Matsunaga, Y. Kamada, and the JT-60 Team, “Momentum transport and plasma rotation profile in toroidal direction in JT-60U L-mode plasmas,” vol. 47, no. 8, pp. 856 – 863, Jul. 2007. [Online]. Available: https://doi.org/10.1088%2F0029-5515%2F47%2F8%2F017

[50] R. M. McDermott, C. Angioni, G. Conway, R. Dux, E. Fable, R. Fischer, T. Pütterich, F. Ryter, and E. Viezzer, “Core intrinsic rotation behaviour in ASDEX Upgrade Ohmic L-mode plasmas,” *Nuclear Fusion*, vol. 54, no. 4, p. 043009, Mar. 2014. [Online]. Available: https://doi.org/10.1088%2F0029-5515%2F54%2F4%2F043009

[51] S. Yang, Y.-S. Na, D. Na, J.-K. Park, Y. Shi, W. Ko, S. Lee, and T. Hahm, “Perturbative studies of toroidal momentum transport in KSTAR H-mode and the effect of ion temperature perturbation,” *Nuclear Fusion*, vol. 58, no. 6, p. 066008, Apr. 2018. [Online]. Available: https://doi.org/10.1088%2F1741-4326%2Faab90e

Appendix A

Numerical input

A.1 ASTRA variable names and input

Symbol	Quantity	ASTRA variable name
v_{Pinch}	pinch velocity	`CNPAR`
χ_φ	parallel momentum diffusivity	`XUPAR`
R	major radius	`RTOR`
L_{n_e}	logarithmic density gradient	`LNE`
s	shear	`SHEAR`
Π_{RS}	residual stress	`RUPFR`
χ_i	ion heat conductivity	`CAR62`
ρ_φ	rho toroidal	`XRHO`
S_{NBI}	torque on plasma	`TTRQ`
$v_\parallel$	velocity parallel to field lines	`UPAR`
c_s	speed of sound	`CS`
	minor radius of LCFS in the mid-plane	`ABC`
I_{pol}	normalized poloidal current	`IPOL`
a	minor radius	`AMETR`
Δ	Shafranov shift of the plasma boundary	`SHIFT`
V'	volume within a flux surface on the intermediate grid	`VRS`
$< (\nabla\rho)^2 > V'$	geometric factor	`G11`

Table A.1: ASTRA variable names (selection)

Code	Comment
`CBND4 = 0.8`	sets the boundary condition for rotation
`DTEQL = 100.`	do not recalculate the equilibrium
⋮	

Table A.2: ASTRA `log`-parameters (selection)

Code	**Comment** [41, cf. Chapter 4]
`NA1 100`	edge grid point number
`RTOR 1.65`	major radius
`AWALL 0.70`	minor radius in the mid-plane
`ELONM 1.7`	plasma chamber elongation
`TRICH 0.14`	plasma chamber triangularity
`AB 0.60`	total minor radius in the mid-plane
`ZMJ 1.0`	majority nuclear charge
`AMJ 2.0`	majority mass divided by proton mass
`BTOR 2.5`	toroidal magnetic field
`IPL 0.8`	plasma current
⋮	
`CAR1 ...CONDI:1.e-4`	scale and use `CONDI` from TRANSP in `CAR1`
`CAR2 ...CONDE:1.e-4`	scale and use `CONDE` from TRANSP in `CAR2`
`CAR4 ...BDENS:1.0`	use `BDENS` from TRANSP in `CAR4`
`CAR5 ...UFASTPP:1.0`	use `UFASTPP` from TRANSP in `CAR5`
`CAR10 ...UFASTPA:1.0`	use `UFASTPA` from TRANSP in `CAR10`
`CAR6 ...TQIN:1.e6`	scale and use `TQIN` from TRANSP in `CAR6`
`CAR7 ...ESRC:1.0`	use `ESRC` from TRANSP in `CAR7`
`CAR8 ....EHEAT:1.0`	use `EHEAT` from TRANSP in `CAR8`
`CAR9 ...IHEAT:1.0`	use `IHEAT` from TRANSP in `CAR9`
⋮	
`NAMEXP BND`	Pass the LCFS
`NTIMES 1`	using 1 temporal point and
`POINTS 50`	50 spatial points
`0`	pass the coordinates of the LCFS in meters
`2.1425660350098803`	in pairs of
`-0.017046535426772952`	z and
`2.1483990911276125`	R
⋮	

Table A.3: ASTRA `exp`-parameters (selection)

Code	**Comment**
`AMAIN=AMJ; ZMAIN=ZMJ;`	set mass and charge of main ion species
`ZIM1=5.; AIM1=10.;`	set mass and charge of main impurity species (boron)
`ZEF=ZEFX;`	use experimental values for Z_{eff}
`PRAD=PRADX;`	use experimental values for P_{rad}
`PE=CAR8X;`	use experimental values for P_e
`PI=CAR9X;`	use experimental values for P_i
`NE=NEX;`	use experimental values for n_e
`TE=TEX;`	use experimental values for T_e
`TI=TIX;`	use experimental values for T_i
`NIZ1=NE*(ZEF-1)/(ZIM1-1)/ZIM1;`	calculate the n_{imp}
`NDEUT=NE-ZIM1*NIZ1;`	calculate the n_D
`NI=NDEUT+NIZ1;`	calculate the n_i as sum of n_D and n_{imp}, neglect fast ions
`CAR61=abs(-625*QETOT/` `GRAD(TEX)/NE/G11)+0.001;`	calculate $\chi_{e,eff}$ (cf. [41, p. 40])
`CAR62=abs(-625*QITOT/` `GRAD(TIX)/NI/G11)+0.001;`	calculate $\chi_{i,eff}$ (cf. [41, p. 40])
`VTOR=VTORX*(RTOR+AMETR+SHIF);`	convert angular velocity to linear velocity
`MRHO=AMAIN*NI;`	total plasma mass
`XUPAR=(...+CHE3*XRHO*...)*CAR62;`	linear ansatz for the Pr number (cf. Equation 2.3)

`CNPAR=-XUPAR/RTOR*(CHE1*RTOR/LNE+`
`CHE2*SHEAR)*(ABC/RTOR)-`
`XUPAR*GRAD(IPOL)/IPOL;`
	pinch velocity (cf. Equation 2.6) - geometric term

`RUPFR=CV8*MRHO*XUPAR*RTOR*` `CS/ABC*(0.02*RTOR/LNE)*G11/VRS;`	residual stress (cf. Equation 2.7 and [23, eq. 28])
`TTRQ=5.9773e+07*CAR6X;`	use the total torque calculated by TRANSP and convert it to ASTRA units

`UPAR=VTOR;`
`UPAR:EQ[2,CBND4];;`
`UPARB=VTOR(AFX(CBND4))`
	use the experimental rotation data above the radial position `CBND4` (given in the `log`-file) as a boundary condition

`XE=0.0; HI=0.0; CI=0.0; DI=0.0;` `HN=0.0; XN=0.0; DE=0;`	neglect the other contributions to the transport (cf. [41, p. 41]
`VPOL=0.;`	neglect poloidal plasma rotation
`SAVEROT>:0.005:0.005::;`	call a routine to write out relevant data every 5 ms
⋮	

Table A.4: ASTRA `equ`-code (selection)

A.2 TRANSP input

Code	**Comment**
`nzones = 40`	number of radial zones for the 1d transport equations
`sedit = 0.002`	time spacing between profile output data
`stedit = 0.002`	time spacing between scalar output data
`tgrid1 = 0.002`	time spacing between profile input data
`tgrid2 = 0.002`	time spacing between scalar input data
`nltipro = T`	use T_i from input data
`nlti2 = T`	use the T_i data directly, skip predictive calculations
`fiefac = 1.0`	use T_i data only
`giefac = 0.0`	do not use T_e data for T_i prediction
`nprad = 2`	use theoretical calculation for radiated power
`nlvphi = T`	use v_{rot} from input data
`nlomgvtr = T`	consider the rotation data as diagnostics species rotation
`nvphmod = 0`	disable plasma rotation prediction
`aimp = 12.0`	atomic weight of impurity
`nptcls = 200000`	number of simulated ion particles
`dtbeam = 0.002`	beam model time step

Table A.5: TRANSP namelist parameters (selection)

A.3 Performed TRANSP runs to study fitting concepts

Run No.	n_e	T_e	T_i	v_{rot}	Z_{eff}, P_{NBI}, P_{ECRH}
34027A18	const	const	const	const	smoothed
34027A19	fitted	const	const	const	smoothed
34027A20	sfull	const	const	const	smoothed
34027A21	const	fitted	const	const	smoothed
34027A22	const	sfull	const	const	smoothed
34027A23	const	const	mod1	const	smoothed
34027A24	const	const	mod12	const	smoothed
34027A25	const	const	fitted	const	smoothed
34027A26	const	const	sfull	const	smoothed
34027A27	const	const	const	mod1	smoothed
34027A28	const	const	const	mod12	smoothed
34027A29	const	const	const	fitted	smoothed
34027A30	const	const	const	sfull	smoothed
34027A32	fitted	fitted	fitted	fitted	smoothed
34027A35	const	const	const	const	unsmoothed

Table A.6: The TRANSP runs performed to study the various fitting concepts (cf. Section 5.1)

Appendix B

Plots of transport parameter fitting on Fourier profiles

Errors on the ASTRA simulation profiles are as large as their experimental counterparts but are not included to enhance visibility.

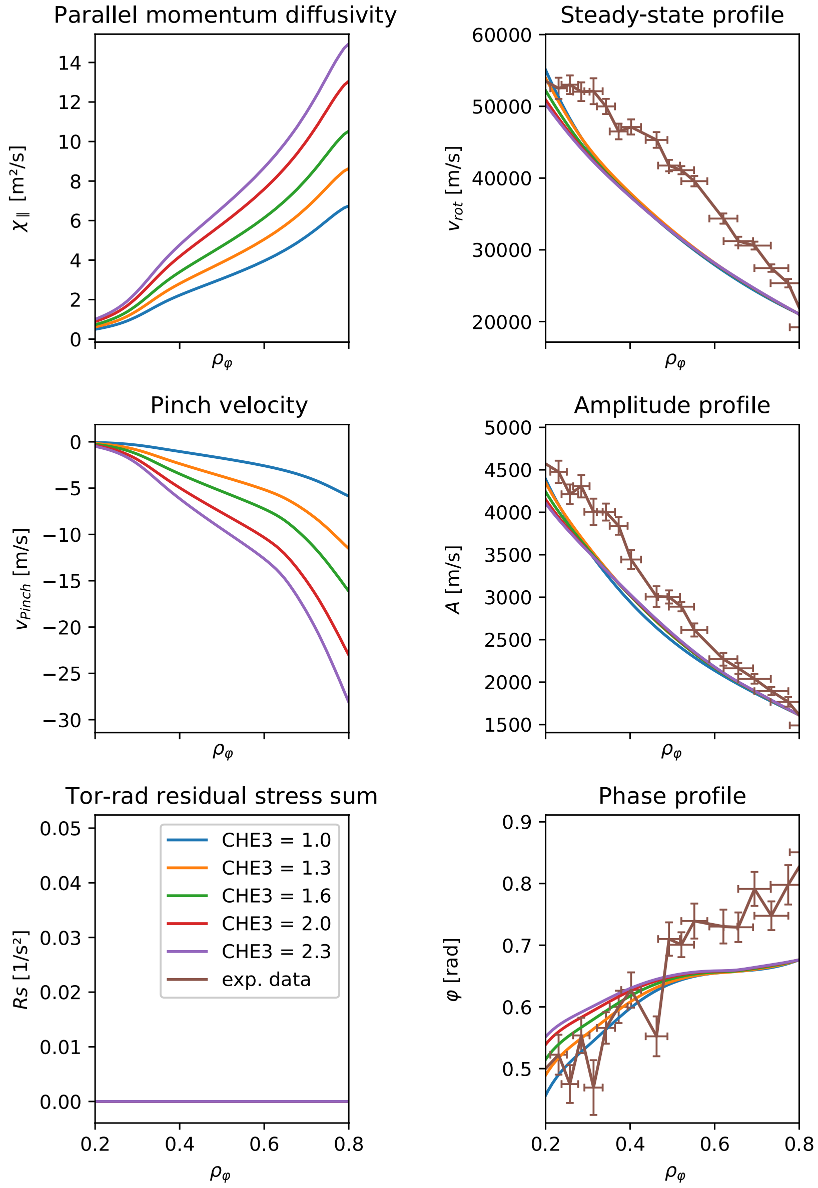

Figure B.1: ASTRA simulations with varying `CHE3` and optimized `CHE1` and `CHE2`, #34027

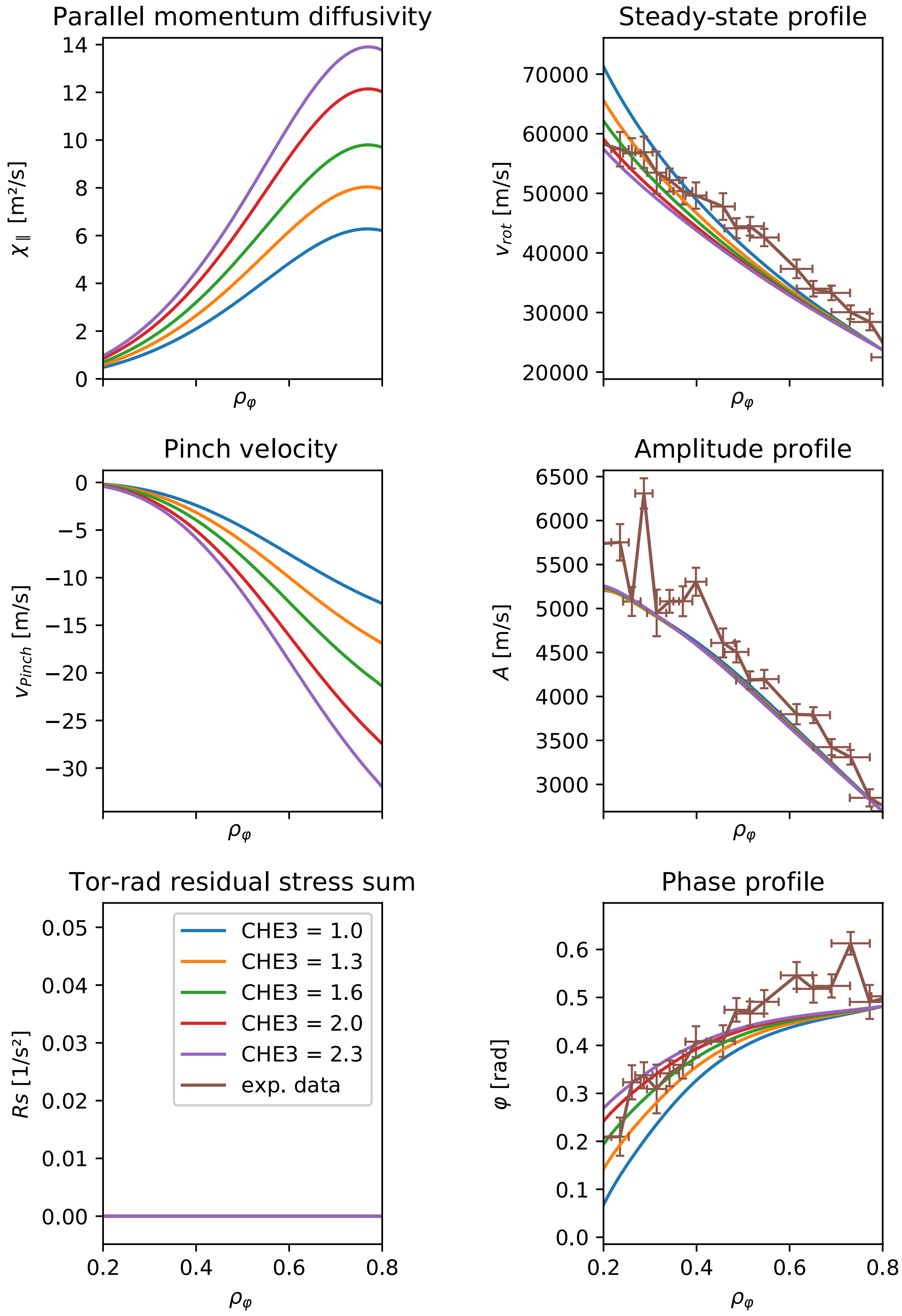

Figure B.2: ASTRA simulations with varying `CHE3` and optimized `CHE1` and `CHE2`, #34042

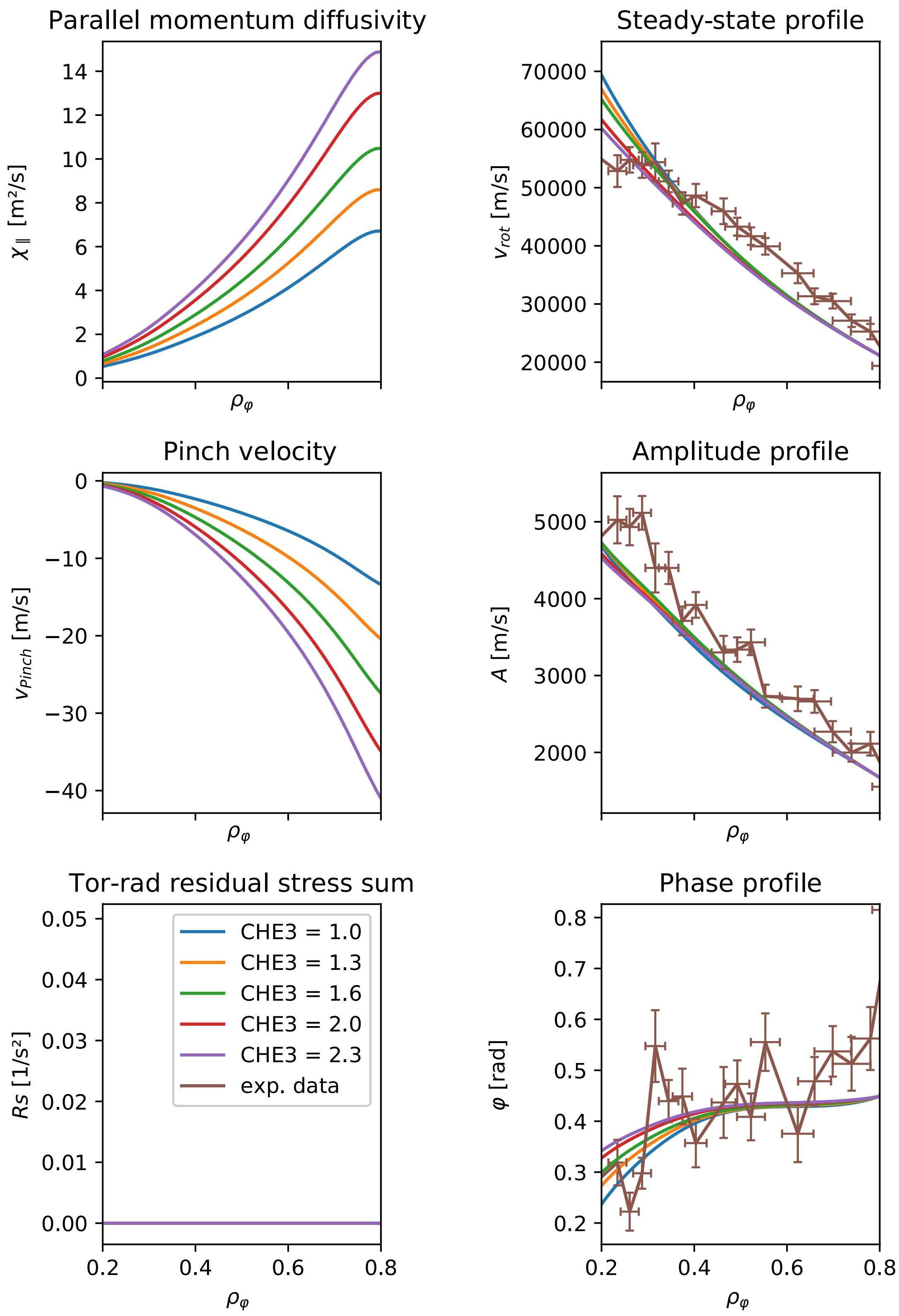

Figure B.3: ASTRA simulations with varying `CHE3` and optimized `CHE1` and `CHE2`, #34047

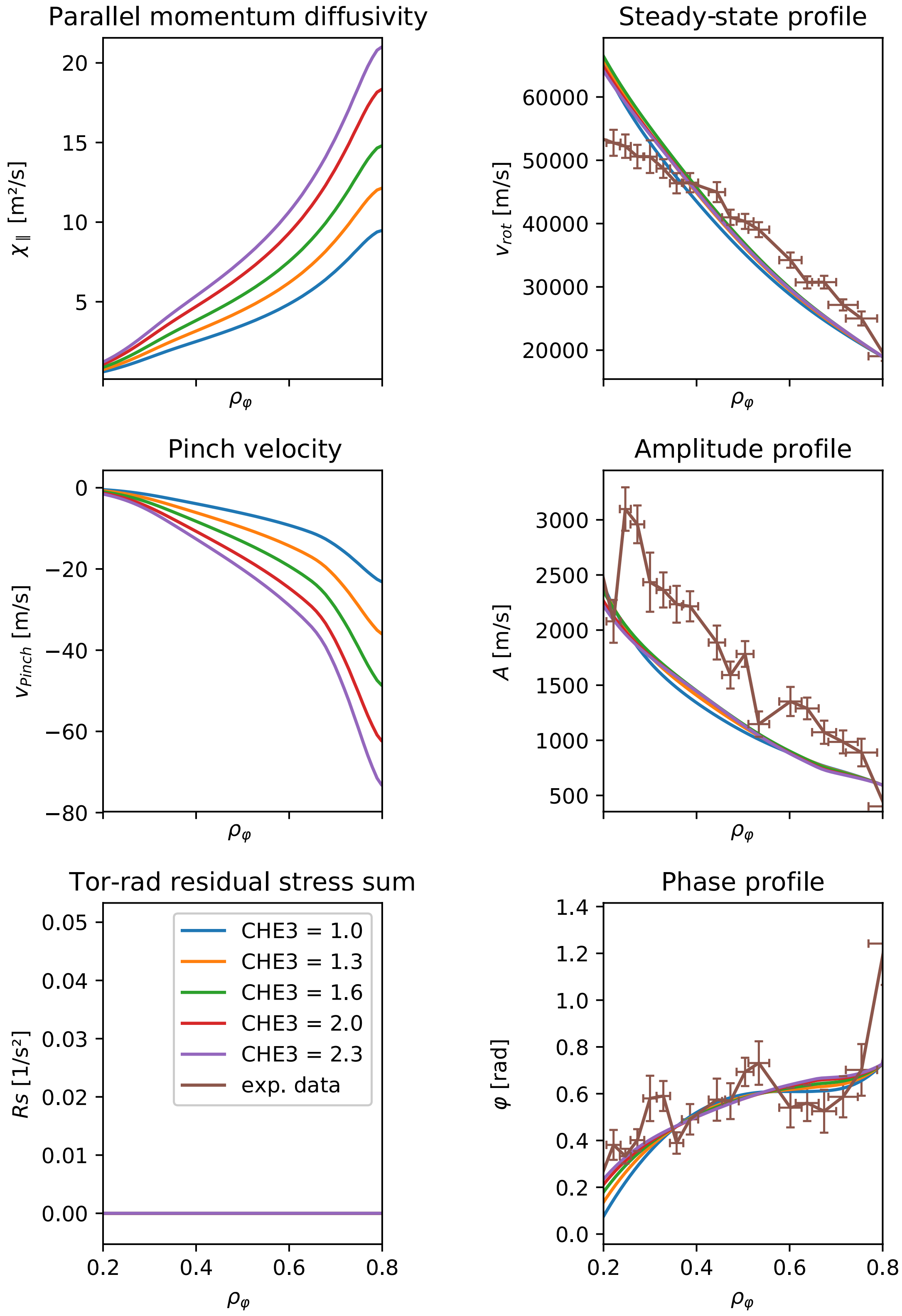

Figure B.4: ASTRA simulations with varying `CHE3` and optimized `CHE1` and `CHE2`, #34050

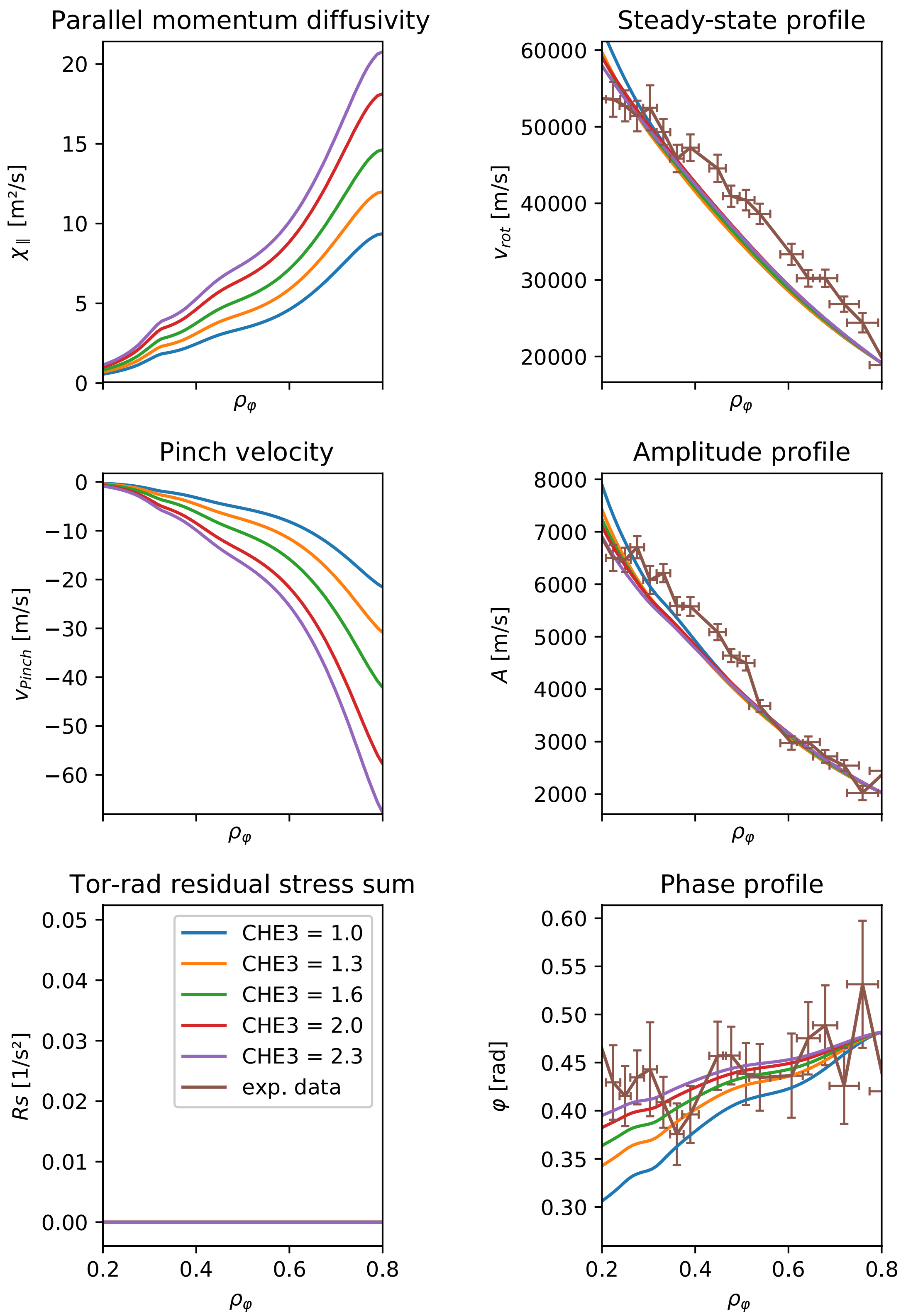

Figure B.5: ASTRA simulations with varying `CHE3` and optimized `CHE1` and `CHE2`, #34051

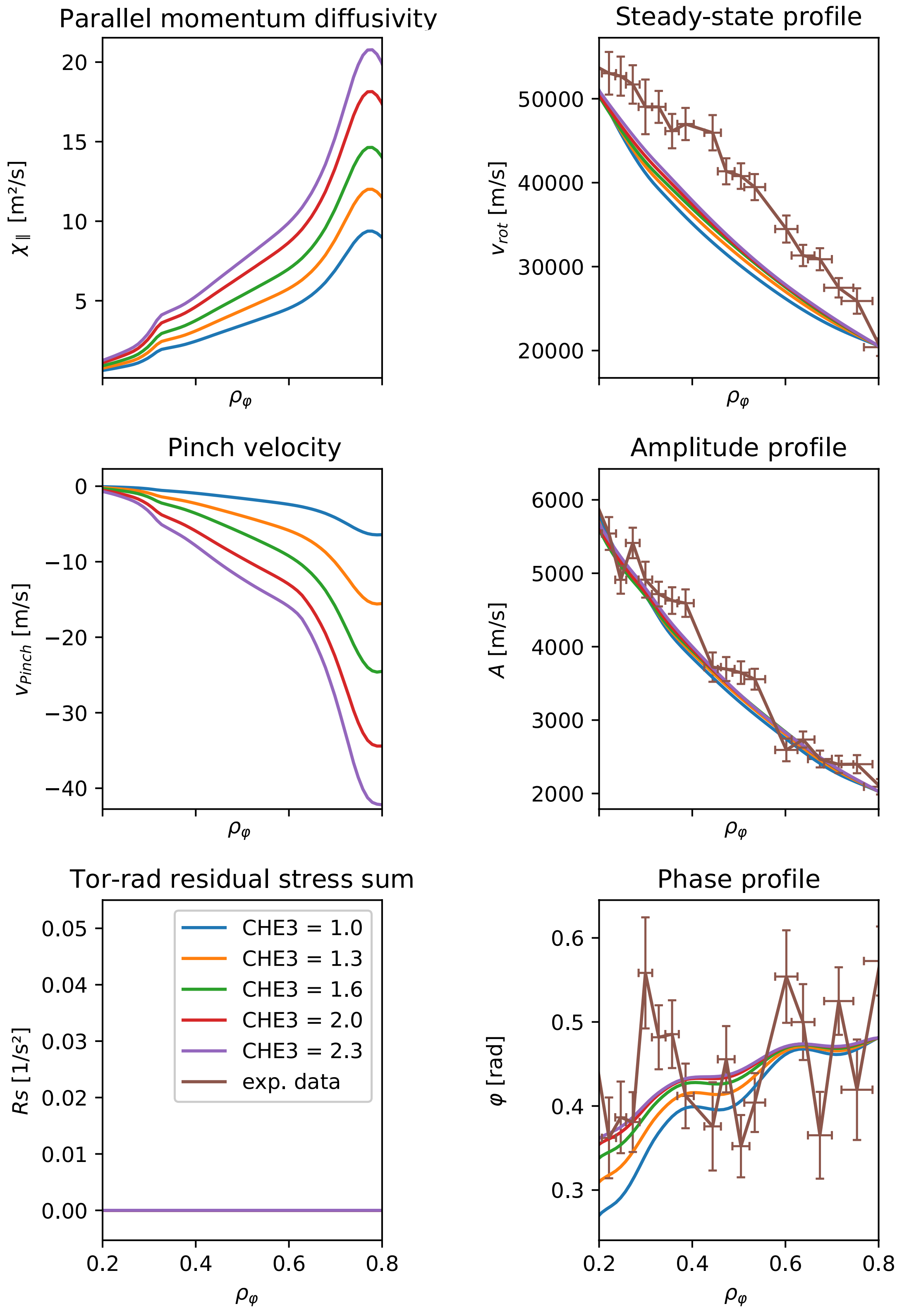

Figure B.6: ASTRA simulations with varying `CHE3` and optimized `CHE1` and `CHE2`, #34063.1

Erklärung

Hiermit erkläre ich, die vorliegende Arbeit selbständig verfasst zu haben und keine anderen als die in der Arbeit angegebenen Quellen und Hilfsmittel benutzt zu haben.

München,

Carl Friedrich Benedikt Zimmermann